Vibrational Spectroscopy for Fundamental Cell Behavior Analyses in a Wound Healing Model

Dissertation zur Erlangung des akademischen Grades des Doktors der Naturwissenschaften (Dr. rer. nat.)

eingereicht in der Fakultät für Chemie der Technischen Universität Dortmund

vorgelegt von

Melissa Mariani, MSc Immunology & Immunogenetics
aus Amerika

ISAS
Institute for
Analytical Sciences
Dortmund und Berlin

Oktober 2009

Table of Contents

List Of Abbreviations

ATCB	β-actin
BSA	Bovine Serum Albumin
C.A	Classically Activated
DAPI	14',6-diamidino-2-phenylindole
FT-IR	Fourier-Transform Infrared
FN	Fibronectin
HCA	Hierarchical Cluster Analysis
CAV1	Caveolin-1
CAV2	Caveolin-2
cDNA	Complimentary Deoxynucleic Acid
cm^{-1}	Wavenumber
Ct	Cycle Threshold
dNTPs	Deoxyribonucleoside triphosphate
dATP	2'-deoxyadenosine 5'-triphosphate
dTTP	deoxytimidine triphosphate
dGTP	2'-deoxyuanosine 5'-triphosphate
dCTP	deoxycytidine 5'-triphosphate
DMEM	Dulbecco's Modified Eagle's Medium
DOX	Doxycycline
ECM	extracellular matrix
EGF	Epidermal Growth Factor
FCS	Fetal Calf Serum
FRET	Fluorescence Resonance Energy Transfer
GAPDH	glyceraldehyde 3-phosphate dehydrogenase
H&E	Hematoxylin & Eosin
HMBS	hydroxymethylbilane synthase
IL-1b	Interleukin-1b
IL-6	Interleukin-6
IL-8	Interleukin-8
ITGA2	Integrin-alpha 2
ITGA3	Integrin-alpha 3
KRT16	Keratin 16
LPS	Lipopolysaccharide
MMP	Matrix Metalloproteinase
mRNA	Messanger Ribonucleic Acid
NEAA	Non-Essential Amino Acids
NFκB	Nuclear-factor kappa B
P/S	Pennicillin/Streptomycin
PBS	Phosphate Buffered Saline
PBST	Phosphate Buffered Saline + Tween
PCA	Principle Component Analysis
PCR	Polymerase Chain Reaction
PPARβ/δ	Proliferator-Activated Receptor Beta/Delta
RT	Reverse Transcription

RT-qPCR	Reverse Transcription Quantitative Polymerase Chain Reaction
SERS	Surface-Enhanced Raman Spectroscopy
TBP	TATA binding protein
TERS	Tip-Enhanced Raman Spectroscopy
TIMP	Tissue Inhibitor Metalloproteinase
TGF-β	Transcription Growth Factor- beta
TNF-α	Tumor Necrosis Factor- alpha
UBC	Ubiquitin C
UHCA	Unsupervised Hierarchical Cluster Analysis
YWHAZ	Tyrosine 3-monooxygenase/tryptophan 5-monooxygenase activation protein

Zusammenfassung und Ausblick

Spektroskopische Techniken sind seit langem etablierte Analysemethoden in der physikalischen Chemie und liefern eine vollständige chemische Zusammensetzung einer Probe durch markerfreie Analyse. Im Unterschied dazu werden in herkömmlichen Versuchsvorschriften in den Lebendwissenschaften Analysemethoden angewendet, die die Proben beeinflussen, wie z. B. das Markieren. Diese invasiven Schritte können durch eine Verknüpfung von spektroskopischen Techniken mit dem Bereich der Lebendwissenschaften erfolgreich umgangen werden.

Der Schwerpunkt in den Lebendwissenschaften wurde kürzlich auf Grund der Zunahme an Beliebtheit beider „omik" Wissenschaften und Systembiologie umgelenkt, wobei die Aufmerksamkeit von einzelnen Komponenten zum Verständnis dieser Komponenten im Kontext des gesamten Systems überging. Hierbei ist die Erforschung einzelner Komponenten und das Verständnis ihrer komplexen Einbindung in biologische Systeme in den Brennpunkt gerückt. Da die Spektroskopie eine nichtinvasive, labelfreie Analysemethode bietet, wächst auch das Intersse, diese Verfahren zunehmend in der Grundlagenforschung der Lebendwissenschaften anzuwenden.

Gekoppelt mit den Fortschritten bei der multivariaten Datenanalyse besitzen die Anwendungen der Fourier Transform Infrarot (FT-IR) und Raman Spektroskopie einen besonderen Reiz, auf Grund ihrer Möglichkeit, lebende oder fixierte Proben mit einer lateralen Auflösung weniger Mikrometer bis in den Nanometerbereich zu untersuchen. Allerdings muß für die Einbindung dieser spektroskopischen Techniken in die biologische Grundlagenforschung und biomedizinische Diagnostik ihre Zuverlässigkeit und Konsistenz durch Vergleiche mit den aktuellen Gold-Standard-Methoden bewiesen werden. Die empfindlichste Methode für die Detektion von mRNA ist derzeit die reverse Transkriptase PCR (RT-PCR), die auf Grund ihrer bewährten Beiträge in biologischen Studien und biomedizinischer Diagnostik genutzt wurde, um die Ergebnisse der spektroskopischen Analysen zu bestätigen und auch um die gesamte Interpretation der spektralen Daten zu unterstützen.

In dieser Arbeit wurden spektroskopische bildgebende Verfahren auf das gut verstandene Modell der epidermalen Wundheilung angewendet. Der hoch komplexe Vorgang der Re-Epithelisierung umfasst Signale der Zell-Zell- und Zell-Substrat-Kommunikation, die zu Zellpolarisierung, Migration und Organisation führen. Trotz der übereinstimmenden Meinung, dass diese morphologischen Veränderungen stattfinden, bleiben die genauen biophysikalischen Prozesse, die zu ihrer Entstehung und Aufrechterhaltung beitragen, kaum verstanden.

Zudem werden die Vorteile der Kombination von schwingungsspektroskopischer Bildgebung mit chemometrischer Datenanalyse und RT-qPCR deutlich ihre Stärken als kombinierte Methode für *in vitro* Zellstudien. Beginnend mit einer Abschätzung der Einflüsse einer Fixierung auf die spektroskopische Probenanalyse, bis hin zu komplexeren Aufgaben, wie z. B. die *in vitro* Untersuchung fundamentaler Zell-Zell-Mechanismen während der epidermalen Re-Epithelisierung, zeigten die Schwingungsspektroskopie und RT-qPCR großes Potential für Anwendungen in komplexeren *in vitro* Modellsystemen und für weitere Anwendungen in Bereichen der biomedizinischen Diagnostik, einschließlich Krebs-Metastase, Gewebezüchtung und Drogeneinwirkung.

Diese Arbeit hat erfolgreich die Vorteile dieses multidisziplinären Ansatzes gezeigt und bietet einen Ausblick auf weiterführende Studien über epidermale Wundheilung und Zell-Organisationsprofile. Darüber hinaus haben die Vorteile der Kombination von spektroskopischer Bildgebung mit RT-qPCR deutlich gezeigt, dass zusätzlich eine Quantifizierung erreicht werden kann, wie auch eine Bestätigung der Ergebnisse, wobei beides grundlegende Voraussetzungen für vertrauenswürdige biologische Studien und aktuelle biomedizinische Diagnostik sind.

Chapter 1

Introduction

Spectroscopic techniques have long been established methods of sample analysis in physical chemistry and provide the total chemical composition of a sample through label-free analysis. Traditionally, experimental protocols in the life sciences differ by often employing perturbing methodologies, like sample labeling, for analyses. By bridging spectroscopic techniques into the realm of life sciences, these invasive stages have been successfully circumvented.

Biological applications of vibrational spectroscopy commenced in the 1950s with the first reports on proteins and amino acids[1]. The first spectra of cells were reported in the early 1980s using resonance Raman spectroscopy to study antibiotic interactions with nucleic acids[2]. In 1991 the identification of whole-cells and bacterial strains was achieved with infrared (IR) spectroscopy[3]. The extent of data presented from these pioneering biological studies demanded the development of statistical techniques capable of extracting the desired information. Consequently, the development of multivariate analysis tools has facilitated exploring increasingly complex matrices, like whole tissue samples.

The focus of the life sciences has been redirected from a recent surge in the popularity of both 'omics' studies and systems biology, taking the focus off of individual components and shifting it toward understanding components within a system context. Studying individual components and understanding their complex association within biological systems has become the focal point. Functional and structural changes in these components, like surface proteins, during interactions and in varying cell states hold the answers to targets for diagnostic and preventative endeavors[4]. With spectroscopic studies providing a non-invasive, label-free method of analysis, interest in applying these applications to the increasingly fundamental studies of the life sciences has grown[5].

Coupled with the advances in multivariate data analysis, Fourier transform infrared (FT-IR) and Raman spectroscopy are of particular appeal from their ability to assess live or preserved samples with lateral resolutions spanning a few microns down to the nanometer scale.

Likewise, as the medical and pharmaceutical industries continue toward an increasingly quantitative path, all techniques implemented for diagnostic use must be capable of providing some degree of quantification. FT-IR and Raman spectroscopy possess an intrinsic degree of quantitation along with multivariate data, compared with the traditional univariate data obtained from conventional imaging techniques. This is particularly of interest for the highly complex, heterogeneous samples often found in biological studies. However, for the incorporation of these spectroscopic techniques into fundamental biological studies and biomedical diagnostics, their reliability and consistency must be confirmed by means of comparison with current gold-standard techniques.

Real-time reverse transcription–quantitative polymerase chain reaction (RT–qPCR) is at present the most sensitive technique for messenger ribonucleic acid (mRNA) detection, providing robust PCR product measurements. Additionally, RT-qPCR is commonly applied to clinical diagnostics, making the technique an industry standard for RNA product detection and quantification[6-8]. An increase in RT-qPCR applications, combined with the growing importance of clinical diagnostics, has permitted both areas to develop in parallel. Reflecting these advancements, the value of RT-qPCR in quantitative clinical diagnostics has increased largely through the stochastic integration of fluorochromes that can be directly related to qualitative measurements[9]. From the established contribution of RT-qPCR in biological studies and biomedical diagnostics, this technique was used to both confirm spectroscopic analyses and contribute to overall spectral data interpretations.

This body of research applied spectroscopic imaging techniques to the well known model of epidermal wound healing. Wound healing and chronic wounds continue to represent a significant burden to both patients and health care systems, effecting millions of patients annually and leading to a financial set-back nearing $20 billion per fiscal year within the US alone[10]. To gain a better handle on wound treatments, a more developed understanding of the healing process is needed. The highly complex process of re-epithelialization alone incorporates numerous cues from cell-cell and cell-substrate

communication leading to cell polarization, migration and organization. Despite the consensus that these morphological occurrences take place, the precise biophysical processes that contribute to their onset and maintenance all remain poorly understood.

To apply spectroscopic studies to this *in vitro* model system, the understanding of sample preparation for subsequent analysis was critical. With this in mind, Chapter 5 describes the effects of sample preparation on Raman spectral analyses and suggests a method for standardization.

Following sample preparation, Chapters 6 through 9 display applications of spectroscopic techniques paired with RT-qPCR for use with the *in vitro* model system of epidermal wound healing. These imaging techniques provided phenotypical sample analyses, while RT-qPCR presented a snapshot of the genotype, enabling a 'systems' view of cell behavior. This multifaceted approach was found particularly advantageous for studying associated molecular cues during wound healing, including cell polarization, migration and organization.

This body of work culminates with the success of a multidisciplinary approach and provides an outlook for continued work on both epidermal wound healing, cell organizational profiles and applications of spectroscopic imaging with RT-qPCR for biological studies and biomedical diagnostics.

References

1. M. C. Tobin, *Science*, 1968, **161**, 68-69.
2. M. Manfait, A. J. Alix, P. Jeannesson, J. C. Jardillier and T. Theophanides, *Nucleic Acids Res*, 1982, **10**, 3803-3816.
3. D. Naumann, D. Helm and H. Labischinski, *Nature*, 1991, **351**, 81-82.
4. R. J. Swain and M. M. Stevens, *Biochem Soc Trans*, 2007, **35**, 544-549.
5. J. R. Baena and B. Lendl, *Curr Opin Chem Biol*, 2004, **8**, 534-539.
6. S. A. Bustin, *J Mol Endocrinol*, 2000, **25**, 169-193.
7. S. A. Bustin and T. Nolan, *J Biomol Tech*, 2004, **15**, 155-166.
8. D. G. Ginzinger, *Exp Hematol*, 2002, **30**, 503-512.
9. W. P. Halford, V. C. Falco, B. M. Gebhardt and D. J. Carr, *Anal Biochem*, 1999, **266**, 181-191.
10. L. Branski, G. Gauglitz, D. Herndon and M. Jeschke, *Burns*, 2009, **35**, 171-180.

Chapter 2

The Tissue Environment

2.1 Why Wound Healing?

While wound healing has been extensively studied, the localized and transient nature of migratory behavior makes elucidating precise cell-cell mechanisms involved in migration and the transport of intra-cellular components particularly difficult[1, 2]. As with many cell actions, cell migration involves a combination of localized cell-cell and cell-substrate interactions mediated by transient molecular signaling. With epidermal wound healing incorporating so many aspects of cell communication, it provides a well characterized model to explore the fundamental cell behavior and their interactions with their environment, leading to migration onset, termination and successive organizational profiles.

2.2 Summary of Epidermal Wound Healing

The skin is the largest organ of the body and is formed by multiple structural layers (Figure 2.1). In the event of wounding, the onset of healing processes are critical for upholding its function as an environmental barrier[3]. The biological process of wound healing is detailed, incorporating most aspects of the immune system for the regeneration of destroyed tissue with new, living tissue and requires three distinct stages for complete tissue regeneration (Figure 2.2)[4].
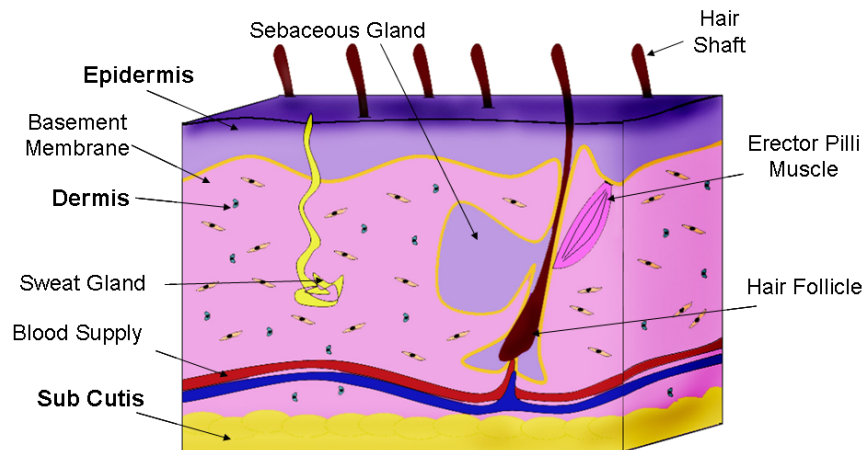
Figure 2.1 Structural overview of tissue. An intricate and well-orchestrated interplay between cells of the 3 main layers (shown in bold) of skin occurs to maintain tissue homeostasis. The epidermal layer is the thinnest (0.1-0.2 mm thick)[5] and provides the first layer of defense. The epidermis is attached to the dermis by the basement membrane, anchoring the 2 main layers together through its collagenous network. Hair follicle cells that aid in maintaining the epidermis reach this region from their dermal origin by diffusion through the dermal capillary network. Once keratinocytes from the dermis reach the epidermis, they differentiate upwards, forming the multiple layers among the epidermis (see Figure 2.3).
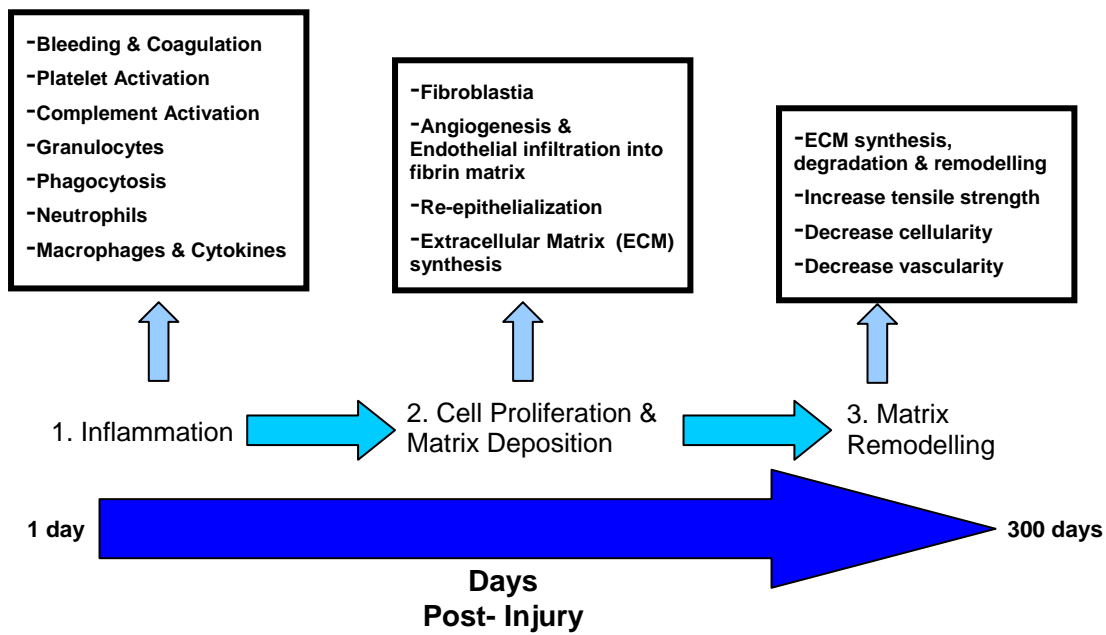
Figure 2.2 Summary of wound healing mechanisms. These detailed healing stages are implemented immediately following trauma to the skin and continue for days to years post-injury to reinstate tissue integrity.

The healing process commences with the formation of a fibrin clot at the wound site, closely followed by an inflammatory response to the skin trauma and concludes with cell proliferation and maturation[6,7]. Both innate and adaptive immune responses are called upon for the production of new tissue[4]. This includes complex reactions and interactions between cytokines, chemokines, growth factors and multiple cell lineages[7].

Shortly following the inflammatory response, re-epithelialization combines a refined orchestration of several cellular processes, commencing with basal keratinocyte activation on the wound edge. Keratinocytes dominate the epidermis and are present in differentiated forms throughout 5 layers (Figure 2.3). These epidermal layers work synergistically to provide the first line of defense from external threats like infection and maintain internal homeostasis. Not only do basal keratinocytes attach to the basement membrane, connecting the epidermis with the dermis; basal keratinocytes are also instrumental in regenerating damaged tissue in the event of wounding by reconstructing the damaged epidermis through proliferation and re-epithelialization. Phenotypic and genotypic modifications include the dynamic re-organization of inter-cellular components like actin microtubules and filaments, the expression and redistribution of integrin and cadherin adhesion complexes and the overall polarization of cells toward the gradient of attractants from the opposing wounded edge[8, 9].

These amendments spatially regulate signal transduction pathways and provide traction for the protruding lamellipodia that emerge.

Once polarization has prepared cells for migration, gradients of diffusible factors and electrochemical signals assist in the generation and transmission of migratory forces to initiate and sustain migratory behavior[8, 10-12]. These necessary modifications, combined with the requirement for a scaffold to support migrating cells enables the onset of re-epithelialization, beginning within hours post-wounding[13]. Proximal cells are recruited to participate in migration by the amplification of chemotactic signals from activated cells on the wound edge, enhancing re-epithelialization[14].

Migratory activity persists until cells from opposing wound edges come into contact, setting off 'contact inhibition'[15]. Increased proliferation replenishes damaged and dead cells while aiding keratinocyte directional sensing and migration, although does not govern migratory activity[16,17].

The final stages also include the reorganization of the ECM and contraction of the newly formed tissue. Contraction occurs as a result of fibroblast modulation into myofibroblasts, which contain α-smooth muscle actin to facilitate closing the wound space[18,19]. Upon completion of the healing process, a scar develops by the formation of healthy tissue sealing the injury site[20].

2.3 Epidermal Environment

The epidermis is a hydrophobic 5-layer conglomerate of cells that provides the body with the first barrier from the environment. Epidermal layers include the stratified corneum, stratified granulosum and stratified spinosum layers and are composed primarily of keratinocytes (Figure 2.3).
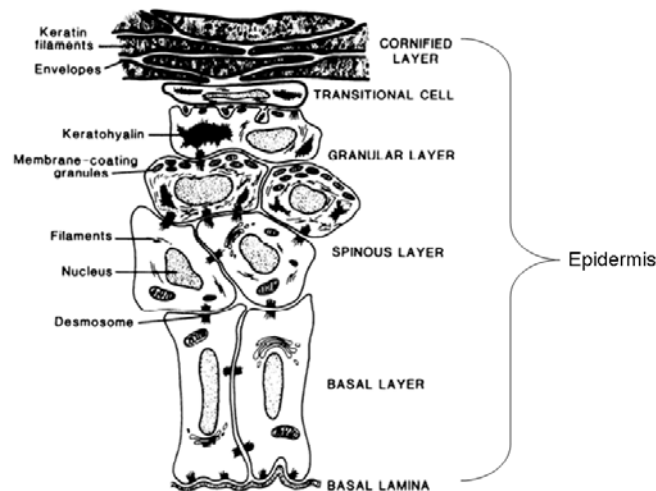
Figure 2.3 Morphological & structural changes in keratinocyte growth & differentiation[3]. Keratinocytes differentiate upward from the basal layer toward the cornified layer. As keratinocytes differentiate, their morphology changes drastically. Cells become smaller and more granular in the spinous and granular layer, while cells in the transitional and cornified layers possess no nuclei and predominately contain keratin filaments to provide a waterproof coating.

As cells develop in the stratified spinosum, they migrate up to the stratified corneum, forming between 20 to 30 layers of dead cells that are removed during desquamification. There are no blood vessels within the epidermis, forcing cell nourishment by blood capillary diffusion through the basement membrane, which provides an anchor between the epidermis and dermis.

2.4 Keratinocytes

As mentioned, keratinocytes are the prevailing cell type within the epidermis, originating in the basal layer from proximal stem cell differentiation and differentiate upward to form the epidermis[3] (Figure 3). These cells were originally cultured in a lab just over 30 years ago[21, 22] and lead to the production of small sheets of cells ranging from 2-3 layers thick[23] and have been shown to migrate in response to stimulated wounding, making them an ideal model for re-epithelialization studies. Moreover, their cytokine profiles are largely unchanged from that of their *in vivo* environment during keratinocyte differentiation states[24, 25].

2.5 Extracellular Matrix

The extracellular matrix (ECM) fills the intra-cellular space among keratinocyte sheets and includes multiple protein components. The scaffold that is formed by ECM proteins is vital for supporting cell motility and functionality, cell interactions and overall tissue structure. Important proteins for the

structure of the ECM include multiple types of collagen (predominately types I and III), fibronectin, hyaluronic acid and laminin. Additionally, various matrix metalloproteinases (MMP), like MMP9, can be found throughout the ECM and act as proteolytic enzymes that can degrade and rebuild the ECM during normal conditions and wound healing[26, 27].

Through these various ECM components, a scaffold is formed to promote cell activity and instigating cell-cell interactions. Through the presence, maintenance or absence of a component, cellular interactions can be induced, modified or even completely inhibited[28]. Specifically through juxtacine signaling, cells can receive signals for proliferation, differentiation, and even a select form of programmed cell death that occurs once cells detach from their extracellular matrix scaffold, anoikis[29].

2.6 Conclusion

The organizational profiles of keratinocyte during re-epithelialization and the associated mechanisms for proximal cell recruitment enabling mass migration remain poorly understood. Understanding cell interactions and their effects on cell migration and organization during re-epithelialization can provide insight into these caveats.

Imaging of fixed samples has been very useful in measuring cell movement and changes in cell phenotypes, particularly through increasingly widespread techniques like fluorescence resonance energy transfer and fluorescence recovery after photo-bleaching with confocal and total internal reflection microscopy[30-34]. Through genetic cell labeling, specific intra-cellular components have been visualized in a contextual setting, whilst protein labeling has been able to monitor cytoskeletal component turnover and post-translational mechanisms[35,36]. Fluorescent labeling of signaling components that direct cytoskeletal formations are also commonly used, as with phosphoinisitol-3 kinase labeling, and have been employed to track both conformational changes in components and changes in distribution[37]. However, all techniques implement invasive, costly and time-consuming methods and often render the samples useless for additional downstream analysis. It is from these setbacks that the benefits of spectroscopic analyses methods can be fully appreciated and will be further addressed in the forthcoming chapter.

References

1.   M. Digmana, P. Wisemanb, C. Choic, A. Horwitzc and E. Grattona, *PNAS*, 2009, **106**, 2170-2175.
2.   P. Girard, E. Cavalcanti-Adam, R. Kemkemer and J. Spatz, *Soft Matter*, 2007, **3**, 307-326.
3.   R. L. Eckert, *Physiol Rev*, 1989, **69**, 1316-1346.
4.   T. Watson, *In Touch*, 2003.
5.   S. MacNeil, *Nature*, 2007, **445**, 874-880.
6.   A. K. Tsirogianni, N. M. Moutsopoulos and H. M. Moutsopoulos, *Injury*, 2006, **37 Suppl 1**, S5-12.
7.   G. Broughton, 2nd, J. E. Janis and C. E. Attinger, *Plast Reconstr Surg*, 2006, **117**, 1e-S-32e-S.
8.   L. Smilenov, A. Mikhailov, R. Pelham Jr., E. Marcantonio and G. Gundersen, *Science*, 1999, **282**, 1172-1174.
9.   A. R. Horwitz and J. T. Parsons, *Science*, 1999, **286**, 1102-1103.
10.   D. A. Lauffenburger and L. G. Griffith, *Proc Natl Acad Sci U S A*, 2001, **98**, 4282-4284.
11.   M. Vicente-Manzanares, C. Choi and A. Horwitz, *J Cell Science*, 2009, **122**, 199-206.
12.   C. E. Pullar and R. R. Isseroff, *J Cell Sci*, 2005, **118**, 2023-2034.
13.   H. Larjava, L. Koivisto and L. Hakkinen, *Chapter 3: Keratinocyte Interactions with Fibronectin During Wound Healing*, Tex Landes Bioscience, Inc, Austin, TX, 2002.
14.   P. Kriebel, V. Barr, E. Rericha, G. Zhang and C. Parent, *J Cell Science*, 2008, **183**, 949-961.
15.   W. K. Nahm, B. D. Philpot, M. M. Adams, E. V. Badiavas, L. H. Zhou, J. Butmarc, M. F. Bear and V. Falanga, *J Cell Physiol*, 2004, **200**, 309-317.
16.   C. A. Parent and P. N. Devreotes, *Science*, 1999, **284**, 765-770.
17.   H. Tao, A. J. Berno, D. R. Cox and K. A. Frazer, *PLoS ONE*, 2007, **2**, e697.
18.   J. J. Tomasek, G. Gabbiani, B. Hinz, C. Chaponnier and R. A. Brown, *Nat Rev Mol Cell Biol*, 2002, **3**, 349-363.
19.   J. J. Tomasek, J. McRae, G. K. Owens and C. J. Haaksma, *Am J Pathol*, 2005, **166**, 1343-1351.
20.   A. Bayat, McGrouther, DA., Ferguson, MWJ, *BMJ*, 2003, **326**, 88-92.
21.   J. G. Rheinwald and H. Green, *Nature*, 1977, **265**, 421-424.
22.   J. G. Rheinwald and H. Green, *Cell*, 1975, **6**, 331-343.
23.   H. Green, O. Kehinde and J. Thomas, *Proc Natl Acad Sci U S A*, 1979, **76**, 5665-5668.
24.   J. Ansel, P. Perry, J. Brown, D. Damm, T. Phan, C. Hart, T. Luger and S. Hefeneider, *The Journal of Investigative Dermatology*, 1990, **94**, 101S-107S.
25.   A. Grone, *Veterinary Immunology and Immunopathology*, 2002, **88**, 1-12.
26.   J. M. Lamar, V. Iyer and C. M. DiPersio, *J Invest Dermatol*, 2008, **128**, 575-586.
27.   T. Salo, M. Makela, M. Kylmaniemi, H. Autio-Harmainen and H. Larjava, *Laboratory Investigation; A Journal of Technical Methods & Pathology*, 1994, **70**, 176-182.
28.   E. O'Toole, *Clin. Exp. Derm*, 2008, **26**, 525-530.
29.   S. M. Frisch and R. A. Screaton, *Curr Opin Cell Biol*, 2001, **13**, 555-562.
30.   M. E. Huot, C. M. Brown, N. Lamarche-Vane and S. Richard, *Mol Cell Biol*, 2009, **29**, 1933-1943.
31.   J. Morgan, R. Huckfeldt and R. O. Wong, *Exp Eye Res*, 2005, **80**, 297-306.
32.   Y. Sako and T. Uyemura, *Cell Struct Funct*, 2002, **27**, 357-365.
33.   L. Soon, F. Braet and J. Condeelis, *Microsc Res Tech*, 2007, **70**, 252-257.
34.   M. Parsons, B. Vojnovic and S. Ameer-Beg, *Biochem Soc Trans*, 2004, **32**, 431-433.
35.   B. N. Giepmans, S. R. Adams, M. H. Ellisman and R. Y. Tsien, *Science*, 2006, **312**, 217-224.
36.   D. M. Chudakov, S. Lukyanov and K. A. Lukyanov, *Trends in Biotechnology*, 2005, **23**, 605-613.

37.   A. J. Ridley, M. A. Schwartz, K. Burridge, R. A. Firtel, M. H. Ginsberg, G. Borisy, J. T. Parsons and A. R. Horwitz, *Science*, 2003, **302**, 1704-1709.

Chapter 3

Vibrational Spectroscopic Theory & Bio-Medical Applications

3.1 Why Vibrational Spectroscopy?

With the cause of many diseases still largely unknown, many empirical treatments are used to improve patients' quality of life. However, as with most empirical treatments, patient immunity can develop rendering it useless, treatments are not sufficiently aggressive or produce unwanted side-effects. This harbors a significant burden on the patient, both financially and emotionally. The medical industry is also affected by this burden from not only repeated patient-clinic visits, but also from patient complaints, which in extreme cases could lead to legal action, and a subsequent toll on practice resources.

With this in mind, it is not surprising that the demands on research and technical capabilities have been faced with increasing pressure. This pressure is projected into the various realms contributing to personalized clinical diagnostics, treatment and prevention. More specifically, researchers are being demanded to identify analyte targets more swiftly and quantitatively. In turn, diagnostics are increasingly required to provide higher throughput and enhanced diagnostic capabilities (cheaper, more precise and reliable) aiming to better understanding fundamental cell behavior. This insight can be applied to develop increasingly personalized medicine while also enabling pharmaceuticals to develop and test promising treatments more succinctly.

Given the current demands, an insurgence toward techniques capable of molecular-specific analyses on whole biological processes has developed. Imaging techniques have displayed particular promise from their ability to provide molecule-level analysis in the context of a tissue-size scale while providing a degree of quantification. Moreover, imaging techniques lend themselves nicely to personalized medicine, enabling more precise diagnosis and subsequent treatment. However, most current imaging techniques require elaborate sample preparation, the use of exogenous labels and provide poorly quantifiable results. Associated labeling techniques also require cumbersome protocols, making them often more costly and can result in non-specific sample binding, increasing the likelihood of false-positives. With this in mind, novel techniques circumventing these set-backs, like micro-Raman spectroscopy and FT-IR, are in great demand.

3.2 Raman Spectroscopy

Raman scattering was first discovered in 1928[1], where it was described as the 'molecular diffraction of light'. This form of photon scattering was found to differ in energy and signal intensity from Rayleigh scattering, with Raman scattering occurring in only every 1 in 10^6 – 10^8 photons. Without delay, Raman spectroscopy found a position in the chemical and materials analysis field, studying mixtures, pure substances, identifying compositions and characterizing chemical structures. As little to no sample preparation is required, samples could be non-invasively studied, lending the technique to a wide variety of applications.

It was not until the advent of the laser in the 1960's that Raman spectroscopy was capable of providing constant and intense light for sample excitation under reproducible conditions. Following this development, detection electronics also became considerably more efficient and hence compatible with smaller sample volumes. From the wealth of multivariate information in a single Raman spectrum and the ability to better assess small sample components non-invasively and non-destructively, exploratory applications involving biological matter were initiated. As biological endeavors grew in prevalence, tailored instrumentation, laser wavelengths and sample preparation became the focus of scrutiny.

Although reproducible conditions could now be achieved, biological samples possessed their own related drawbacks. These samples are often present in limited quantities, possess heterogeneous composition and compartmentalized targets, require microscopy, and produce high auto-fluorescence. This results in complex spectra and often difficult spectral deconvolution. These areas of concern have been addressed through the enhancement of associated instrumentation and also novel techniques for spectral evaluation like multivariate data analysis, better suiting studies of this nature and aiding the development of the micro-Raman spectroscopy widely used today

3.2.1 Raman Scattering

In context to the generally better known absorption spectroscopies, the excitation of energy levels in Raman proceeds via a 'detour'. In microwave, infrared or uv/vis absorption spectroscopy, the intensity loss at specific wavelengths is detected. This photon absorption happens when the energy difference between two levels matches a wavelength of the source. This is valid for all levels namely rotational, vibrational and electronic levels and is illustrated in Figure 3.1 for a vibrational level that corresponds to an infrared absorption. In the same figure the quantum state picture of Raman spectroscopy for the same vibrational levels is shown.
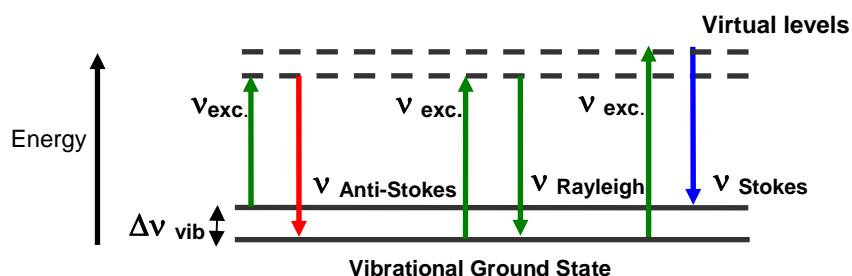
Figure 3.1 Induced excitation states of molecules via Stokes, Rayleigh or Anti-Stokes excitation patterns. Following laser excitation, molecules are excited to short-lived virtual states and return to their ground state by photon emission. Emitted photons can be of higher energy than incidence light (Anti-Stokes) or of lower energy than incidence light (Stokes) or of equal energy (Rayleigh scattering). In the case of absorption spectroscopies, incident energy is compared with the transmitted energy, indicating the amount of energy absorbed at a certain wavelength.

In contrast to absorption spectroscopy, where either a broadband excitation is used or the wavelength is scanned over the entire range of interest, for Raman spectroscopy a monochromatic light source is required. If this monochromatic source is far from a resonance, most of the photons will not interact with the sample, which is generally the case for transparent media. Nevertheless, a few photons excite the molecule in a so-called virtual level. From that level, most photons are simply reemitted at the same wavelength giving rise to elastic or Rayleigh scattering, a radiation that can also be detected orthogonal to the excitation direction. Even fewer photons are reemitted at wavelengths shifted in energy with respect to the excitation. The amount of the difference in energy is exactly the difference between the initial state and the final energy level of the molecule and is called Raman scattering. Most often, this is used for vibrational spectroscopy, but

the same arguments hold for rotational or electronic energy levels as specific selections rules must be considered as well.

The quantum mechanic level description is straight forward for visualizing the involved energy levels. Classic theory can also be used to understand the processes and the molecule properties that influence the intensity of Raman lines. Firstly, the incoming electromagnetic field (E) acting on a target molecule must be characterized for a specific time by a frequency (ω_0) and amplitude (E_0):

$$E \; = \; E_0 \cdot \cos \omega_0 t \qquad \qquad \textbf{1}$$

Any electromagnetic field (E) consequently induces an electrical dipole (μ) (2), where α refers to the polarisability of the molecule.

$$\mu \; = \; \alpha \cdot E \qquad \qquad \textbf{2}$$

If the oscillation of an electromagnetic field (1) is combined with the induction of a dipole (2), the dipole then oscillates with respect to the field (3).

$$\mu \; = \; \alpha \cdot E_0 \cos \omega_0 t \qquad \qquad \textbf{3}$$

On top of the oscillating induced dipole, the molecule also vibrates either in its ground state or also higher excited states. A vibrating molecule can be expressed as:

$$q \; = \; q_0 \cdot \cos \omega_R t \qquad \qquad \textbf{4}$$

ω_R is the resonance frequency of the vibrating molecule, where q_0 is the normal coordinate. In turn, the polarisability can now be expanded around q=0 using a Taylor expansion:

$$\alpha \;=\; \alpha(q) \;=\; \alpha(0) + \left(\frac{\partial \alpha}{\partial q}\right)_{q=0} \cdot q + \dots \qquad \textbf{5}$$

This expression for the polarisability can now be inserted into formula (3) for the dipole oscillation, as follows:

$$\mu \;=\; \left[\alpha_0 + \left(\frac{\partial \alpha}{\partial q}\right)_0 q_0 \cos \omega_r t\right] E_0 \cdot \cos \omega_0 t \qquad \textbf{6}$$

Expanding the term above, it can be rewritten as:

$$\mu \;=\; \alpha_0 E_0 \cos \omega_0 t + \frac{1}{2}\left(\frac{\partial \alpha}{\partial q}\right)_0 q_0 E_0 \cos(\omega_0 - \omega_R)t \qquad \textbf{7}$$

$$+\frac{1}{2}\left(\frac{\partial \alpha}{\partial q}\right)_0 q_0 E_0 \cos(\omega_0 + \omega_R)t$$

In this formula, the first term corresponds to elastic scattering as it is not influenced by the vibration of the molecule, the second and third terms refer to inelastic scattering. In particular, the second term refers to the red shifted stokes Raman scattering and the third term to the blue shifted anti-stokes Raman scattering. Hence, formula (7) readily explains the distinct Raman band positions of individual molecules.

The intensity of molecular polarisability can also be classically obtained using the emitted power of a hertzian dipole since it is also valid for induced dipoles (8).

$$I \; = \; \frac{\omega^4}{32\pi^2\epsilon_0 c^3}\mu_{ind}^2 \qquad\qquad \mathbf{8}$$

The induced dipole (2) can be combined with the above formula to obtain the intensity of molecular polarizability and is displayed as follows:

$$I \; = \; \frac{\omega^4}{32\pi^2\epsilon_0 c^3} \cdot \alpha^2 \cdot E^2 \qquad\qquad \mathbf{9}$$

For the Stokes portion of Raman scatting, $\omega = \omega_0 - \omega_R$ must be inserted to describe the induced oscillating dipole and the squared field is equal to the intensity, hence:

$$I_{Stokes} \; = \; const \cdot I_0 \cdot (\omega_0 - \omega_R)^4 \cdot \alpha^2 \qquad\qquad \mathbf{10}$$

For the classical calculation of scattering intensities, α must be replaced with δ_α / δ_q.

$$I_{Stokes} \; = \; const \cdot I_0 \cdot (\omega_0 - \omega_R)^4 \cdot \left(\frac{\partial \alpha}{\partial q}\right)^2 \qquad \mathbf{11}$$

From formula (11), it can be noticed that apart from molecular properties influencing the polarisability of the molecule, the Raman intensity depends directly on the intensity of the excitation source and on the fourth power of the excitation frequency. The latter dependency has practical aspects as a change in excitation wavelength from eg. 800 nm to 400 nm is accompanied by a 16-fold increase in scattering intensity. Practically, this can be difficult to directly monitor as spectral dependencies of instrumentation can influence the observed scattering. Other aspects like electronic resonances must also be considered before merely blue-shifting the Raman excitation to increase the intensity.

3.2.2 Raman Spectral Data

Since the difference in energy between incident and excited photons corresponds to a transition in molecule state, energy levels and resulting Raman spectra are unique for each molecule[2]. Even though Raman scattering produces a fairly weak overall signal, signal intensity depends on bond strength as well as quantity present. Raman spectra are then displayed as scattered intensity for the y-axis versus the relative shift in energy in wavenumber (cm^{-1}) for the x-axis. This representation is independent of the actual excitation wavelength used to excite the molecules and represents the differences in eigenstates of the absolute energy states of a molecule[3].

Here, the vibrational Raman spectra of benzene, deuterated benzene and a mixture of both are shown (Figure 3.2). This example visualizes not only the effect of isotopic labeling, but also how an assignment of different compounds can be made simply by a comparison of known spectra.
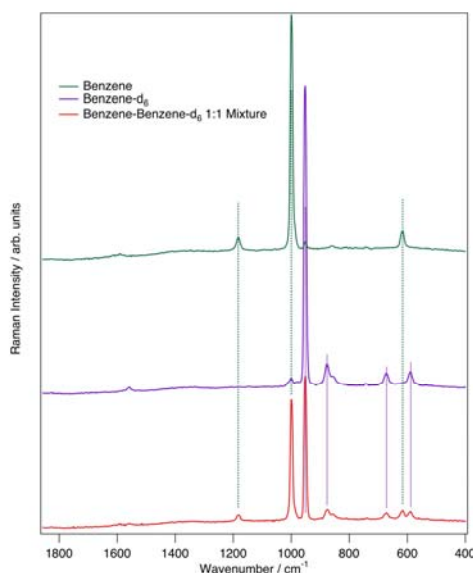
Figure 3.2 Raman spectra of benzene, deuterated benzene and a mixture of both substances.

Even though Raman scattering produces a fairly weak overall signal, signal intensity depends on bond strength as well as mass. In the case of benzene, shown in Figure 3.2, the intense band around 1003 cm^{-1} is attributed to ring breathing, whereas the smaller features at 606 cm^{-1} and 1178 cm^{-1} result from CH- bending vibrations[4]. For deuterated

benzene, these features are all present with an isotopic shift. The most intense band at 1003 cm^{-1} can be seen at the lower wavenumber 997 cm^{-1} and results from the mass difference of H vs D. The smaller features can also be seen to have shifted to lower wavenumbers in the deuterated benzene sample due to the same reasons. When solutions are combined, features from both benzene and deuterated benzene samples can be clearly identified, illustrating the importance of proper referencing.

3.2.3 Coupling Raman Spectroscopy with Microscopy

The microscope has long been an ideal platform for sample analysis, allowing the region of interest to be targeted. The incorporation of confocal microscopy with Raman spectroscopy revolutionized the scope of adaptations and in 1990 was first applied to study single cells and chromosomes[5]. This pairing simplified biological studies and enabled a 3-dimensional image translation and magnification of the sample relative to the microscope objective. Moreover, the confocal pinhole inflicts a geometry that ensures only select photons are collected from the back-scatter, reaching the detector. This precision enhances the ability to quantify spectra by providing spatio-temporal information of their origin, useful in identifying and quantifying specific localities.

By guiding a laser through an objective lens, a near-diffraction limited spatial resolution and increased collection efficacy can be achieved[6]. The laser beam can be made much tighter, increasing the intensity per area and can provide a spatial resolution below 1 μm, enabling biologically important structures including individual nuclei, mitochondria, cilia and regions of cell-interaction to be analyzed[7-10]. The minimally invasive micro-Raman process maintains sample integrity and direct sampling in either air or aqueous environments can be carried out maintaining viability. Raman micro-spectroscopy can also provide confocal resolution with appropriate wavelength selection, permitting measurements on different planes below the sample from a reduced absorption of the laser by the sample[11].
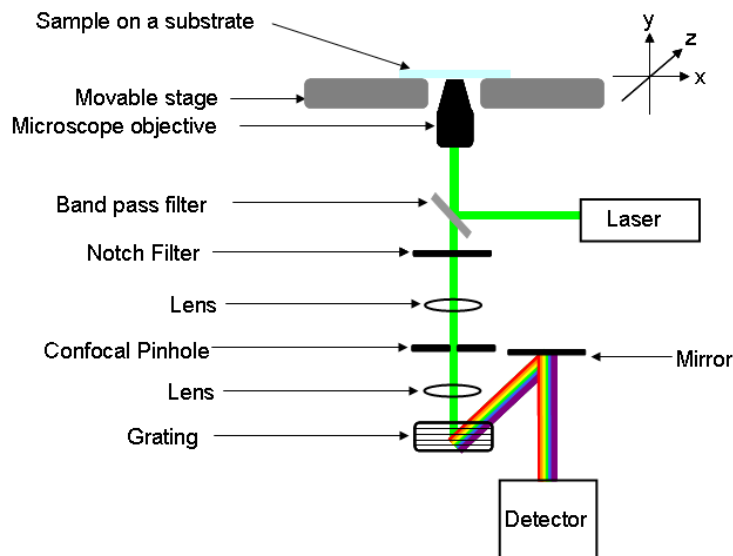
Figure 3.4 Instrumentation for a Micro-Raman Spectroscopy set-up to conduct sample imaging. The collimated laser light is directed through a band pass filter with appropriate wavelength selection and is focused through a microscope objective onto the sample. The backscattered light is collected through the objective and after filtering with a Notch filter to reject elastically scattered signal, the light is transmitted through the confocal pinhole into the spectrometer. The signal is then directed onto a grating which disperses the light and eventually guided onto the detector to collect the Raman spectrum.

Most micro-Raman spectroscopic measurements implement a confocal setup, exciting and collecting the backscatter from the same location using the 180° collection geometry (Figure 3.4). High numerical apertures provide increased Raman performance but can be hindered by spherical aberrations[6].

The innovation of micro-Raman spectroscopy has enabled the collection of detailed information pertaining to analyte molecular structure and composition on multiple focal planes. Micro-Raman spectroscopy continues to be a growing area of research, providing a spatial resolution surpassing that of IR spectroscopy and providing quantitative chemical insight. Its versatility can be best observed by the broad range of applications like the characterization of molecular structure in biological samples (e.g. cells, tissues) and distinguishing differences between cells as a result of growth cycles, physiological behavior or even physiological states (e.g. activation states)[12].

Through technological advancements, fully automated *xy* maps and line scans can now be collected of selected sample areas, upholding the spatial resolution of the analyte requisite for both single cell and full tissue analysis. A sampling region is broken into a series of pixels that are color coordinated based on the height of a chosen peak area (Figure 3.5).
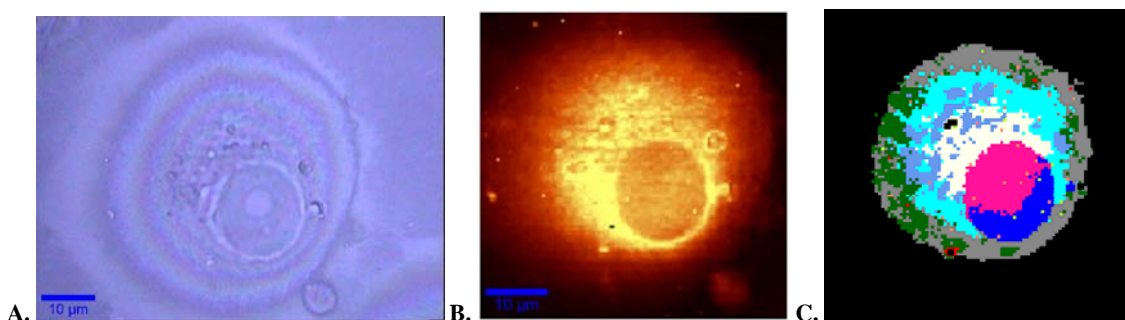
Figure 3.5 Micro-Raman imaging of a single MCF-7 cell and subsequent quantitative analysis[13]. An image is mapped by an automated stage and computer system duo. Each pixel can possess an individual spectrum and the total mapped spectra are compared by the signal intensity of a selected band. Intensities are assigned a color in relation to intensity (blue = high intensity, red = low intensity) and the image is converted into a spectral map. **A & B)** Visible image of an MCF-7 cell and chemical imaging specific for the intensity of CH- stretching throughout the cell (80 x 80 pixels and a 0.5µm spot size). **C)** Hierarchical clustering of the spectral image specific for the 'fingerprint region' (1800-675cm^{-1}) displays the localities of sub-cellular components.

Spectroscopic imaging of cells is still a new and exciting area of research, although shows great promise to provide novel ways of interpreting samples. As a result, both micro-Raman spectroscopy and micro-Raman imaging possess great potential for use in diverse applications.

3.2.4 Benefits of Raman Spectroscopy

Interest in Raman spectroscopy has grown considerably over the past 20 years. Attractive features include its non-invasive and non-destructive nature, in addition to no sample dilutions or extensive preparation necessary (Table 3.1). Raman spectroscopy also provides multivariate sample analysis, ideal for complex biological systems. Combined, these advantages illustrate the high sensitivity of Raman spectroscopy and its likelihood to accommodate a range of sample types and their respective industries.

Foremost, the good spatial resolution employed by Raman spectroscopy (1-100 µm) permits studying individual species and their structures in complex samples. This is an attribute specifically advantageous for single cell and imaging studies, something more difficult with related techniques like IR.

Advantages also include the ability to work using aqueous solutions in conventional glassware and the opportunity to monitor reactions, particularly when stretching vibrations are involved. For pharmaceutical studies on drug activity, this is tremendously beneficial. Final product conformations can also be maintained and their activity can be studied in their natural environment, shedding light onto *in vivo* compound reactions. Moreover, as most drug active molecules contain a degree of un-saturation, producing a strong signal in the Raman 'fingerprint region' between 400- 2000 cm^{-1}, detecting symmetrical stretching provides a significant advantage over IR spectroscopy.

Imaging Techniques	Spatial Resolution	Sample Preparation	Molecular Probe Use	Visualized Target	Information Obtained	Acquisition Time	Cell to Result Time	Quantification	Ref.
Micro-Raman Spectroscopy	Approx. 500 nm	Not required	N/A	Proteins, RNA/DNA, lipids, carbohydrates	Chemical composition	Milli-Seconds-Hours; dependent on sample size	Min. – Hours	Absolute & Relative	2, 14
Fluorescent In-Situ Hybridization	N/A	Chemical & formalin fixation, labeling	DNA primers conjugated to a fluorophore	DNA & RNA sequences, chromosomes	Gene sequence presence	Min. – Hours	Min. – Hours	Absolute & Relative	14
Immunohistochemistry	N/A	Formalin fixation, labeling	Antibodies for cell labeling	Cell constituent localization	Proteins	Min.- Hours	Min. – Hours	Relative	15
Atomic Force Microscopy	Atomic resolution	Intermolecular forces & sample immobilization	N/A	Sample Mapping, including whole cell surface & individual components	Topographical & nm scale structural information	Min.	Min.	N/A	16
Electron Microscopy	Approx. 5 nm	Cryo or chemical fixation, gold sputtering, dehydration, sectioning	N/A	Proteins & Cells	Protein Structure, Cell conformations	Seconds	Min.-Hours	Relative	17
Multi-Photon Microscopy	15-1000 nm	Chemical fixation, sectioning	Rhodamine amide, quantum dots, fluorescent proteins, dyes	Visualization of cell structures	Structural & topographical information	Seconds	Min.-Hours	Relative	18, 19
Tip- Enhanced Raman Spectroscopy	5-50 nm	Tip preparation	N/A	Proteins, RNA/DNA, lipids, carbohydrates	Chemical composition	Seconds-Min.; dependent on sample and tip	Min.-Hours	Relative	20, 21
Secondary Ion Mass Spectrometry - SIMS	50 nm	Cryopreservation	N/A	Whole cells, intracellular structures	Molecular &/or elemental composition of the sample	Seconds-Min.	Min.-Hours	Absolute & Relative	22, 23
Maldi-Imaging	Down to 500 nm	Sectioning & MALDI-matrix application	N/A	proteins, peptides, metabolites, biomarkers	Drug development, biomarker characterization,	Min.-Hours	Min.-Hours	Relative	24-26

Table 3.1 Imaging techniques and their quantification capabilities. Micro-Raman spectroscopy, FISH, FT-IR, Immunohistochemistry, AFM, Electron Microscopy, Multi-Photon Microscopy, SIMS and Maldi-Imaging are all prevalent imaging techniques, whilst TERS and CARS are novel spectroscopic additions to these imaging techniques.

3.3 IR Spectroscopy

Although the advantages of Raman spectroscopy have been clearly elucidated in the previous section, the application of Raman's sister technique IR spectroscopy can be better suited to larger samples. IR spectroscopy is known as the sister technique to micro-Raman from its ability to provide corresponding spectral data by following a different series of selection rules. The infrared region of the electromagnetic spectrum includes 3 regions: the near-, mid- and far- infrared regions based on their proximity to visible light. Conventional IR spectroscopy typically applies mid- infrared light (4000-400 cm^{-1}) and is useful in studying fundamental vibrations and structural composition.

While Raman spectroscopy is based on light scattering from molecules, IR spectroscopy is based on absorption and molecular dipoles. When infrared radiation interacts with different forms of matter, the radiation is absorbed when it matches a specific energy transition. This incident radiation that is absorbed by the matter results in fewer photons being transmitted. These transmitted photons are sent to a detector for spectral development and subsequent analysis.

As stated, IR radiation must match a specific molecular vibration for an absorption process, exploiting the many modes that molecules can rotate. Energy levels are related to the common wavenumber scale, with higher 'wavenumbers' (cm^{-1}) equating to higher energy levels. The overall absorption frequencies are determined by the molecular potential energy surface shape, the associated vibronic coupling and the atomic mass. As molecules have *N* atoms, allowing in general *3N* degrees of freedom. The vibrational modes of molecules account for *3N-6* degrees of freedom (except for linear molecules with 3N-5), displaying the number of ways the atoms in a molecule can vibrate[27]. All molecules show typical vibrational modes, making the IR spectrum specific to the molecule, as with Raman spectroscopy. For a molecule to be IR-active, a change in its permanent dipole must occur.

For more complex samples like cells, many bonds will absorb the IR radiation, enabling multiple vibrations to occur related to their respective chemical groups[27]. An example of such an occurrence can be seen when looking at the types of vibrations from a common group, like methylene (CH_2). As the H- atoms are bound on either side of the C-, six different frequencies can occur following absorption of IR radiation. These include symmetrical and anti-symmetrical stretching, wagging, rocking, twisting and molecular scissoring (Figure 3.6).

Symmetrical Stretching

Rocking

Antisymmetrical Stretching

Twisting

Scissoring

Wagging
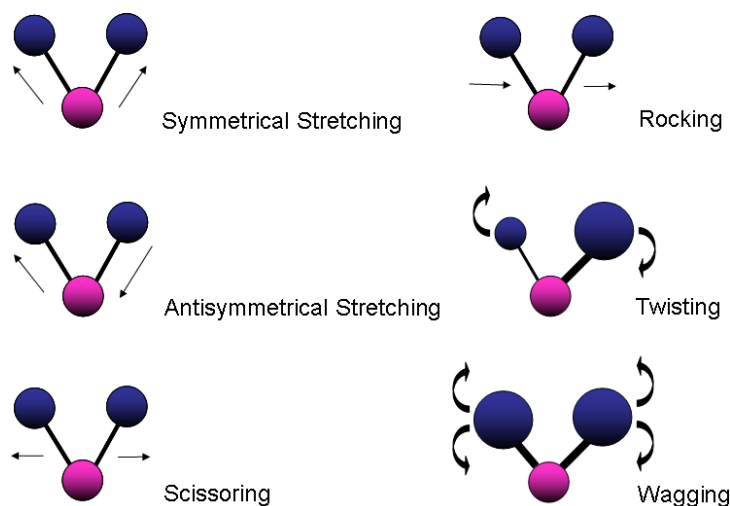
Figure 3.6 The six different types of vibrational modes of CH_2 that are detected in an IR spectrum. A common example of such vibrations can be noticed with CH_2 group vibrations, as they are commonly found in many organic compounds like lipids, and undergo all six of these different vibrations.

These individual frequencies possess characteristic IR absorbance frequencies and are visualized through plotting all of the absorbance frequencies. The resulting 'spectrum' can be displayed in either ' % Transmission' (%T) or 'Absorbance' (A) mode. A %T spectrum displays where the IR radiation was transmitted, meaning where there was no absorbance and the radiation was 100% transmitted through the sample. On the other hand, an A spectrum displays the same chemical information but is based on where the radiation was absorbed and how much, depending on the intensity of the dipole change (Figure 3.7).
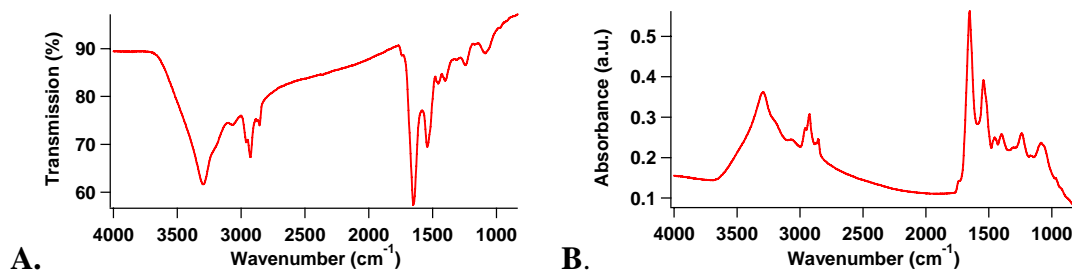
Figure 3.7 (A) An example of a cell spectrum in % Transmission (T%), while (B) displays an example of a cell spectrum in Absorbance. The y-axis units are different based on what the spectral plot is displaying. For spectra in T%, the y-axis reaches 100% for complete absorption of the IR radiation, while for Absorption spectra, the y-axis represents the amount of IR radiation absorbed at each wavenumber.

Molecules that do not have a change in dipole moment are termed infrared inactive. In the case of a CO_2, its symmetric stretching mode does not undergo a change in the dipole moment, making it IR-inactive (the vibration is still Raman active). Meanwhile, the asymmetric stretch of CO_2 does undergo a change in dipole moment, thus enabling it to absorb IR radiation and produce an IR-active spectrum. Another IR-inactive molecule is the diatomic molecule N_2, from its lack of dipole moment and how, even when stretching, a dipole moment is not produced.

3.3.1 FT-IR Instrumentation

The most commonly applied method of IR spectroscopy is Fourier-Transform IR (FT-IR) from its ability to measure all the IR frequencies simultaneously by using an interferometer to collect an interferogram of the sample signal and digitize the signals for downstream use. Standard FT-IR instrumentation begins with an interferometer. This interferometer prepares the IR radiation source for sample analysis. The most prevalent type of interferometer is the Michelson interferometer configuration. These interferometer configurations only differ by incorporating a movable mirror in the place of one of the stationary mirrors in the Michelson configuration (Figure 3.8).
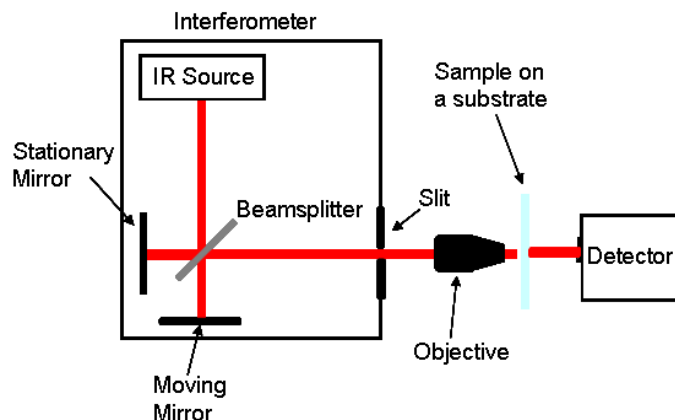
Figure 3.8 Instrumentation for a FT-IR set-up to conduct sample imaging. The IR source is sent through a half-silvered mirror in the interferometer, allowing half of the beam to be reflected off of a stationary mirror while the other beam half reflects off of a moving mirror to introduce a time delay. Both beams rejoin and are reflected through an objective and onto the sample for absorption. The resulting IR beam that results following sample absorption is then transmitted through a slit into the monochromator to ensure other wavelengths are not present and is reflected onto a grating to disperse the beam into its respective wavelengths which continue on to the detector for spectral compilation.

To begin with, an IR radiation source is channeled through a beam-splitting mirror that is half reflective and half transmissive (half-silvered), splitting the beam into two parts. One half will be reflected at a 90° angle and the other will continue through the mirror until it reaches an oscillating mirror. This moving mirror will completely reflect the IR beam 180°, introducing a time delay in the beam, and it will continue until it reaches the beam-splitter, where it interferes with the beam reflected from the stationary mirror and is then reflected towards the sample. The other half of the incident IR radiation beam was reflected to a stationary mirror, where it will also be reflected 180°. Both beams will rejoin past the beam-splitter, referred to as the transmitted beam, and will continue through to the sample. The induced time delay in the temporal coherence of one of the beams is used to measure the time delay at each setting, allowing the time variable to become a spatial coordinate for subsequent FT by the following formula (12) into a spectrum.

$$S(t) = \int_{-\infty}^{\infty} I(v)e^{-iv2\pi t}\,dv \qquad \textbf{12}$$

The above formula compiles all the contributing frequencies from the molecular vibrations to provide a signal S(t) in the form of time. Continuing this, a subsequent formula can be used to provide a non-zero value in the case of S(t) containing a variable that is equivalent to the oscillating function, as shown in formula (13), while remembering formula (14).

$$I(v) = 2\,\mathrm{Re}\int_{-\infty}^{\infty} S(t)e^{2i\pi vt}\,dt \qquad \textbf{13}$$

$$e^{ix} = \cos\chi + i\sin\chi \qquad \textbf{14}$$

Following sample analysis, the varying percent of the beam transmitted is sent into a detector for subsequent plotting and digitization. The signal variations with respect to the moveable mirror are detected producing an 'amplitude vs. length' plot that can undergo a FT for deconvolution of the amplitude waves, producing an 'intensity vs. cm^{-1}' plot.

3.3.2 Benefits of FT-IR

One of the most prevailing advantages of FT-IR is its quantitative capability. Although micro-Raman spectroscopy can provide quantitative data as well, FT-IR analysis implements a much stronger signal quality for spectral acquisition and subsequent quantification. Understanding the Beer-Lambert Law provides the foundation to the quantitative capabilities of FT-IR, where transmittance of a sample at a known wavelength is described as the ratio of the radiant power that is given off from the back-end of a sample of an identical wavelength to the incident radiation power. This is described as shown in formula (15).

$$T(v) = \frac{I(v)}{I_o(v)} = \exp[-\alpha(v)b]$$ **15**

For this formula, b refers to the sample thickness, while $\alpha(v)$ is the linear absorption coefficient at v[28]. With this in mind, it is crucial to emphasize that the absorbance of a sample is directly correlated with the sample concentration and the refractive index of the sample. Hence, the window must also be integrated for an accurate assessment.

In addition to FT-IR being capable of providing quantitative sample insight, it also provides high-throughput sample analysis. Larger sampling regions can be rapidly mapped when compared with micro-Raman spectroscopy, making it a nicely suited technique for preliminary sample screening prior to further analysis of regions of interest using a higher spatial resolution. Moreover, FT-IR provides a higher signal-to-noise ratio then micro-Raman spectroscopy, enabling the reliable detection of less prevalent components for downstream use in analyses methods.

3.4 Conclusion

Since discovery, Raman and FT-IR have become a valuable means of sample analysis, propelling the area of spectroscopy to new heights. Coupled by the development of commercially available lasers, interferometers and FPA detectors, modern day Raman and FT-IR have grown into innovative and highly attractive techniques. Attributes like their intrinsic multivariate nature, little to no sample preparation and non-invasive analysis make these technique appealing for studies ranging from chemical compound analysis to tissue architecture[29, 30]. This flexibility permits the analysis of samples in various states, including solids, gases, aerosols, vapors and liquids, in addition to *in situ* measuring.

As discussed, the need to better understand individual cell mechanisms and their relation to larger scale systems like whole tissues has become critical. This notion has increased in particular importance for the development of more specific therapies, personalized diagnostics and even preventative medicine. With these demands, the ability to obtain

data pertinent to molecular composition and maintain the spatial-temporal analyte distribution in context of the whole sample through imaging (tissue or cell monolayer) while preserving the sample for downstream analysis has become vital. The joining of spectroscopy with microscopy has also enabled the breadth of applications to expand considerably in the direction of the bio-medical sciences, filling the current caveat in bio-analysis and bio-medical diagnostics.

This combination has lead to the quantitative, non-invasive analysis of specific localities or the imaging of whole samples, providing a resolution below the micrometer level while maintaining spatio-temporal organization. From its high resolution and chemical-rich spectra, accurately filtering the many intrinsic spectral components of spectra has lead to the development of multiple algorithms to de-convolute heterogeneous samples and provide quantitative insight. Although absolute quantification of raw spectral data remains complicated to achieve, relative quantification can be readily achieved.

For single spectrum analyses, applying methods like band deconvolution can assist in relative sample evaluation[31]. Absolute quantification with respect to sample heterogeneity versus molecular quantity can be achieved with imaged samples by applying methods like hierarchical cluster analysis (HCA) and principle component analysis (PCA). Through the use of hyper-spectral data clustering methods and the sensitivity of these spectroscopic techniques, sample heterogeneity can be clearly visualized and measured with a theoretical single molecule limit of detection.

As micro-Raman and FT-IR spectroscopy gain acclaim in bio-medicine and significant spectral databases are developed, quantification capabilities are likely to develop synergistically. In turn, as the potential for quantification expands and the need to understand fundamental cell behavior on a 'systems' level, vibrational spectroscopy will continue to deliver in bio-medical applications.

References

1. C. Raman and K. Krishnan, *Nature*, 1928, **121**, 501.
2. K. E. Shafer-Peltier, A. S. Haka, J. T. Motz, M. Fitzmaurice, R. R. Dasari and M. S. Feld, *J Cell Biochem Suppl*, 2002, **39**, 125-137.
3. P. Crow, J. S. Uff, J. A. Farmer, M. P. Wright and N. Stone, *BJU Int*, 2004, **93**, 1232-1236.
4. D. Whiffin, *Proc. Phys. Soc. A.*, 1956, **69**, 375-380.
5. G. J. Puppels, F. F. de Mul, C. Otto, J. Greve, M. Robert-Nicoud, D. J. Arndt-Jovin and T. M. Jovin, *Nature*, 1990, **347**, 301-303.
6. M. Pelletier, *Analytical applications of Raman spectroscopy*, Blackwell Publishers, Oxford, England, 1999.
7. J. C. Timlin, A; Morris, MD, *Appl Spectrosc*, 1999, **53**.
8. E. Paschalis, E. DiCarlo, F. Betts, P. Sherman, R. Mendelsohn and A. Boskey, *Calcif Tissue Int*, 1996, **59**, 480-487.
9. M. Kazanci, P. Roschger, E. Paschalis, K. Klaushofer and P. Fratzl, *J Struct Biol*, 2006, **156**, 489-496.
10. Y. Huang, T. Karashima, M. Yamamoto and H. Hamaguchi, *Biochemistry*, 2005, **44**, 10009-10019.
11. C. K. Krafft, M; Beleites, C; and G. S. Schackert, R, *Analytical and bioanalytical chemistry*, 2007, **389**, 1133-1142.
12. M. Diem, M. Romeo, S. Boydston-White, M. Miljkovic and C. Matthaus, *Analyst*, 2004, **129**, 880-885.
13. M. D. Mariani, PJR and V. Deckert, *Integrative Biology*, 2009, **(submitted)**.
14. T. Taton, C. Mirkin and R. Letsinger, *Science*, 2000, **289**, 1757 - 1760.
15. J. Levsky and R. Singer, *J Cell Science*, 2003, **14**, 2833.
16. C. Taylor and R. Levenson, *Histopathology*, 2006, **49**, 411-424.
17. G. Murphy and G. Jensen, *Biotechniques*, 2007, **43**, 413-417.
18. R. Weissleder, *Nature Rev Cancer*, 2002, **2**, 11-18.
19. J. Fölling, V. Belov, D. Riedel, A. E. Schönle, A, C. Eggeling, M. Bossi and S. Hell, *Chem Phys Chem*, 2008, **9**, 321-326.
20. T. Deckert-Gaudig, E. Bailo and V. Deckert, *J. Biophotonics*, 2008, **1**, 377-389.
21. E. Bailo and V. Deckert, *Chem Soc Rev*, 2008, **37**, 921-930.
22. T. L. Colliver, C. L. Brummel, M. L. Pacholski, F. D. Swanek, A. G. Ewing and N. Winograd, *Anal Chem*, 1997, **69**, 2225-2231.
23. T. P. Roddy, D. M. Cannon, Jr., C. A. Meserole, N. Winograd and A. G. Ewing, *Anal Chem*, 2002, **74**, 4011-4019.
24. P. Chaurand, J. Norris, D. Cornett, J. Mobley and R. Caprioli, *J. Proteome Res*, 2006, **5**, 2889-2900.
25. M. Reyzer and R. Caprioli, *Current Op. Chem. Bio.*, 2007, **11**, 29-35.
26. A. Maarten Altelaar, I. Taban, L. McDonnell, P. Verhaert, R. de Lange, R. Adan, W. Mooi, R. Heeren and S. Piersma, *Int. J. Mass Spectrom.*, 2007, **260**, 203-211.
27. B. Smith, *Fundamentals of Fourier transform infrared spectroscopy*, CRC Press, Florida, 1996.
28. P. Griffiths and J. de Haseth, *Introduction to Vibrational Spectroscopy*, Wiley, New York, 2007.

29.   J. Laserna, *Signal Expressions in Raman Spectroscopy*, Wiley, New York, 1996.
30.   C. K. Krafft, T; Funk, RHW; Salzer, R, *Anal Chem*, 2006, **78**, 4424-4429.
31.   G. Thomas Jr and D. Agard, *Biophys J*, 1984, **46**, 763-768.

Chapter 4

Real-Time Reverse Transcriptase Quantitative Polymerase Chain Reaction (RT-qPCR) & Associated Benefits With Imaging Correlation

4.1 Analysis of Nucleic Acids

The current understanding of living organisms, their functionality and their development continue to require clarification as many fundamental mechanisms remain to be elucidated. In turn, molecular classification of tissue samples and techniques facilitating sensitive and trustworthy nucleic acid quantification can be turned to with the hopes of revealing these caveats[1]. Genetic studies applying techniques focusing specifically on gene variations, microsatellite presence, single nucleotide polymorphisms and deletions can supply invaluable information pertinent to phylogeny, gene flow, overall predispositions, gene involvement, overall diagnosis and treatment choice [2-5].

4.2 Background

Polymerase chain reaction (PCR) was first described by Powell et al. in *Cell* in 1987[6] and enables the detection of RNA transcripts down to the single copy. For the detection of individual gene sequences, PCR exploits the capabilities of two enzymatic activities. The first enzymatic activity does not occur within the PCR plate itself; rather it applies an RNA template-dependent DNA polymerase called reverse transcriptase to the extracted RNA sample prior to the PCR reaction to develop a complimentary DNA (cDNA) target through the process of reverse transcription (RT). This cDNA molecule is complimentary to the RNA target through its possession of complimentary nucleotide components and strand polarity (Figure 4.1). This cDNA is then used as the PCR target for gene sequence detection.
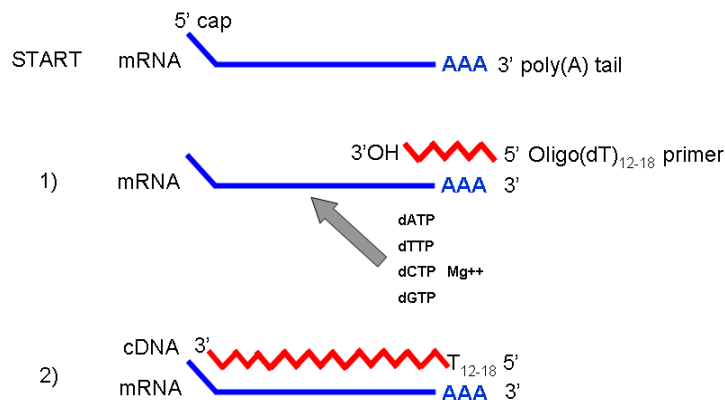
Figure 4.1 Reverse Transcription (RT) of mRNA into complimentary DNA (cDNA) for PCR analysis. The mRNA is extracted from the analyte and used as a template to produce cDNA during reverse transcription, which takes place at 65º and is deactivated at 95º. Deoxyribonucleoside triphosphate's (dNTP's) are added to supply the nucleotides for cDNA synthesis in a balanced buffer solution. dATP: 2'-deoxyadenosine 5'-triphosphate, dTTP: 2'-deoxytimidine triphosphate, dCTP: deoxycytidine 5'-triphosphate, dGTP: 2'-deoxyguanosine 5'-triphosphate.

The second enzymatic reaction is based on amplifying the cDNA target sequence with a DNA polymerase. To do this, the PCR assay must be compiled. This includes the previously synthesized, analyte-specific cDNA sample, and the specific primers that bind to the target gene sequence (amplicon). This is all combined within a reaction buffer, often referred to as the 'Master Mix', that provides an optimal balance between the DNA Taq polymerase, dNTPs (dATP, dTTP, dGTP, dCTP), nuclease-free water and $MgCl_2$ to support the amplification process.

Following the combination of all reagents, basic PCR target amplification was carried out using a standard thermal cycler and PCR products were detected by ethidium bromide staining and subsequent 1-dimensional gel separation. However, as technology improved and quantification became increasingly important, PCR was modified to enable higher throughput sample processing and improved PCR product quantification.

This new generation of instrumentation provided a more efficient heating block and a laser or halogen lamp for sample detection based on absorbance for quantification (q) coupled with a computer for real-time detection. For absorbance detection, transcripts were bound to a fluorescing target such as an intercalating dye like SYBR® Green or to

fluorescent-labeled probes that bind the amplion between the primers of the amplicon sequence. These will activate fluorescence resonance electron transfer (FRET), producing fluorescence detectible by the passing monochromatic incident laser (typically $\lambda = 532$ nm) or a halogen lamp. In turn, the development of real-time reverse transcriptase quantitative PCR (RT-qPCR) began.

To carry out RT-qPCR, all components must be combined into the PCR plate wells and undergo a series of heating and cooling cycles within a real-time thermal cycler (Figure 4.2). The cooling cycle (often 45º) will enable the activity of the Taq polymerase to elongate the amplicon, where the polymerase will polymerize the amplicon beginning with the 3' end of the primer. This will lead into the probe, causing fluorescence resonance electron transfer (FRET) for laser detection.
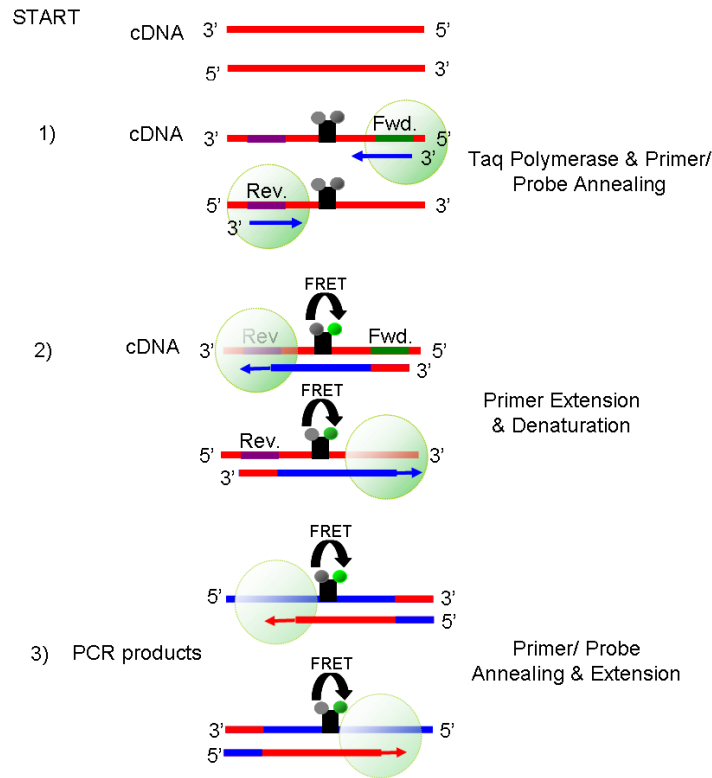
Figure 4.2 PCR amplification. Single stranded cDNA is denatured at the start to ensure all targets are unbound. This allows primer and probe annealing to the amplicon. The Taq polymerase then binds and commences elongation of the amplicon (1). The elongation process is completed when the Taq reaches the end of the amplicon and the temperature is increased to inhibit Taq activity and denature the newly formed PCR products from the cDNA templates (2). Following PCR product denaturation, the heating and cooling cycles will cycle through again, allowing the new targets to be amplified, displaying the exponential amplification process in PCR. Theoretically, following each PCR cycle (steps 1-2) the PCR product is doubled, with an efficiency rate near 70%[7].

Following the elongation of the target amplicon, the sample will be heated (60 ºC) to inactivate the Taq polymerase activity and denature the newly formed double stranded DNA. This permits all newly synthesized amplicon templates to separate from the cDNA and be used in the next round of elongation as a template. This cycle of cooling and heating will continue up to approximately 40 cycles (instrumentation dependent) and with higher concentrations of target amplification, more PCR product will result.

Resulting PCR amplification is then plotted based on the amount of fluorescence detected at each cycle number (x-axis) and by the logarithm of the cDNA target (y-axis) resulting

in the form of a sigmoidal curve. These curves display three stages of amplification, a lag (stochastic phase), exponential and plateau phase[8]. The lag phase is largely due to the sensitivity of the instrument and is accounted for by setting a 'threshold bar' just above the background fluorescence at the beginning of the exponential phase (Figure 4.3).
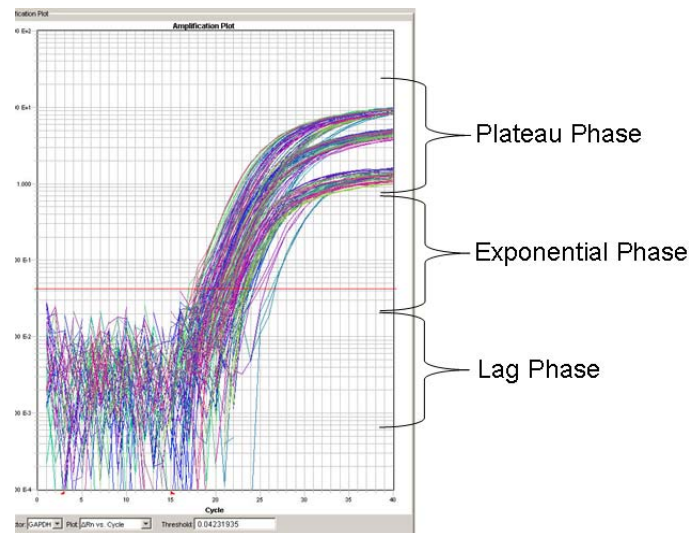
Figure 4.3 Example of a PCR product amplification plot. The red line denotes the 'Threshold Bar' where the cycle threshold (Ct) values are recorded from for each candidate gene. This is manually placed just above the background fluorescence (lag phase) and toward the beginning of the exponential phase to identify which cycle PCR product fluorescence reached the threshold.

4.2.1 Data Processing

RT-qPCR data can be processed by means of absolute quantification or relative quantification. Absolute quantification implements template oligonucleotides and the development of standard curves to determine the copy number of a particular mRNA target relative to an external standard[9].

The more commonly applied method of RT-qPCR data analysis is through relative quantification from its theoretically superior analytical capabilities[9]. Relative quantification applies the target mRNA copies detected through amplification to an internal standard, which are typically two previously selected reference genes based on their overall expression stability for the specific sample. With respect to selection of the

reference genes, RT-qPCR is slowly moving away from ubiquitously applying glyceraldehyde 3-phosphate dehydrogenase (GAPDH) or β-actin (ACTB) as the reference gene or transcript in qPCR-related assays. The energetic activity and structural compositions across cell types and within cell populations have been found to be inconsistent, making the expression of these particular genes vary by cell.

In turn, the selection of more stable reference genes by means of gene-array screens[10] or literature searches, assay screening and analysis in bio-analytical software, like *geNorm*[®], has been shown to determine more stable reference genes. These bio-analytical softwares compare a) the difference between amounts of reference transcript and those of test transcripts from a nominated reference sample to b) the same difference observed in all other tested samples. With this known, a thorough study by Vandesompele et al. in 2002[11], identified a series of 12 frequently stable genes that could be screened with varying samples to optimize the selection of internal sample normalizer genes[12]. Since this publication, these 12 genes have been frequently screened for their stability among different samples and have enabled the selection of more suitable reference expression profiles, alleviating the need to know the standard concentration for quantification.

The corresponding Ct values of the selected reference genes are used to normalize the Ct values of the candidate genes and are then displayed as a ratio, obviating the need to determine mRNA concentration. To carry-out relative quantification, the amount of amplified molecules at the threshold must be determined while considering the target gene and the reference genes, and can be expressed by formula (1).

$$X_T = T_0(1 + E_T)^{C_{T,T}} = K_T \qquad 1$$

In this formula, X_T represents the total number of target copies at the threshold, while E_T is the amplification efficiency and $C_{T,T}$ is the threshold level. Once this is known, the copy number of the normalizing gene can also be assessed (2).

$$X_R = R_0(1+E_R)^{C_{T,R}} = K_R \qquad 2$$

With X_T and X_R, the ratio of the candidate gene copies compared with the reference gene copies at the selected threshold can be determined through the formula below (3).

$$T_0 / R_0 = K(1+E)^{C_{T,R}-C_{T,T}} \qquad 3$$

In carrying out relative quantification, some assumptions are included, particularly with respect to the degree of fluorescence released following target amplification and the efficiency of PCR amplification. However, studies have found these variables differ to a negligible degree and do not influence downstream quantification[9].

4.2.2   Applications

Direct benefits to clinical diagnostics will be achieved as a result of technical advancements in quantitative analysis of the transcriptome[13]. Interests in deoxyribonucleic acid (DNA) and messenger ribonucleic acid (mRNA) detection and quantification have improved current knowledge of cell functions, including cell regulation, growth, expression markers, and transcription[14]. The polymerase chain reaction (PCR) is one such research technique in mainstream clinical diagnostics that can provide quantitative analysis and assist in closing the "bench to bedside" gap found with translational medicine[15].

Applications of RT-qPCR include a variety of areas in medical disciplines, including viral diagnostics[16,17], peripheral blood specimens and disease-specific translocations[18-22] and investigations of minimal residual disease expressly among follicular lymphoma and acute lymphoblastic leukemia[23,24]. From this unparalleled sensitivity, RT-qPCR can provide reproducible detection of genetic components spanning from very low expression to very high expression, enabling changes in cell behavior to be acutely explored.

4.2.3   Correlation With Imaging

As research enters the post-genomic era with profound knowledge surrounding genetic codes[25], protein studies have become increasingly prevalent. Although proteins represent the outcome of genetic coding, the many steps leading to protein synthesis and folding structures still pose difficulties for protein-based therapeutic and diagnosing targets[26]. The rapidly emerging field of molecular imaging, particularly with biophotonic techniques like vibrational spectroscopic methods, provides the capability to identify molecular fluctuations and phenotypical shifts within cell samples[27]. By combining vibrational spectroscopic imaging with quantitative gene expression analyses, it has become possible to track changes in cells using a systems approach while obtaining spatial and temporal resolution[28]. Using this top-down approach, protein targets can be discerned and sequence-specific molecules can be readily designed by exploiting the Watson-Crick nucleic acid base-pairing[29]. These sequence-specific molecules can be designed to target one of the stages involved in protein synthesis for detection or therapeutic applications[30, 31].

4.3 Conclusion

Understanding the link between fundamental cell interests and associated interactions within healthy tissue and wounded tissue environments can be better explored by identifying genes involved in accurate tissue regeneration and applying them to studies focusing on deformities like fibrosis onset, elucidating potential mechanisms and predispositions involved. Through the use of RT-qPCR and vibrational spectroscopic imaging, novel insight into primary cell organization and cell interactions within tissue can be detected and ultimately applied to the development of innovative treatments and potential forms of prevention, while advancing the current understanding of elemental cell behavior.

References

1. K. Dettmer, P. A. Aronov and B. D. Hammock, *Mass Spectrom Rev*, 2007, **26**, 51-78.
2. S. M. Haig, *Ecology*, 1998, **79**, 413-425.
3. D. Paetkau, G. F. Shields and C. Strobeck, *Mol Ecol*, 1998, **7**, 1283-1292.
4. F. Palomares, J. A. Godoy, A. Piriz and S. J. O'Brien, *Mol Ecol*, 2002, **11**, 2171-2182.
5. K. F. Becker, C. Schott, S. Hipp, V. Metzger, P. Porschewski, R. Beck, J. Nahrig, I. Becker and H. Hofler, *J Pathol*, 2007, **211**, 370-378.
6. L. M. Powell, S. C. Wallis, R. J. Pease, Y. H. Edwards, T. J. Knott and J. Scott, *Cell*, 1987, **50**, 831-840.
7. R. Cha and W. Thilly, *Genome Res.*, 1993, **3**, S18-S29.
8. C. T. Wittwer, M. G. Herrmann, A. A. Moss and R. P. Rasmussen, *Biotechniques*, 1997, **22**, 130-131, 134-138.
9. S. Bustin and T. Nolan, *Data Analysis & Interpretation*, International University Line, La Jolla, CA, 2006.
10. F. J. Hoerndli, M. Toigo, A. Schild, J. Gotz and P. J. Day, *Anal Biochem*, 2004, **335**, 30-41.
11. J. Vandesompele, K. De Preter, F. Pattyn, B. Poppe, N. Van Roy, A. De Paepe and F. Speleman, *Genome Biology*, 2002, **3**, RESEARCH0034.
12. L. Fink, W. Seeger, L. Ermert, J. Hanze, U. Stahl, F. Grimminger, W. Kummer and R. M. Bohle, *Nat Med*, 1998, **4**, 1329-1333.
13. S. A. Bustin, *J Mol Endocrinol*, 2002, **29**, 23-39.
14. C. Ramachandran and S. J. Melnick, *Mol Diagn*, 1999, **4**, 81-94.
15. G. Burrow, *Clinical and Investigative Medicine*, 1988, **11**, 315-320.
16. M. Schutten and H. G. Niesters, *Expert Rev Mol Diagn*, 2001, **1**, 153-162.
17. I. M. Mackay, K. E. Arden and A. Nitsche, *Nucleic Acids Res*, 2002, **30**, 1292-1305.
18. A. Hochhaus, A. Reiter, H. Skladny, A. Reichert, S. Saussele and R. Hehlmann, *Recent Results Cancer Res*, 1998, **144**, 36-45.
19. J. Gabert, *Haematologica*, 1999, **84 Suppl EHA-4**, 107-109.
20. M. Eder, K. Battmer, S. Kafert, A. Stucki, A. Ganser and B. Hertenstein, *Leukemia*, 1999, **13**, 1383-1389.
21. M. Emig, S. Saussele, H. Wittor, A. Weisser, A. Reiter, A. Willer, U. Berger, R. Hehlmann, N. C. Cross and A. Hochhaus, *Leukemia*, 1999, **13**, 1825-1832.
22. E. Olavarria, E. Kanfer, R. Szydlo, J. Kaeda, K. Rezvani, K. Cwynarski, C. Pocock, F. Dazzi, C. Craddock, J. F. Apperley, N. C. Cross and J. M. Goldman, *Blood*, 2001, **97**, 1560-1565.
23. T. Szczepanski, *Leukemia*, 2007, **21**, 622-626.
24. A. Tysarowski, A. Fabisiewicz, E. Paszkiewicz-Kozik, J. Kulik, J. Walewski and J. A. Siedlecki, *Acta Biochim Pol*, 2007, **54**, 135-142.
25. E. M. Southern, *J Mol Biol*, 1975, **98**, 503-517.
26. M. Rudin, *Curr Opin Chem Biol*, 2009, **13**, 360-371.
27. T. F. Massoud and S. S. Gambhir, *Genes Dev*, 2003, **17**, 545-580.

28.   Y. Shav-Tal, R. H. Singer and X. Darzacq, *Nat Rev Mol Cell Biol*, 2004, **5**, 855-861.
29.   S. Bhaumik, Z. Walls, M. Puttaraju, L. G. Mitchell and S. S. Gambhir, *Proc Natl Acad Sci U S A*, 2004, **101**, 8693-8698.
30.   A. C. Stephens, *Curr Opin Mol Ther*, 2003, **5**, 336.
31.   L. Joos, E. Eryuksel and M. H. Brutsche, *Swiss Med Wkly*, 2003, **133**, 31-38.

Chapter 5

Impact of Fixation On *in vitro* Cell Culture Lines Monitored With Raman Spectroscopy

5.1 Introduction

As Raman spectroscopy continues to break into cell biology and biomedical diagnostics, increasing importance is being placed on methodology standardization. Specific to sample preparation, although live samples can be imaged using Raman spectroscopy, live measurements no longer suffice when the time from sampling to analysis exceeds the desired timeframe. In this case, sample preservation is necessary to preserve biochemical conditions for prolonged time periods.

Sample preparation for spectroscopic analysis can include chemical fixation or non-chemical preservation methods like air-drying or desiccation, as some form of sample preparation is always necessary. Although a wide variety of chemical fixation methods are available *ad hoc*, conventional methods in biomedical research are not suitable for spectroscopic analysis. Recurrent fluctuations in band intensities, contamination from fixatives and the ever-present auto-fluorescence can mask diagnostically useful information. Accordingly, optimized fixation methods for cultured cells are necessary, to ensure that the sample integrity is maintained close to the native or physiological state whilst minimizing auto-fluorescence.

Cultured cell sample preservation methods and their spectroscopic effects remain largely unexplored although are the first method of sample handling prior to analysis, creating a window where samples can be modified from their original state. Some noteworthy endeavors from a few groups have focused on fixation methodologies, summarized in Table 5.1.

Table 5.1 Recent studies focusing on the effects of sample fixation and preservation. CPD-Critical-Point Drying

Sample	Technique	Fixative	Specimen	Effects	References
Tissue	Near-Infrared Raman	Formalin	Human Bronchial Tissue	Tissue macromolecules found to produce major spectral bands Consistent decline in overall spectral intensity Decline due to formalin disruption of bronchial lipid self-assembly Formalin peaks identified in normal tissue samples	32, 33
	Raman	Tissue Drying Formalin Snap Freezing	Normal Hamster Tissue	Tissue drying disrupted protein vibrational modes Formalin did not contaminate spectrum	34
	IR & Raman	Formalin	Cervical Tissue	Formalin peak identified Loss of amide I intensity due to alteration of secondary amide to tertiary amide Reduction in overall signal intensity	31
	FT-IR	Ethanol Formalin Methacrylate Embedding	Foetal Rat Bone Tissue	Ethanol resulted in aminde I and II alterations from modifications in protein conformation	36
Cultured Cells	FT-IR	Formalin Acetone	Vero cells	Similar to unfixed Acetone fixation lead to loss of spectral features, lipid band loss and amide I and II bands modified	35
	Synchrotron FT-IR	Formalin Formalin & CPD glutaraldehyde-osmium tetroxide-CPD	Prostate Cancer-3 cells	Formalin found to produce no significant effects Formalin+CPD did not preserve cytoplasmic lipids well Glutaraldehyde-osmium tetroxide-CPD preserved a greater fraction of cytoplasmic lipid to formalin + CPD	37

Although tissue samples of varying origin were examined using both FT-IR and Raman, the overwhelming conclusion from these studies indicated that formalin tissue fixation lead to a reduction in band intensity[1-4]. This decline resulted from the disruption of lipid assembly and by modification of amide band intensities from changes in protein conformations. Furthermore, the addition of a formalin peak was observed at 1490 cm^{-1} [1].

Chemical tissue drying by means of ethanol or acetone was also examined by Hastings et al.[5] with Vero cell monolayers and by N.L. Pleshko[6] with fetal rat bone tissue samples using FT-IR. Both studies showed conformational modifications in the protein content, influencing the amide I and II bands. Acetone drying in particular was found to reduce the overall lipid band intensities.

Gazi et al.[7] continued to assess the effects of sample preservation. Using synchrotron radiation FT-IR, they examined the prostate cancer cell line PC-3 preserved using formalin, formalin with subsequent critical-point drying (CPD), and glutaraldehyde-osmium tetroxide-CPD. No considerable effects of the

formalin fixation on the IR spectra of single cells were observed. Moreover, the cytoplasmic lipid content was better preserved by formalin fixation and glutaraldehyde-osmium tetroxide-CPD fixation.

The aim of sample fixation is to preserve the structural and biochemical constituents of the cell to mimic their *in vivo* states. During fixation, cells loose their internal water content that is bound to internal macromolecules and consequently internal structures can collapse, leading to a delocalization of bio-molecules. This is caused by the large surface tension occurring from the water-air interface passing through the cell[7] and is highly detrimental to the resulting spectra. Additionally, once cells are removed from media, autolytic processes continue until fixation. Autolysis is the process of degradation initiated by internal enzymes, like lipozomes and lysosomes. Proteins become denatured, mononucleotides and phospholipids dephosphorylate, nuclear fragmentation commences and the cytoplasm condenses. All this can severely influence the study of intracellular biochemical pathways.

Formalin is a widespread chemical fixative that causes the cross-linking of the primary and secondary amine groups of proteins[8] and can preserve lipids by the reaction of hydrated formalin with double bonds of unsaturated hydrocarbon chains[7]. In conjunction with two other commonly used methods of sample preparation, air-drying and desiccation, this study sought to determine the most consistent method of preservation for two human cell lineages of varying origin with Raman spectroscopy[9].

5.2 Methods

5.2.1 Cell Culture. Human dermal derived keratinocyte (HaCaT; ECACC, UK) cells and human peripheral macrophages (MM6; DSMZ, Germany) were grown at 37 ºC with a constant humidified atmosphere of 5% CO_2 in air. HaCaT cells were cultured in Dulbecco's Modified Eagle's Medium (DMEM) and supplemented with 10% Fetal Calf Serum (FCS), 1% Penicillin/ Streptomycin (P/S) and 2mM L-Glutamine & non-essential amino acids (NEAA). MM6 cells were cultured in 24-well plates containing RPMI-1640, supplemented with 10% FCS, 1% P/S, 2mM L-Glutamine & NEAA, 1 mM Sodium Pyruvate and 10 µg/ml human recombinant insulin. All reagents and culture media were purchased from Gibco, Germany.

HaCaT cells were cultured until confluent directly onto 1 cm diameter quartz substrates (QCS GmbH, Germany) pre-cleaned using HCl and dried in a desiccator. MM6 cells were classically activated (C.A) using lipopolysaccharide (LPS) (Sigma-Aldrich, Germany) at 1 µg/ml for 24 hours[10]. Once confluent, media was carefully removed, causing all cells in suspension to settle onto quartz substrates.

5.2.2 Cell Sample Preparation. All quartz cell samples were removed from media and washed with 1 ml Phosphate Buffer Saline (PBS). Air-dried samples were left in half open Petri-dishes to allow sample drying in ambient conditions for 1 hour, while preventing sample disruption by dust and debris. Cell samples for desiccation were placed in a desiccator containing silica gel beads for 1 hour under ambient pressure. Remaining samples were lightly fixed using a combination of 10% formalin, sterile PBS and ultra-pure H_2O producing a 2% formalin solution (Sigma-Aldrich, Germany) for 1 hour. Following treatment, all samples were wrapped in aluminium foil and stored at -20 ºC until analysis.

5.2.3 Raman Measurements. Raman measurements were collected using a micro-Raman setup (HR LabRam inverse, Jobin-Yvon-Horiba, Bensheim, Germany). A frequency doubled 532 nm Nd:YAG laser (Coherent Compass, Dieburg, Germany) was used for excitation, providing 1mW incident power at the sample. The entrance slit was set to 100 μm and a 300 rules/mm grating was used. The laser was focussed onto the sample using a Leica PLFluoar objective (NA 0.75), providing a 0.8 μm focal spot. Raman scattering was detected with a CCD camera operating at 220 K (Panasonic, Germany). All measurements were carried out under ambient conditions and instrumentation was calibrated prior to the actual experiments to the 636 cm^{-1} Titanium Oxide spectral peak. In total, 72 acquisitions were collected from each sample. Integration times were optimized for each sample (see Figure 2). Measurement locations were alternated throughout the cell to include any location dependant spectral variances and differences in the cell cycle.

5.2.4 Cell Staining. Following Raman analysis, all cell samples were stained using hematoxylin and eosin (H & E) histological stains (Sigma-Aldrich, Germany) for the nucleus and cytoplasm following standard methods.

5.2.5 Data Analysis. Raman spectra were all pre-processed. All spectra were smoothed using a moving average with a third-order polynomial and then transformed with a Savitzky-Golay 2nd derivative convolved with a 13-point smoothing function. Spectra were mean-centered and then compared by cross-validating PCA using 6 PC's. PCA data analysis was carried out in Unscrambler software (Camo, Norway). Average raw spectra were calculated for each sample and compared in Igor (Wavemetrics, USA).

5.3 Results & Discussion

Figures 5.1A through 5.1C show visible light microscope images of HaCaT cells for each fixation method on quartz. Figures 5.1G through 5.1I show visible light microscope images of C.A.MM6 cells on quartz disks for each specific fixation method. Examination of these representative visible light microscope images indicate no significant morphological differences in cell structures resulting from the different fixation methods.
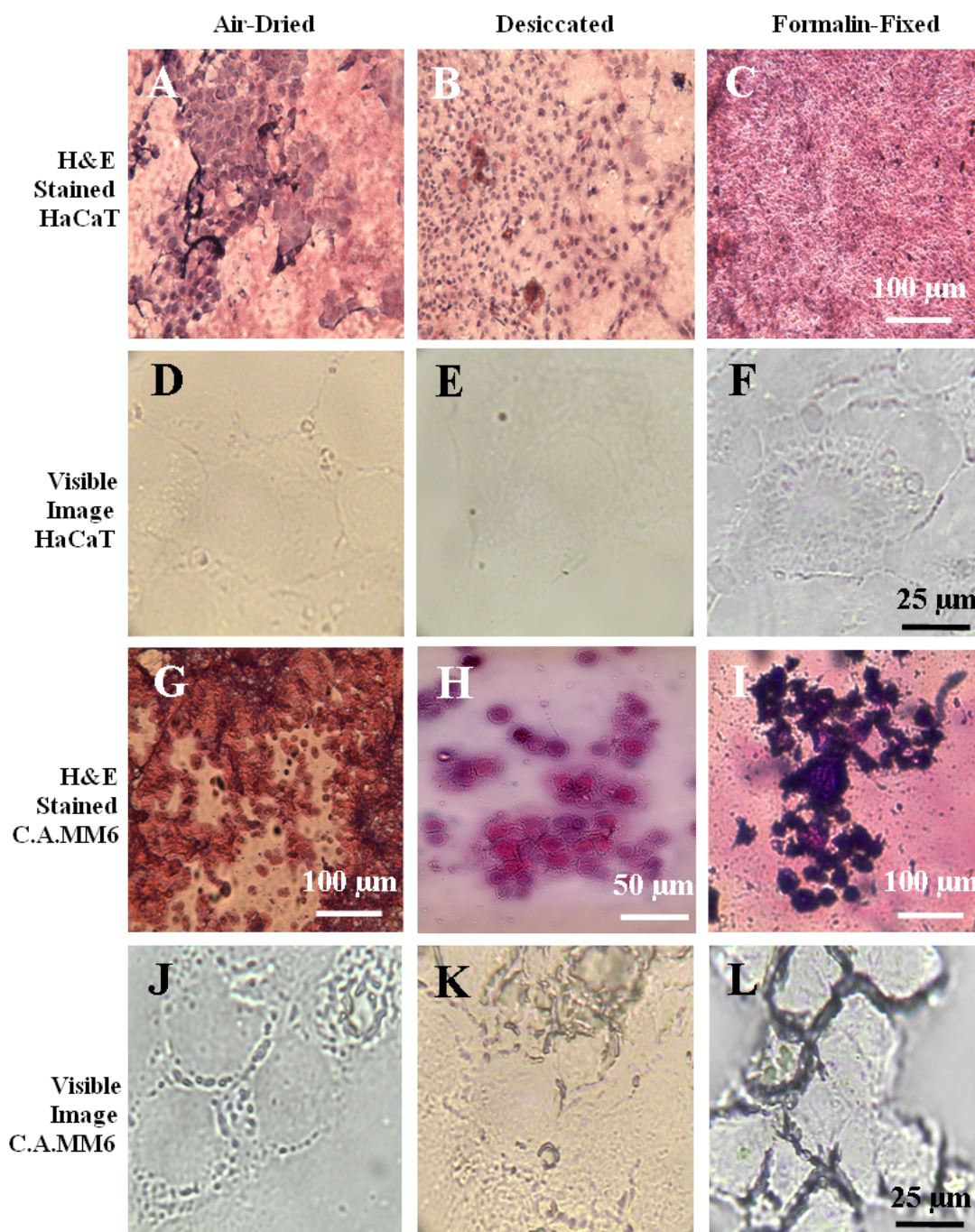
Figure 5.1 (A) Average spectra of air-dried (A), desiccated (B) and formaldehyde fixed (C) HaCaT cells. **(B)** The average spectra of air-dried (A), desiccated (C) and formalin-fixed (B) C.A.MM6 cells are shown. All cells were cultured onto quartz substrates, washed in ultra-pure H_2O and chemically fixed or dried (air or desiccation) for 1 hour. Spectra were collected from the cell wall, cytoplasm and nucleus to account for region specific spectral variations and differences in cell cycles. In total, eight cells were measured, providing 72 spectra per cell type for each fixation method. The laser spot size was 0.8 μm and a grating at 300 was used. The laser power at the sample was 1 mW. All spectra were pre-processed with 3 point smoothing and transformed using a 2nd derivative. Spectra were then averaged and plotted.

The corresponding H & E staining for all cell samples of both cell lines varied in staining ability. Air-dried HaCaT samples did not stain easily due to detaching of the typically adherent cells from the quartz. Remaining cells were found to stain well but lacked overall consistency when compared with desiccation and formalin fixation. Formalin fixed HaCaT cells displayed widespread pink coloring and largely unclear nuclear localities, indicative of non-specific staining from the loss of nuclear integrity. Desiccated cell samples displayed the most preserved cell structure and reproducible H & E staining.

Desiccated C.A. MM6 cells also displayed the most preserved morphology following H & E staining compared with other preservation methods. Air-drying and formalin fixation resulted in cell detachment from the quartz substrate and also displayed non-specific staining indicative of internal component damage or degradation.

5.3.1 Raman Spectra of HaCaT Monolayer Samples Using Varied Preservation Methods

Average cell spectra for each fixation procedure are displayed below (Figure 5.2).
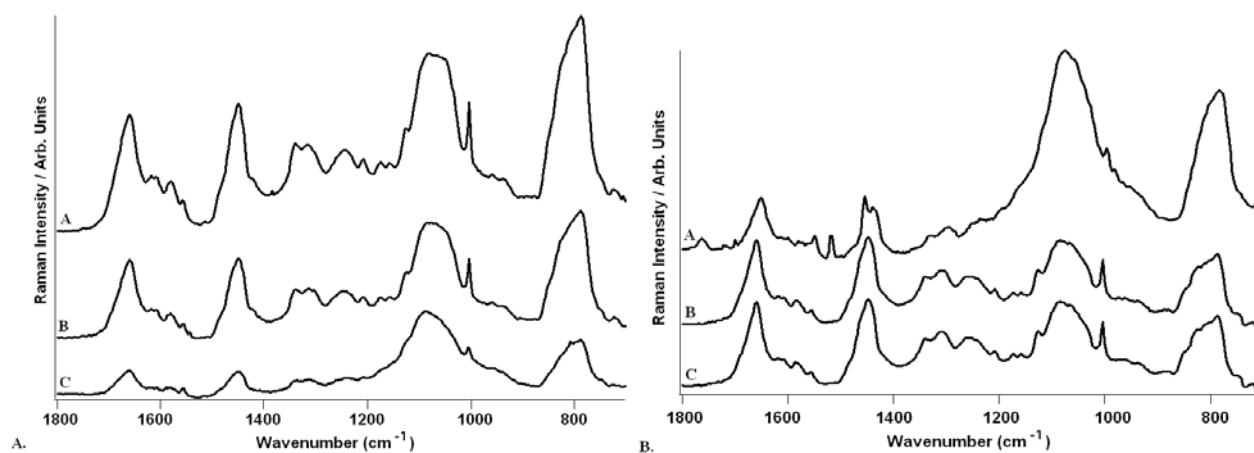
Figure 5.2 The effects of fixation methods on cell preservation were visualized with H & E stains and light microscope images. Cells were cultured or allowed to settle directly onto quartz substrates and then chemically fixed, desiccated or air-dried. Visible images and H & E staining were carried out following sample analysis. Cell fixation methods impacted visible images to a negligible degree. However, cell fixation methods directly impacted cell component preservation and was visualized with H & E staining. These results confirm that preservation methods differ in efficacy between cell lines.

Spectral peaks in the 1800 - 700 cm^{-1} region were found to vary in intensity with fixation procedures. The best intensity for all components in HaCaT cells was detected in the air-dried sample. Both major and minor molecular contributions are clearly identified. Desiccation as a means of sample preservation produced a slightly less intense spectral profile when compared with air-drying, but

maintained the majority of the molecular contributions identified in the air-dried sample and no changes in position were observed. Air-dried and desiccated samples both maintained significant spectral features particularly in the 1600 - 1500 cm^{-1} region, attributed to C=C stretching, amide II and purine nucleic acid base presence.

The weakest overall spectrum was detected from the formalin-fixed HaCaT sample. This degradation could result from enzymatic activity of lipases and proteases considering formalin fixation does not inhibit all activity[11]. Here, many of the less intense features become largely unidentifiable, as noticed in the 1600 - 1500 cm^{-1} region. This decline in overall spectral intensity from air-drying to formalin fixation is indicative of degradation in general cellular constituent contributions like protein and lipid with this fixation method. H&E staining of the formalin fixed sample (Figure 5.1C) confirms this degradation from the stain bleeding. The purine base peaks for guanine and adenine (1577 cm^{-1})[4] and the amide II band (1555 cm^{-1})[12] also decline in intensity with desiccation and fixation methods, compared to the air-dried approach.

The spectral range of 1448 - 1127 cm^{-1} displayed a substantial loss of information compared to air-dried or desiccated samples. In this spectral range, ribose C-O vibrational stretching (1167 cm^{-1})[13], α-helical (1259 cm^{-1})[14] and β-pleated (1223 and 1240 cm^{-1})[14, 15] sheet conformational changes can all be detected in the air-dried sample but become unidentifiable in the formalin fixed specimen. This disparity is indicative of changes in protein folding from poor overall sample preservation, permitting widespread protease activity. A decline in nucleic acid purine bases (1337 cm^{-1})[16] and lipid (1309 cm^{-1})[17] signals were both noticed in addition to a decrease in amide III (1245 cm^{-1})[18] vibrations. This decrease in amide III specifically points towards keratin presence, a widespread structural protein specific to keratinocytes. Furthermore, a decline of the signal at 1448 cm^{-1} was noticed. The intensity of this band relates to the amount of methyl groups present in the sample and also confirms both a decline in lipid hydrocarbon saturation[34] and, in general, overall inadequate sample fixation.

The reproducibility of the fixation methods was also confirmed by PCA. The original spectral data was combined, averaged and preprocessed prior to being decomposed by a standard PCA with six principle components. The scores plot and the associated loading vectors for principle components 1 and 2 are displayed in Figures 5.3A and B for all three HaCaT cell fixation methods. The total variance of spectral intensities on the wavenumber (cm^{-1}) axis was found to be 68% in the first principal

component (PC1) and 11% in the second principal component (PC2). The results clearly illustrate a clear discrimination based on the fixation protocol employed. Formalin sample fixation was shown to be the most consistent preservation method, indicated by the close replicate clustering. Despite the increased spectral intensity noticed in air-dried samples, this method was also the most inconsistent in overall fixation, compared with desiccation and formalin fixation. The desiccation protocol provided consistent sample clustering, indicating reproducibility. In total, only four of the 72 desiccated sample spectra clustered near to the air-dried samples. Desiccation also yields spectra in sufficient quality. Both major and minor bands were preserved, making desiccation the most consistent with Raman spectral analysis of the selected cell type.

Corresponding loadings for the PC1 (blue) versus PC2 (red) scores plot display the inter-method variations. Looking at this loadings plot, significant discrepancies within the 1800-700 cm^{-1} spectral region can be noticed. Bands of substantial variances between PC's include 1019, 1445 and 1657 cm^{-1} specific for DNA backbone C-O stretching[19], CH_2/ CH_3 bending deformations[20] and amide I intensity. These are also considerable fluctuations between 1361- 1120 cm^{-1}, pertinent to nucleic acid bases, lipids and amide III. These spectral differences all support the previously noted cell modifications associated with preservation techniques.
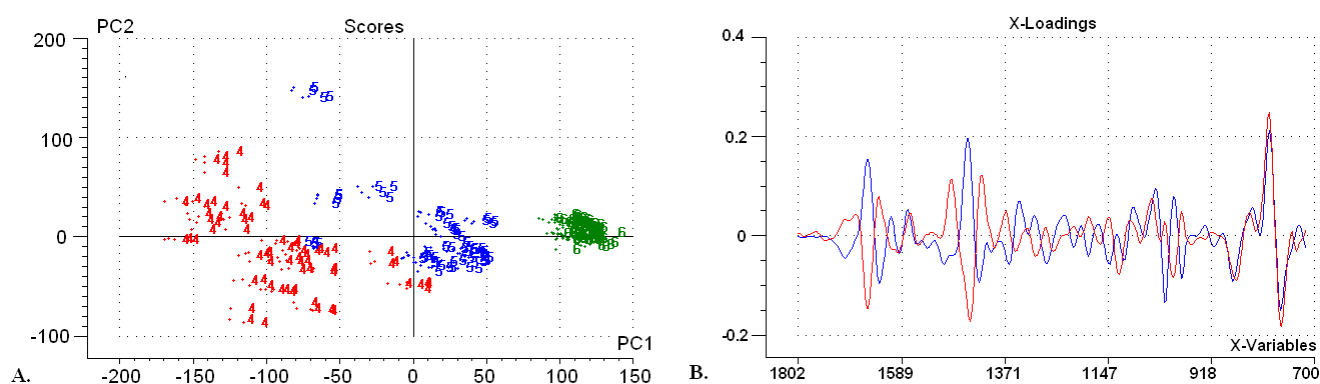
Figure 5.3 (A) Cross validated PC1 & PC2 results from Raman spectra of HaCaT cells on quartz using 3 preparation methods. Distinct clusters are exhibited for air-dried (red), desiccated (blue) or formalin-fixed (green) samples. Air-dried samples exhibited the most variability in sample preparation, while desiccation exhibited more consistent sample preservation. **(B)** Loading plot of PC1 (blue) and PC2 (red) display differences in the spectra from each sample.

5.3.2 Raman Spectra of C.A. MM6 Monolayer Samples Using Varied Preservation Methods

In contrast to the aforementioned HaCaT cells, the C.A.MM6 cells responded differently to the three preservation methods as the average spectra displayed in Figure 5.2B already show. Peaks in the 1800-700 cm^{-1} region were found to vary in intensity corresponding to the fixation procedures as shown with HaCaT cell samples. However, in the case of C.A.MM6 cells, the most intense spectra were from formalin fixation and desiccation. Air-drying was found to maintain the presence of stronger features, specifically at 1455 cm^{-1} for CH$_2$ deformations, at 1077 cm^{-1} for nucleic acid C-C vibrational stretching, C-O lipid stretching and PO$_2$ symmetric vibrational stretching modes[4]. At 1077 cm^{-1} specifically, a broad band is present that overshadows many of the lower intensity peaks in the desiccated and formalin fixed samples. This significant increase in C-C bonds can be attributed to plasma membrane saturated fatty acids. These saturated fatty acids become solid at room temperature, indicating vesiculation of the cell membrane lipid content, giving rise to the intense 1077 cm^{-1} peak. Literature suggests that saturated fatty acids are prevalent in activated cells for their importance in inducing pro-inflammatory cytokine secretion, indicating why such a peak would occur with air-dried C.A. MM6 cells and not with air-dried HaCaT cells[21, 22].

Lower intensity bands detected in the spectra of desiccated and formalin fixed samples from 1253 cm^{-1} to 1127 cm^{-1} specific for mostly lipid and protein constituents could not be identified in the air-dried sample. This absence further confirms protein and lipid degradation both on the cell membrane and within the cell, compromising overall cell structure integrity. This lack in preservation of cells from their natural state can also be noticed in the corresponding H&E staining, shown in Figure 1G, where signs of non-specific staining between the nucleus and cytoplasm occur corresponding to damage or degradation of internal components. All points considered, air-drying for C.A.MM6 cells was not found to be an adequate method of sample preservation.

In contrast to air-drying, formalin fixation and desiccation of C.A.MM6 samples produced comparable intense spectral bands. The 1600 - 1450 cm^{-1} region of both preparation methods contained spectral features not detectable in air-dried samples, like 1159 cm^{-1} for protein and carbohydrate vibrational C-O stretching[23] and 1127 cm^{-1} for C-C specific lipid stretching[18].

Distinct peaks at 1448 cm^{-1}, 1582 cm^{-1} and 1658 cm^{-1} were maintained throughout C.A.MM6 samples. The band at 1448 cm^{-1} is specific for deoxyribose deformations, the one at 1582 cm^{-1} for nucleic

acids[14, 24]. In combination both bands are good indicators for nucleic acid presence. The amide I at 1658 cm^{-1} and C=C vibrational stretching in unsaturated fatty acids, indicate a good preservation of overall cell structure[25]. Cell membrane and nuclear integrity was confirmed by H&E staining, where distinct nuclei and cell membranes can be noticed (Figure 5.1H, I).

Sample desiccation differed slightly from the spectra of formalin fixed samples, with less intense bands at 1612 cm^{-1} (proteins and nucleic acids) and 1180 cm^{-1} (cytosine, adenine, guanine)[16, 26]. This decrease in band intensity is indicative of a decline in overall protein and nucleic acid content, compared with the formalin fixed samples.

However, despite the preservation of many important strong and weaker spectral features in the C.A.MM6 cells with formalin fixation, overall reproducibility of this fixation method was found to produce significant inconsistencies. The reproducibility of each preservation method was again tested using a cross-validating PCA displayed in Figure 5.4A. Again, all original spectra were treated as previously described. The scores plot and the associated loading vectors for PC 1 and PC 2 are displayed in Figure 4A and B. The preservation of C.A.MM6 cells using three varied fixation methods was found to possess a total variance of spectral intensities on the wavenumber (cm^{-1}) axis by 80% in PC1 and 7% in PC2. The corresponding scores plots display a clear discrimination based on the fixation protocol employed.

The inconsistencies noticed in formalin fixation result from the differential distribution of cell surface proteins and lipid conformations present. This is particularly important for C.A.MM6 cells because activated cells express more proteins and undergo significant plasma membrane changes compared with non-activated cells[21]. Structural component organization and lipid conformations are also not identical between individual cells of same lineages. These inter-lineage differences will vary in response to fixation, leading to varied methylene protein cross-linking.

Corresponding loadings for PC1 (blue) versus PC2 (red) identify all variables involved with the majority of data variance present. These loadings display discrepancies throughout the 1800-700 cm^{-1} spectral region. Bands of substantial variances between PC's include 1708, 1674, 1337, 1315 and 790 cm^{-1}. These bands are specific for DNA base pairing vibrations[23], amide I β-pleated sheets[15], nucleic

acid purine bases[16], guanine[26] and PO_2 symmetric stretching from DNA[19]. These spectral differences support the changes in cell integrity from each preservation method.
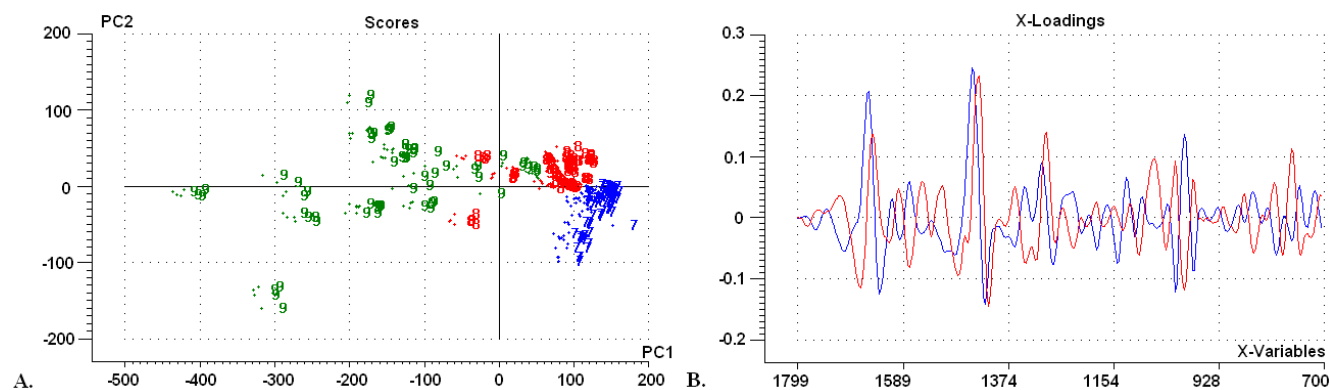
Figure 5.4 (A) Cross validated PC1 & PC2 results from Raman spectra of C.A.MM6 cells on quartz using 3 preparation methods. Air-dried (blue), desiccated (red) or formalin-fixed (green) samples exhibit distinct clusters. These clusters illustrate the varying effects of sample preparation. Formalin-fixed samples exhibited the most variability in sample preparation, while desiccation exhibited more consistent sample preservation. **(B)** Loading plot of PC1 (blue) and PC2 (red), illustrating differences within spectrum between samples.

In conclusion, air-drying and desiccation provided the most consistent preservation methods, indicated by their close replicate clustering. Despite the spectral intensity noticed in the average formalin- fixed spectrum, this method was the most unpredictable for sample preservation with C.A.MM6 cells. Sample desiccation provided good overall spectral intensity compared with formalin-fixation and air-drying. Desiccation also provided reproducible sample fixation. Therefore, desiccation provided the most ideal method of sample fixation for C.A.MM6 cells by maintaining cellular component structure for good overall spectra and by also being a consistent method of sample fixation.

5.3.3 Effects of Sample Preparation Methods Between Cell Lineages

The effects of sample preparation methods on different cell lineages were also assessed. Using an adherent cell line derived from the skin (HaCaT cells) and an activated non-adherent cell line from the peripheral circulatory system (C.A.MM6 cells), identical fixation procedures were tested. Results indicate that identical fixation methods do affect cells differently and depend largely on the individual cell constituents. C.A.MM6 cells possess increased structural and surface protein expressions and also undergo lipid rearrangements during activation. The complement cascade is essential for classical

activation[27] and is associated with the formation of antibody complexes and lectin binding[28]. Following antibody binding, subsequent peptide cleavages release cytokines and activate protease functions, leading to changes in surface receptors, antigens and changes in fatty acid composition[28]. Internal cell activity is also modified, demonstrated by less overall enzymatic activity and 5'-nucleotidase activity[29]. In turn, these morphological changes will respond differently to sample preparation methods, compared with an inactivated cell line.

On the whole, C.A.MM6 cells were found to be the most consistently fixed using air-drying and desiccation, whilst unprimed HaCaT cells were the most consistently fixed using desiccation and formalin fixation (Figures 5.3A and 5.4A). These fluctuations could result from differences between lineages in the lipid bi-layers and surface protein aggregation, particularly since surface proteins are not uniformly organized and will cross-link depending on their surface locations.

5.4 Conclusion

Cellular organelle, structural components and their relative changes are the focus of many biological studies. However, the ability to spectroscopically analyse live cells still provides distinct challenges and is not widespread in practice. In turn, selecting the ideal sample preparation method for sample analysis is critical for obtaining both sensitive and reproducible results.

Compared with previous Raman spectroscopy studies using cultured cells, formalin fixation was found to affect the cellular lipid and protein content[5, 7]. Here, both the average spectra and the corresponding PCA scores plots show clear disparities between sample preservation and cell line response.

From comparing different cell types with varying preparation methods, significant differences in overall sample preservation were observed and indicated that the standard method of formalin fixation is not necessarily ideal. Here, formalin fixation displayed results not as consistent as expected for a commonly used method. In comparison with previous Raman studies using formalin fixed tissue samples, formalin fixed cultured cell results were in agreement for one cell line tested (C.A.MM6 cells) but not for the other (HaCaT). Spectra for formalin-fixed HaCaT cells were weak compared with desiccated and air-dried samples, whereas C.A.MM6 cells possessed similar spectral intensities for both formalin-fixed and desiccated samples. These results confirm that cell responses to fixatives are cell line and morphological-state dependent from the variances in internal structure and membrane

components. As a result, sample desiccation was found to provide an ideal compromise between signal intensity and preservation in cell components.

References

1. E. O. Faolain, M. B. Hunter, J. M. Byrne, P. Kelehan, H. A. Lambkin, H. J. Byrne and F. M. Lyng, *J Histochem Cytochem*, 2005, **53**, 121-129.
2. Z. Huang, A. McWilliams, H. Lui, D. I. McLean, S. Lam and H. Zeng, *International journal of cancer*, 2003, **107**, 1047-1052.
3. Z. Huang, A. McWilliams, S. Lam, J. English, D. I. McLean, H. Lui and H. Zeng, *International journal of oncology*, 2003, **23**, 649-655.
4. M. G. Shim and B. C. Wilson, *Photochemistry and photobiology*, 1996, **63**, 662-671.
5. G. Hastings, R. Wang, P. Krug, D. Katz and J. Hilliard, *Biopolymers*, 2008, **89**, 921-930.
6. N. L. Pleshko, A. L. Boskey and R. Mendelsohn, *Calcif Tissue Int*, 1992, **51**, 72-77.
7. E. Gazi, J. Dwyer, N. P. Lockyer, J. Miyan, P. Gardner, C. Hart, M. Brown and N. W. Clarke, *Biopolymers*, 2005, **77**, 18-30.
8. J. Keiran, *Histological & Histochemical Methods: Theory & Practice, Ch.2*, Pergamon Press, Oxford, UK, 1990.
9. M. M. Mariani, P. Lampen, B. R. Wood, J. Popp and V. Deckert, *The Analyst*, 2009, **134**, 1154-1161.
10. F. Meng and C. A. Lowell, *The Journal of experimental medicine*, 1997, **185**, 1661-1670.
11. A. M. Seligman, H. H. Chauncey and M. M. Nachlas, *Stain Technol*, 1951, **26**, 19-23.
12. M. Manfait, P. Lamaze, H. Lamfarraj, M. Pluot and G. Sockalingum, *Proc. SPIE: Biomedical Spectroscopy: Vibrational Spectroscopy and Other Novel Techniques*, 2000, **3918**, 135-143.
13. M. Tsuboi, K. Matsuo, T. Shimanouchi and Y. Kyogoku, *Spectrochim. Acta*, 1963, **19**, 1617-1618.
14. A. Mahadevan-Jansen and R. Richards-Kortum, *J Biomed Opt*, 1996, **1**, 31-70.
15. T. Miura and G. Thomas, Jr., *Raman spectroscopy of proteins and their assemblies*, Plenum Press, New York, 1995.
16. R. Manoharan, Y. Wang, R. Dasari, S. Singer, R. Rava and M. Feld, *Lasers Life Sci.*, 1995, **6**, 217-227.
17. M. Gniadecka, H. C. Wulf, O. F. Nielsen, D. H. Christensen and J. Hercogova, *Photochemistry and photobiology*, 1997, **66**, 418-423.
18. P. J. Caspers, G. W. Lucassen, R. Wolthuis, H. A. Bruining and G. J. Puppels, *Biospectroscopy*, 1998, **4**, S31-39.
19. G. J. Puppels, *Confocal Raman Micro-spectroscopy*, 2nd edn., Academic Press, San Diego, CA, 1999.
20. R. Alfano, C. Liu, W. Sha, H. Zhu, D. Akins, J. Cleary, R. Prudente and E. Cellmer, *Lasers Life Sci.*, 1991, **4**, 23-28.
21. S. Gordon, *Nat Rev Immunol*, 2003, **3**, 23-35.
22. L. Haversen, K. N. Danielsson, L. Fogelstrand and O. Wiklund, *Atherosclerosis*, 2008.
23. B. R. Wood, B. Tait and D. McNaughton, *Appl Spectrosc*, 2000, **53**, 353-359.
24. Y. Yazdi, N. Ramanujam, R. Lotan, M. Mitchell, W. Hittelman and R. Richards-Kortum, *Appl Spectrosc*, 1999, **53**, 82-85.
25. C. Krafft, T. Knetschke, A. Siegner, R. H. W. Funk and R. Salzer, *Vib. Spec.*, 2003, **32**, 75-83.
26. K. Hartman, N. Clayton and G. Thomas, Jr., *Biochem. Biophys. Res. Comm.*, 1973, **50**, 942-949.
27. D. C. Morrison and L. F. Kline, *J Immunol*, 1977, **118**, 362-368.
28. S. H. Zuckerman and S. D. Douglas, *Annu Rev Microbiol*, 1979, **33**, 267-307.
29. P. J. Edelson and Z. A. Cohn, *The Journal of experimental medicine*, 1976, **144**, 1581-1595.

Chapter 6

FT-IR Mapping of Keratinocyte Organizational Profiles During *in vitro* Wound Healing

6.1 Introduction

Cell migration and organization are fundamental organism development processes. As with many cell processes, cell migration involves a combination of localized cell-cell and cell-substrate cues mediated by diffusible signaling. While epidermal wound healing has been extensively studied, the localized and transient nature of cell migration makes elucidating precise cell-cell mechanisms and the transport of intra-cellular components during migration particularly difficult[1,2]. Moreover, keratinocyte organizational profiles during epidermal re-epithelialization and underlying mechanisms enabling proximal cell recruitment to sustain mass migration are not well defined.

Understanding cell interactions via direct contact and diffusible factors and their resulting effects on cell migration and organizational profiles during re-epithelialization can provide insight into these caveats. Imaging of fixed samples has been very useful in measuring cell movement and changes in cell phenotypes, particularly through increasingly widespread techniques like fluorescence resonance energy transfer and fluorescence recovery after photobleaching with confocal and total internal reflection microscopy[3-7]. By genetic cell labeling, specific intra-cellular components have been visualized in a contextual setting, whilst protein labeling has been able to monitor cytoskeletal component turnover and post-translational mechanisms[8,9]. Fluorescent labeling of signaling components that direct cytoskeletal formations are also commonly used, as with phosphoinisitol-3 kinase labeling, and have been employed to track both conformational changes in components and changes in distribution[10]. However, these techniques implement invasive, costly and time-consuming methods, often rendering the samples useless for additional downstream analysis.

FT-IR spectroscopic mapping has been able to avoid some of these setbacks by non-invasive fixed *in vitro* sample scanning[11]. Specifically for use with larger sample regions, FT-IR spectroscopy has been advantageous with its higher-throughput capabilities compared with its spectroscopic counterparts like micro-Raman. Label-free, non-invasive FT-IR mapping can also rapidly acquire chemical information pertinent to sample composition with a resolution approaching the single cell level and aiding in closing the gap between soluble factor cues and resulting spatial cell patterns. This data is in the form of a spectrum correlated to a spatial location, which when combined, produces a chemical map. Resulting chemical maps provide spatio-temporal insight into the distribution of sample components, as shown in widespread tissue diagnostic studies[12-15]. Univariate data analysis techniques can be applied to the collected hyperspectral data sets to generate chemical maps, based on integrating regions

of interest including 1700-1600 cm^{-1} for protein and 3250-2800 cm^{-1} for total lipid content. Alternatively, multivariate methods such as Unsupervised Hierarchical Cluster Analysis (UHCA) based on spectral distance calculations and clustering using algorithms including Ward's[16] enable classification based on spectral variance and can be used to generate dendograms and false colour maps.

Although FT-IR mapping alone can provide a significant amount of information related to cells and their activities, the simultaneous assessment of cell interactions by means of diffusible factors is not incorporated. In turn, FT-IR mapping only provides a subset of the overall story of re-epithelialization. To gain better insight into cell migration, organization and associated cell-interactions, gene expression analysis of the transcriptome was combined. By incorporating RT-qPCR, transcript expression profiles could be quantified. By pairing RT-qPCR with FT-IR mapping, a complete view of cells, their activities and their inter-communication profiles could be obtained.

Through the use of FT-IR mapping, this study sought to monitor the organization and associated interactions of keratinocyte-subtypes in response to *in vitro* stimulated wounding. Associated cell-cell interactions were quantified using RT-qPCR and correlated to resulting spectra for a comprehensive view of related biophysical processes occurring during re-epithelialization. Combined, a non-invasive and quantitative perspective of cell polarization, migration and organization was obtained.

6.2 Methods

6.2.1 Cell Culture. HaCaT cells were cultured in DMEM (PAA, Germany), supplemented with 1% NEAA (Invitrogen), 10% FCS (Invitrogen), 1000 units/ml P/S (Invitrogen) at 37 ºC with 5% CO_2 in air. Upon confluency, HaCaT cells were trypsinized with 0.25% Trypsin + ETDA (Invitrogen) and inactivated with a 1:4 dilution of media. Cells were pelleted for use by centrifugation at 400g for 5 minutes.

6.2.2 Time-Lapse Video. A sterile bi-well silicone culture insert (IBIDI, Germany) was adhered to a trans-reflection low'e' slide (Kevley, USA). Cell suspension at a concentration of approximately 1 x 10^6 cells per ml of DMEM was added to each well in a final volume of 80 μL. Cells were cultured until confluent within each well and inserts were subsequently ripped out, injuring boarder cells and providing a reproducible 400 μm denuded region. Following insert removal, a time-lapse video was

carried out to monitor cell migration using a Cell^M imaging station (Olympus, Germany) with a 20× objective. One image was collected every 30 minutes over a period of 4 days. All images were compiled using Cell^M software (Olympus, Germany) and time points of interest were determined (Figure 6.1).

0 Hours

4 Hours

12 Hours

36 Hours
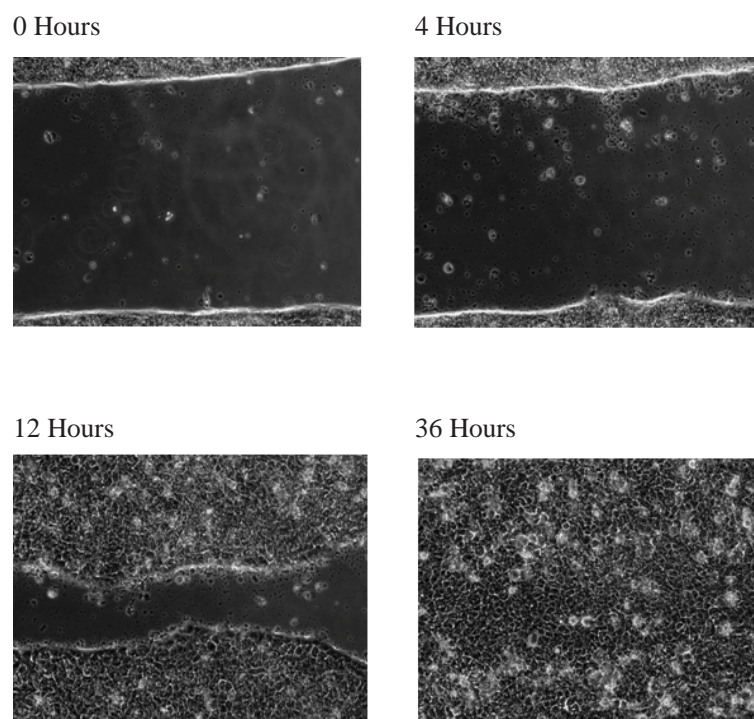
Figure 6.1 Still images collected from time-lapse video. Time points for further analysis were selected from their respective distinguishing features.

6.2.3 Simulated Wounding Sample Preparation. Samples were prepared as described above. Following swift insert removal, wounded samples were cultured in DMEM until each pre-determined time-point (0, 4, 8, 12, 24 and 36 hours). Time 0 reflects sample fixation immediately following insert removal. At each time-point, samples were washed with sterile PBS and fixed with 2% Formaldehyde in PBS for 1 hour. Samples were then wrapped in foil and stored at -80 °C until FT-IR mapping.

6.2.4 FT-IR Mapping. A Perkin-Elmer 2000 (Shelton, CT, USA) with an MCT detector was used to map each stimulated-wound sample in reflection mode. A 30 μm lateral resolution was used, providing a resolution level at or below that of single cells since migrating keratinocytes change shape strikingly with that of stationary cells, spanning sizes from 30- 80 μm, as previously observed[17]. The mapped region on each sample was 480 μm x 320 μm. For each spectrum 128 scans were co-added with an 8

cm^{-1} spectral resolution and a 15 μm step size. A background spectrum (128 co-added scans) was re-scanned after 5 sample spectra were recorded.

6.2.5 Spectral Data Analysis. FT-IR spectral maps were processed using UHCA in CytoSpec™. FT-IR maps were imported and spectra were converted into absorbance spectra. Data sets were pretreated using a quality test for amide I (1700-1600 cm^{-1}) intensity and vector normalized from 1800-900 cm^{-1} for sample thickness. A 2nd derivative applying 9 points was used for all spectra prior to UHCA. For UHCA, D-Values were used for the calculation of the distance matrix and Ward's algorithm was implemented for hierarchical clustering of the spectral ranges from 1800-900 cm^{-1} & 3250-2800 cm^{-1}, from 1300-950 cm^{-1} and from 1700-1500 cm^{-1}.

6.2.6 Gene Expression Quantification.

6.2.6.1 RNA Extraction. RNA was extracted at all time-points from the entire sample following the manufacturer's protocol supplied in the innuPREP RNA Mini-Kit (Analytik Jena, Germany). Briefly, cells were lysed and vortexed for sample homogenization. Samples were centrifuged at 8,000 g for 30 seconds to remove genomic DNA and the flow-through was combined with 70% ethanol. Samples were transferred to spin columns to bind total RNA during centrifugation at 8,000 g for 15 seconds. All total RNA bound to the spin-filter was cleaned of residual ethanol by further centrifugation at 8,000 g for 15 seconds. Samples were then washed in 80% ethanol, centrifuged at 8,000 g for 2 minutes and dried by centrifugation at 25,000 g for 5 minutes. Total RNA was then eluted into RNase-free water by centrifugation at 25,000 g for 1 minute. In total, three separate batches were collected for each time-point.

RNA quality was assessed by automated gel electrophoresis (Bio-Rad, Germany) with RNA StdSens chips. Briefly, on an accompanying chip 1 μl of each RNA sample was allocated into individual wells that had been primed with a loading gel. Following sample allocation, a fluorescent dye was added that binds to the RNA to determine the concentration and integrity. An RNA ladder was loaded to provide a comparison for sample separation and subunit weight. As a standard, the 18S subunit is used as an indicator of RNA concentration and quality for the detection of the ribosomal RNA bands (see Appendix A for results).

RNA quality was also confirmed using a NanoDrop$^®$ ND – 1000 UV/Visible Spectrophotometer for the absorbance ratio of 260 nm and 280 nm (A260/A280), with 1.8-2.0 being regarded as pure RNA (NanoDrop Technologies Ltd, USA) and for the absorbance ratio of 260 nm and 230 nm (A260/A230), with up to 2.2 being regarded as clean RNA.

6.2.6.2 cDNA Synthesis. Reverse transcription was performed using Superscript III reverse transcriptase (Invitrogen, Dorset, UK) as specified by the manufacturer. 200 ng of total RNA was combined with 0.5 μg oligo-dT$_{12-18}$ (Invitrogen) and 10 mM dNTP mix (Invitrogen), incubated for 5 minutes at 65 °C and then chilled on ice. Samples were then combined with 4 μl 5 × first strand buffer (containing 250 mM Tris-HCI (pH 8.3), 375 mM KC1, 15 mM MgCl$_2$), 1 μl of 0.1 M DTT, 40 units of RNAse (Promega) and 200 units of Superscript III reverse transcriptase (Invitrogen). Once combined, samples were incubated for 60 minutes at 50 °C. Enzymatic activity of reverse transcriptase was ceased by sample incubation at 70 °C for 15 minutes. Samples were stored at -20 °C until subsequent use.

6.2.6.3 RT-qPCR. Candidate genes were selected from previous microarray screening (see Appendix A) and from relevant literature. Reference genes specific to the cell line were previously determined by identifying the 2 most stable genes from a selection suggested by Vandesompele *et al.*[18] (see Appendix A).

All RNA transcript sequences were acquired online from the National Centre for Biotechnology Information (USA). Transcripts were cross-referenced with corresponding Ensemble Human Genome Database sequences. Homologous regions were then used for primer and probe assay design using the Universal Probe Library Assay Design Centre (Roche Diagnostics Ltd., UK). Subsequent BLAST searches were performed for all sequences to confirm primer-gene specificity. Primers were synthesized by Metabion GmBH (Germany) and probes were synthesized by Roche Diagnostics (UK), implementing the locked nucleic acid technology and incorporated the reporter dye fluorescein (FAM (6-carboxy fluorescene)) at the 5'-end and the dark quencher dye at the 3'-end (Table 6.1).

Table 6.1 Primer and probe assay designs for RT-qPCR use.

NAME	FORWARD	REVERSE	PROBE	PROBE SEQUENCE	ACCESSION NUMBER
TNFa	cagcctcttctccttcctgat	gccagagggctgattagaga	29	cttctgcc	NM_000594.2
KRT16	atcgaggacctgaggaacaa	gggccagttcatgctcatac	49	ggccacca	NM_005557.3
IL-1B	tctggtccatatgaactgaaagc	aaggacatggagaacaccactt	10	ccacctcc	NM_000576.2
ITGA2	tcaggcacaccaaagaattg	cgtctttcaaccagcaggtaa	38	ctgcttcc	NM_002203.3
ITGA3	gaggacatgtggcttggagt	gtagcggtgggcacagac	13	aggcagag	NM_002204.2
TGF-β	agcagcacgtggagctgt	cagccggttgctgaggta	72	ttcctggc	NM_000660.3
NF-kB	accctgaccttgcctatttg	agctcttttcccgatctcc	39	aggtggag	NM_003998.2
IL-6	caggagcccagctatgaact	agcaggcaacaccaggag	7	cttctccc	NM_000600.2
TIMP	gggcttcaccaagacctaca	tgcaggggatggataaacag	76	tggctgtg	NM_003254.2
MMP9	gaaccaatctcaccgacagg	gccacccgagtgtaaccata	6	cagaggaa	NM_004994.2

Every RT-qPCR assay was performed in triplicate using the 384 well configuration and an ABI® 7900 (Applied Biosciences, Germany). Each assay included three no-template controls. The reaction volume for each well was 10 μl and contained 5 μl 2x Precision Master Mix (Primer Design, UK). Additionally, 0.7 μl of RNase-free H_2O (Ambion, Inc.), 0.1 μl of 20 μM forward primer, 0.1 μl of 20 μM reverse primer, 0.1 μl of 10 μM Roche fluorescently-labeled probe and 4 μl of sample cDNA at 2.5 ng/ μl were added to each well. All no-template control wells supplemented cDNA volume with 4 μl of RNase-free H_2O. The amplification conditions for all assays included 1 cycle at 65 °C for 5 minutes, 40 cycles of 95 °C for 2 minutes, 95 °C for 15 seconds and 60 °C for 1 minute. RT-qPCR data was analyzed by using ABI® 7900 standard software to determine cycle threshold (Ct) values and relatively quantified to the Time 0 gene expression profiles to view changes during re-epithelialization. Reference genes YWHAZ (Tyrosine 3-monooxygenase/tryptophan 5-monooxygenase activation protein) and HMBS (hydroxymethylbilane synthase) were selected for their stability in the HaCaT cell line, identified as previously described[18], and were applied to all assays as an endogenous control.

6.2.7 Statistical Analysis. RT-qPCR data was assessed for statistical significance using $2^{\Delta\Delta Ct}$ values for each candidate gene. Transformed values for each gene were imported into GraphPad Prism v.3.0 (La Jolla, CA USA) assessed for significance using the Kruskal-Wallis nonparametric test with a Dunn's post-test. P-values below 0.1 (90% confidence interval) are considered to be significant.

6.3 Results & Discussion

Keratinocytes become activated following trauma, directly begin producing inflammatory mediators and polarize for migration. Label-free FT-IR mapping at multiple pre-selected stages during stimulated re-epithelialization indicated that multiple keratinocyte subtypes were present, in agreement with previous observational studies[19]. Keratinocyte organizational profiles were found to vary significantly with each time-point and possess function-specific groupings. Transcript profiles at each time-point were also found to be consistent with *in vivo* literature, providing a trustworthy model, and allowing for further probing of the resulting spectra.

6.3.1 Time 0

Directly following insert removal, the Time 0 sample displayed moderate absorbance fluctuations in the integrated area of the amide I (1680-1620 cm^{-1}) chemical map (Figure 6.2) and minimal absorbance fluctuations attributed to regions of cell proliferation for lipid (3250-2800 cm^{-1}) (Figure 6.3), indicating that the sample remains largely homogeneous (Figure 6.2). However, following UHCA on data set from 1800-900 cm^{-1} & 3250-2800 cm^{-1}, distinct clusters could be observed. Resulting clusters displayed regions of dispersion directly on the edge, indicated by the light blue and green clusters. Remaining clusters shown in grey, blue and red illustrate the extrapolation of differing cell phenotypes from their natural monolayer colony formation[20].
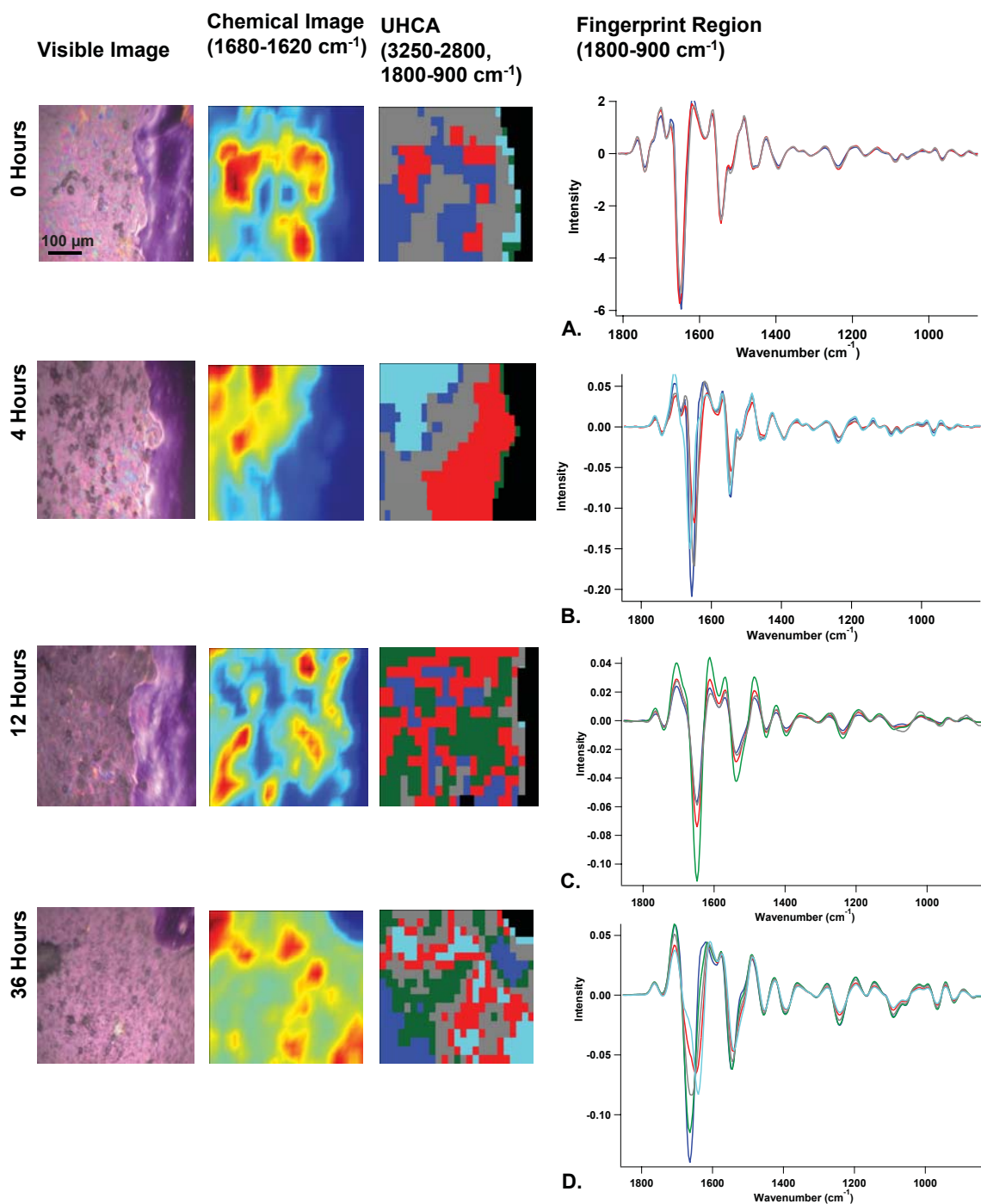
Figure 6.2 FT-IR imaged time points and their subsequent UHCA. Spectral plots (right) correspond with the respective UHCA images (left). Visible images display marginal changes in keratinocyte activity, aside from overall cell migration and density. By looking at corresponding chemical images specific for amide I, distinct regions of high protein content can be identified providing insight into overall keratinocyte organizational patterns. The final stage of analysis, UHCA clustering, displays substantial variations between each time point and can be correlated with differing cell phenotypes during re-epithelialization. Organizational preferences of keratinocytes during varying migration times can be seen and spectral comparisons between regions display the variations between keratinocyte phenotypes in the migrating monolayer.
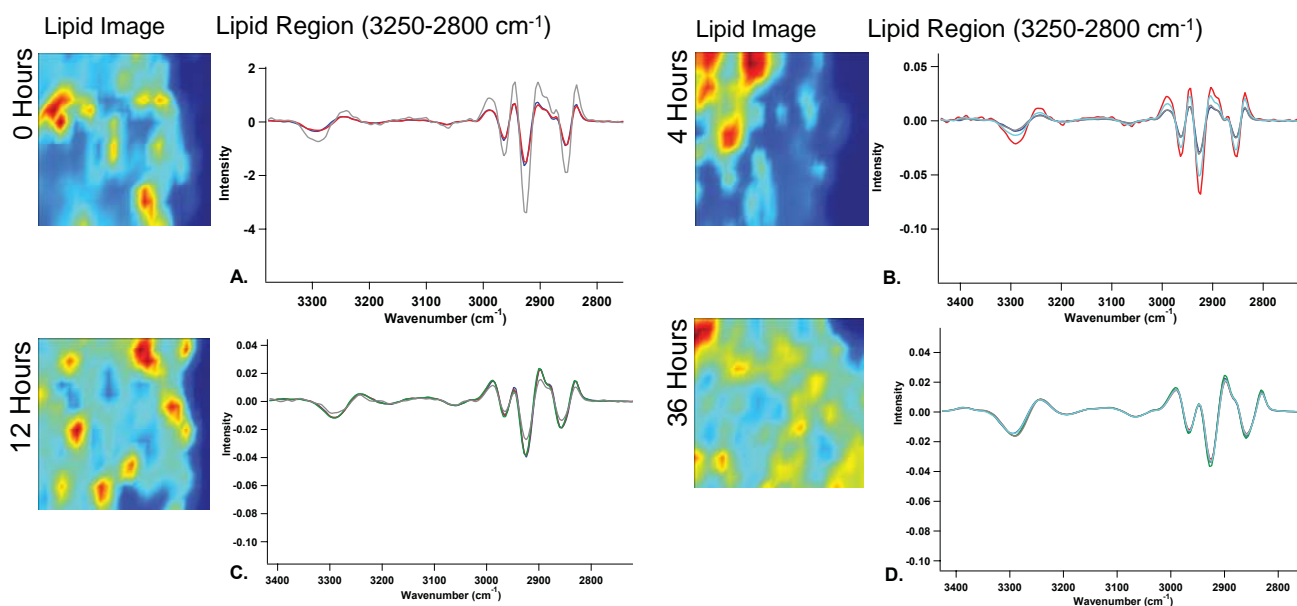
Figure 6.3 Lipid distributions at each time point. Chemical images display lipid organization, with clusters of high lipid regions identified at 0 hours. These clusters are characteristic of normal keratinocyte behavior and are zones of cell proliferation. Following 4 hours of incubation post-stimulated wounding, lipid presence is found to have shifted to one region, with remaining keratinocytes displaying low cytoskeletal modifications and hence, proliferative activity. By 12 hours, proliferative regions are found to return and spread to overall increased lipid presence, as shown by the chemical image at 36 hours. Spectral graphs illustrate the differences in the lipid profiles from UHCA for each time point, as displayed in Figure 6.2.

When comparing the average spectra from each cluster following UHCA over 1300-950 cm^{-1}, negligible differences were detected in the DNA and RNA. These minor fluctuations were identifiable at 1240 cm^{-1}, 1084 cm^{-1}, 996 cm^{-1} and 964 cm^{-1}; all attributed to symmetric and anti-symmetric DNA and RNA motions[21]. An additional variation was noticed at 1168 cm^{-1}, assigned to lipid CO-O-C symmetric and anti-symmetric vibrations[21]. These slight discrepancies are likely the result of cells in various cell cycle stages, particularly from the onset of enhanced mitosis rates[22]. Further discrepancies were detected at 1668 cm^{-1}, 1650 cm^{-1}, 1640 cm^{-1} and at 1612 cm^{-1}, all corresponding to amide I for protein content and alongside an additional feature at 1684 cm^{-1}. All combined, these variances possess the spectral attributes to that of the provisional matrix protein fibronectin (FN)[23]. FN is an extracellular-matrix (ECM) protein that provides a scaffold to direct migrating cells[24]. Epidermal keratinocytes are known to not produce FN during regular culturing and only when stimulated to begin migratory activity[25, 26], indicating cells have begun phenotype changes in response to wounding.

Corresponding FN spectral assignments were also found to vary between clusters, depicting where cells were polarizing for subsequent migration. When absorbance spectra were compared with commercially available FN in phosphate buffered saline, spectral features were found to be similar aside from a slight spectral shift (Figure 6.4). This shift was approximately ten wavenumber values and resulted from the combined influences of both temperature and origin of FN synthesis. Plasma FN was studied by Pauthe *et al.*[23] using FT-IR to view any structural modifications in response to temperature. Here, β-aggregations in FN were found to vary depending on the environmental temperature. Additionally, plasma FN possesses slightly different monomer polypeptides to form the protein dimer structure to the cell-surface FN synthesized by epidermal keratinocytes[27].
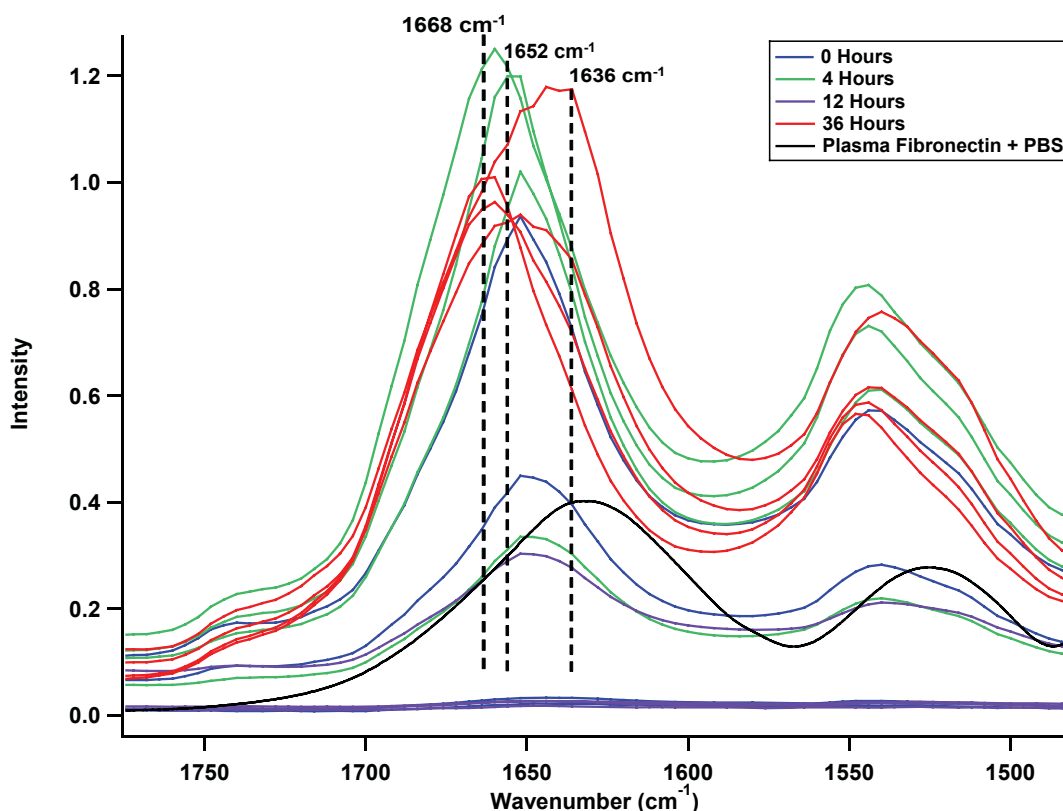
Figure 6.4 Comparison of FT-IR spectra from plasma FN in PBS with the FN features identified in time-point specific spectra. As shown, a distinct shift is noticed from the 1664- 1636 cm^{-1} region. This can be attributed to the use of plasma FN which possesses different monomers to the secreted FN from keratinocytes. Additionally, conformational changes in the structure of FN with respect to α-helices and β- pleated sheets have been found to occur at varying temperatures. As secreted FN is synthesized in culture (38 ºC) and plasma FN is kept at room temperature (approx. 22 ºC), shifts in the spectral peaks could also occur[23].

6.3.2 4 Hours

The chemical image following 4 hours post-insert removal exhibits a distinctly varied cellular organization profile (Figure 6.2). Following UHCA, a noticeable row-like pattern was detected, indicating that cells have altered their phenotype from Time 0. The thin green cluster was excluded for resulting from dispersion artifacts. Phenotypical changes occur from cell-cell communication and diffusible factor penetration into the keratinocyte sheet, activating and recruiting more cells for the orchestrated migration to repair the denuded region. With a known delay between wounding and keratinocyte migration[28], mapping at 4 hours clearly visualizes the changes in cell behavior. Corresponding spectra for each cluster displayed minor fluctuations in DNA and RNA content (Figure 6.2 D). Specifically, vibrational asymmetric stretching of PO_2^- at 1236 cm^{-1}, vibrational symmetric stretching of PO_2^- at 1088 cm^{-1} and symmetric PO_4^- stretching and deoxyribose skeletal motions at 964 cm^{-1} [21] were detected in the blue and light blue regions. These changes identify regions of proliferation following cell activation, known to occur distal to the migrating edge[29]. The noted change in edge cell phenotype also indicates that post-insert removal, edge cells become damaged, as cells require very low forces for injury[2].

Compared with Time 0, 4 hour lipid profiles have also shifted (Figure 6.5). Areas of increased lipid intensities for saturated and unsaturated fatty acids span from 3250-2800 cm^{-1} and were most prevalent furthest from edge cells. This behavior is in agreement with *in vivo* wound healing, with proliferation replenishing damaged and dead cells[30].

Change in Gene Expression Post-Stimulated Wounding
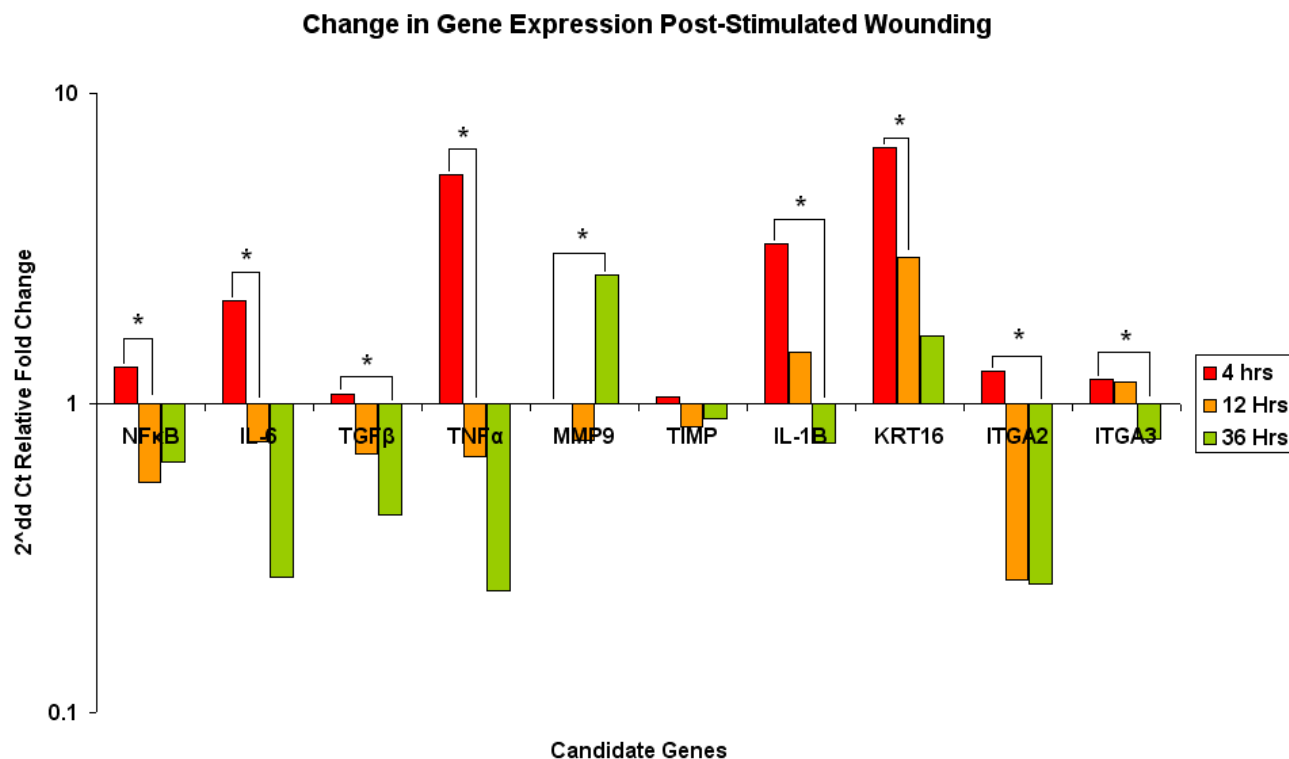
Figure 6.5 Changes in candidate gene expression following stimulated wounding. Gene expression changes in the stimulated wound environment of epidermal keratinocytes were found to mirror that of *in vitro* re-epithelialization. Specifically, the change in Keratin 16 (KRT16), Interleukin-1b (IL-1b), Tumor Necrosis Factor α (TNF-α) and Interleukin-6 (IL-6) confirm keratinocyte activation profiles, facilitating cell migration and re-epithelialization of the denuded region[31, 32]. Transcription Growth-Factor β (TGF-β) is also a potent initiator of keratinocyte migration, as illustrated by its substantial up-regulation following stimulated wounding[33]. Additionally, the up-regulation in Nuclear Factor-κB is indicative of increased signal transduction from cell-cell and cell-surface interactions. For cell migration, Matrix-Metalloproteinase's, like MMP9, and Tissue-Inhibiting Metalloproteinase (TIMP) tightly regulate the de-attachment and re-attachment process of cells on the extra-cellular matrix to cover the denuded region. Different integrin modalities, like integrin-α2 (ITGA2) and integrin-α3 (ITGA3), also enable this cell attachment during migration and are differentially expressed[34]. Changes were assessed using a Kruskall-Wallis nonparametric test followed by the Dunn's post-test, where $P \leq 0.1$.

The most significant fluctuations identified in the average spectra of each major cluster were with the amide I (α-helices at 1656 cm^{-1}) and amide II (β-pleated sheets at 1530 cm^{-1}, α-helices at 1550-40 cm^{-1}) regions[21]. Moreover, the FN features at 1676 cm^{-1} (β-pleated turns) and at 1636 cm^{-1} (β-pleated stands) display substantial variations between clusters (Figure 6.2D)[23]. Combined, these intensity variances and wavenumber shifts support changes in FN content and its structural components present. These fluctuations can distinguish between migrating cells and cells of other functions. In this specific sample, dark blue and grey regions possess elevated FN features and low DNA/RNA profiles, strongly

indicating migratory behavior, while Red and light blue regions possess low FN features but high unsaturated and saturated fatty acids (3250-2800 cm^{-1}) (Figure 6.2B) which correlates to cell membrane reorganization and subsequent proliferation[21].

Corresponding gene expression profiles exhibit an up-regulation in genes specific to keratinocyte activation, Interleukin-1b (IL-1b) and Keratin 16 (KRT16). IL-1b commonly denotes keratinocyte activation[35] and assists with propagating the activated phenotype[31,36], while KRT16 works synergistically with Tumor Necrosis Factor- α (TNF-α) to sustain the activated phenotype[37] (Figure 6.5). Associated cell activation behavior includes hyper-proliferation, differentiation, migration and increased cell communication[38]. This confirms keratinocyte response to stimulated wounding and supports associated FT-IR data.

Elevated KRT16 also correlates to polarized keratin filaments in the edge population, identifiable with cells of the green and red UHCA regions. This reorganization of intercellular structural components results in keratinocyte polarization and adhesion to the extracellular matrix (ECM) and was confirmed by elevated Integrin-α3 (ITGA3) and tissue inhibitor metalloproteinase (TIMP). Integrins are the main receptors involved in migration and ligand binding strength alterations permit the cyclic process of cell migration through a series of attaching and de-attaching processes[39]. Specifically, Integrin-α2 (ITGA2) facilitates initial cell attachment to the ECM, is replaced by ITGA3 for cell movement and is later re-expressed to halt migration[40].

A significant increase in Interleukin-6 (IL-6), Interleukin-1b (IL-1b) and TNF-α expression was also detected, propagating the activated phenotype and stimulating cell migration[41, 42]. A decline in Nuclear Factor-κ B (NFκB) was also detected and although not significant (Figure 6.5), could be attributed to the delay in keratinocyte migration onset.

6.3.3 12 Hours

Following 12 hours post-insert removal, keratinocytes have reorganized their distribution (Figure 6.2C). Organizational patterns were still function-specific, albeit with a more dispersed clustering profile. This disbursement resulted from widespread keratinocyte migration at this time-point and included sustained hyperproliferation, cell polarization and epidermal keratinocyte sheet advancement.

The light blue cluster of the resulting UHCA was omitted from comparison from the presence of dispersion artifacts. Of the remaining clusters, noted spectral differences were with amides I, II, III and DNA/RNA regions (Figure 6.2C). Variances between amide groups concur with the necessary phenotypic changes to aid directional keratinocyte migration and adhesion to the ECM. DNA/RNA fluctuations could be attributed to hyperproliferation, occurring to replenish the population of damaged cells and ensure sufficient cells for successful wound closure. Corresponding lipid profiles at 12 hours were found to increase in intensity from both previous time-points. Organization was found to be mostly homogenous, punctuated with small regions of high lipid profiles characteristic of cell proliferation zones from increased cytoskeletal rearrangements.

Associated gene expression profiles display wide-spread up-regulation in all candidate genes (Figure 6.5). ITGA3 remains up-regulated, as does KRT16 and IL-1b. The decline in ITGA2 expression was mirrored by an increase in ITGA3 from the concomitant response of cells attaching to the ECM via ITGA2 and then becoming fully motile through lamellipodia extension and adhesion to the ECM via ITGA3[43].

6.3.4 36 Hours

At 36 hours, keratinocyte organization begins exhibiting indications of cells returning to un-activated phenotypes. At this time-point, the opposing keratinocyte sheets have joined, filling the denuded region and halting migration following 'contact-inhibition', as displayed in Figure 6.2. The process of 'contact-inhibition' may stop cell migration but the process of cell maturation continues, with cells on the suture region continuing to display activated phenotypes. The chemical image for the lipid region indicates a mostly homogeneous lipid presence, with minor elevated lipid cluster's occurring furthest from the cell-suture region (Figure 6.3). This time-point also displays considerable fluctuations in DNA and RNA components (Figure 6.2D). Particularly in the dark blue region, elevated 1244 cm^{-1} and 1028 cm^{-1} bands were noticed when compared with other cluster regions. Combined, these profiles indicate where cells are still dividing to finish the re-epithelialization process. Meanwhile, cells furthest from the suture region begin reverting to the phenotype distribution noticed at 0 hours. Further confirming this, the dark blue region displayed no FN feature at 1684 cm^{-1}, indicative that cells particularly in the dark blue cluster are returning to an inactivated phenotype and no longer need to produce ECM proteins.

The green cluster possessed similar spectral features, although these cells also displayed elevated lipid profiles, indicating that cytoplasmic rearrangements are still occurring for cell proliferation. Therefore, cells in the green region are proliferating to sustain the final migration of edge cells.

Remaining clusters in light blue, grey and red all displayed similar spectral features to the dark blue and green regions. These clusters possess shifts in their amide I and II bands, which are likely to result from α-helical and β-pleated sheet degradation from matrix metalloproteinase's (MMP's) in contact with any remaining FN. Corresponding RT-qPCR data displays an up-regulation in both MMP9 and TIMP, confirming protease activity (Figure 6.5). MMP9 is necessary for the detachment of wound edge keratinocytes from the ECM, allowing migration by degrading mature ECM components[44,45]. Additionally, an overall decline in IL-1b expression is present, in agreement with the decline in FT-IR detected activated keratinocytes and FN present. TGF-β is known to possesses a concentration-dependent control over MMP9 expression[46] and was down-regulated in this sample, enabling complete re-epithelialization through MMP-driven matrix degradation for future remodeling. Moreover, a decline in ITGA2 and ITGA3 was detected, indicating an inhibition in keratinocyte proliferation[47].

6.4 Conclusion

By combining label-free FT-IR mapping & chemometric analysis methods, the organizational profiles of single cells & populations during stimulated healing have been illustrated. With a resolution level around a single cell, phenotypic differences between cells and their neighbors have also been distinguished and visualized through the use of UHCA. Collectively, spectral data also strongly indicate that lipid levels correlate with proliferative regions. Moreover, by combining quantitative transcriptome analysis with FT-IR mapping, associated cell-interactions in the wound environment could be quantified, leading the focus from cell behavior to a systemic view of re-epithelialization.

Moreover, FT-IR mapping and RT-qPCR have clearly displayed their strengths as combined techniques for *in vitro* cell studies. These united techniques can assist in identifying contact inhibition cues as well as cell migration initiation and proliferation cues, including the increasingly important contribution of cell lipids. This capability will be applied toward further studies of fundamental cell-cell mechanisms enforced during epidermal re-epithelialization.

References

1. M. Digmana, P. Wisemanb, C. Choic, A. Horwitzc and E. Grattona, *PNAS*, 2009, **106**, 2170-2175.
2. P. Girard, E. Cavalcanti-Adam, R. Kemkemer and J. Spatz, *Soft Matter*, 2007, **3**, 307-326.
3. M. E. Huot, C. M. Brown, N. Lamarche-Vane and S. Richard, *Mol Cell Biol*, 2009, **29**, 1933-1943.
4. J. Morgan, R. Huckfeldt and R. O. Wong, *Exp Eye Res*, 2005, **80**, 297-306.
5. Y. Sako and T. Uyemura, *Cell Struct Funct*, 2002, **27**, 357-365.
6. L. Soon, F. Braet and J. Condeelis, *Microsc Res Tech*, 2007, **70**, 252-257.
7. M. Parsons, B. Vojnovic and S. Ameer-Beg, *Biochem Soc Trans*, 2004, **32**, 431-433.
8. B. N. Giepmans, S. R. Adams, M. H. Ellisman and R. Y. Tsien, *Science*, 2006, **312**, 217-224.
9. D. M. Chudakov, S. Lukyanov and K. A. Lukyanov, *Trends in Biotechnology*, 2005, **23**, 605-613.
10. A. J. Ridley, M. A. Schwartz, K. Burridge, R. A. Firtel, M. H. Ginsberg, G. Borisy, J. T. Parsons and A. R. Horwitz, *Science*, 2003, **302**, 1704-1709.
11. M. Mariani, P. Lampen, L. Maccoux, B. Wood and V. Deckert, *PNAS*, 2009, **submitted**.
12. P. Lasch, W. Haensch, D. Naumann and M. Diem, *Biochim Biophys Acta*, 2004, **1688**, 176-186.
13. B. R. Wood, L. Chiriboga, H. Yee, M. A. Quinn, D. McNaughton and M. Diem, *Gynecologic oncology*, 2004, **93**, 59-68.
14. M. Diem, L. Chiriboga, P. Lasch and A. Pacifico, *Biopolymers*, 2002, **67**, 349-353.
15. M. Diem, M. Romeo, S. Boydston-White, M. Miljkovic and C. Matthaus, *The Analyst*, 2004, **129**, 880-885.
16. J. Ward, *J Am. Stats. Ass.*, 1963, **58**, 236-244.
17. E. O'Toole, *Clin. Exp. Derm*, 2008, **26**, 525-530.
18. J. Vandesompele, K. De Preter, F. Pattyn, B. Poppe, N. Van Roy, A. De Paepe and F. Speleman, *Genome Biol*, 2002, **3**, RESEARCH0034.
19. G. K. Patel, C. H. Wilson, K. G. Harding, A. Y. Finlay and P. E. Bowden, *J Invest Dermatol*, 2006, **126**, 497-502.
20. D. Tudor, F. Chaudry, L. Harper and I. C. Mackenzie, *Cell Prolif*, 2007, **40**, 706-720.
21. A. D. Meade, F. M. Lyng, P. Knief and H. J. Byrne, *Anal Bioanal Chem*, 2007, **387**, 1717-1728.
22. M. Goto, H. Sumiyoshi, T. Sakai, R. Fassler, S. Ohashi, E. Adachi, H. Yoshioka and S. Fujiwara, *Mol Cell Biol*, 2006, **26**, 548-558.
23. E. Pauthe, J. Pelta, S. Patel, D. Lairez and F. Goubard, *Biochim Biophys Acta*, 2002, **1597**, 12-21.
24. R. A. Clark, J. M. Lanigan, P. DellaPelle, E. Manseau, H. F. Dvorak and R. B. Colvin, *J Invest Dermatol*, 1982, **79**, 264-269.
25. F. Grinnell, K. Toda and A. Takashima, *Journal of Cell Science*, 1987, **8**, 199-209.
26. K. Toda and F. Grinnell, *J Invest Dermatol*, 1987, **88**, 412-417.
27. H. Brotchie and D. Wakefield, *The Australasian Journal of Dermatology*, 1990, **31**, 47-56.
28. R. Rovee and H. Maibach, *The Epidermis in Wound Healing*, Informa Health Care, 2004.
29. P. Martin, *Science*, 1997, **276**, 75-81.
30. A. Jacinto, A. Martinez-Arias and P. Martin, *Nature Cell Biology*, 2001, **3**, E117-123.
31. I. Freedberg, M. Tomic-Canic, M. Komine and M. Blumenberg, *J Invest Derm*, 2001, **116**, 633-640.
32. S. Yano, T. Banno, R. Walsh and M. Blumenberg, *J. Cell Phys.*, 2008, **214**, 1-13.

33. C. L. Phillips, S. B. Combs and S. R. Pinnell, *J Invest Dermatol*, 1994, **103**, 228-232.
34. P. C. Marchisio, S. Bondanza, O. Cremona, R. Cancedda and M. De Luca, *J Cell Biol*, 1991, **112**, 761-773.
35. T. S. Kupper and R. W. Groves, *J Invest Dermatol*, 1995, **105**, 62S-66S.
36. R. Paladini, K. Takahashi, N. Bravo and P. Coulombe, *J Cell Biol*, 1996, **132**, 381-397.
37. B. J. Nickoloff and L. A. Turka, *The American Journal of Pathology*, 1993, **143**, 325-331.
38. I. M. Freedberg, M. Tomic-Canic, M. Komine and M. Blumenberg, *J Invest Dermatol*, 2001, **116**, 633-640.
39. F. Decline and P. Rousselle, *J Cell Sci*, 2001, **114**, 811-823.
40. W. G. Carter, E. A. Wayner, T. S. Bouchard and P. Kaur, *J Cell Biol*, 1990, **110**, 1387-1404.
41. R. Gallucci, D. Sloan, J. Heck, A. Murray and S. O'Dell, *J Invest Derm*, 2004, **122**.
42. B. Lu, P. Elias and K. Feingold, *The role of primary cytokines, TNF, IL-1 and IL-6, in permeability barrier homeostasis.*, CRC Press, 2006.
43. H. Larjava, T. Salo, K. Haapasalmi, R. H. Kramer and J. Heino, *The Journal of Clinical Investigation*, 1993, **92**, 1425-1435.
44. T. Salo, M. Makela, M. Kylmaniemi, H. Autio-Harmainen and H. Larjava, *Laboratory Investigation; A Journal of Technical Methods & Pathology*, 1994, **70**, 176-182.
45. U. Mirastschijski, U. Impola, T. Jahkola, T. Karlsmark, A. G. MS and U. Saarialho-Kere, *Human Pathology*, 2002, **33**, 355-364.
46. J. M. Lamar, V. Iyer and C. M. DiPersio, *J Invest Dermatol*, 2008, **128**, 575-586.
47. F. E. Turner, S. Broad, F. L. Khanim, A. Jeanes, S. Talma, S. Hughes, C. Tselepis and N. A. Hotchin, *J Biol Chem*, 2006, **281**, 21321-21331.

Chapter 7

High Resolution Imaging & Gene Expression Profiling of ECM Localization & Lipid Profiles in Epidermal Keratinocyte During *in vitro* Wound Healing

7.1 Introduction

Following the initial FT-IR mapping on scratch assays, organizational patterns based on cell phenotype were found to vary dramatically during re-epithelialization. Although this work touched upon protein and lipid-related spectral contributions, higher resolution imaging over a larger area was determine to be necessary for further insight to be gained into the resulting spectral and phenotypical fluctuations.

Using higher resolution FT-IR mapping (6.25 μm vs. 30 μm previously), this study sought to monitor protein and lipid spectral profiles of keratinocyte functional organization profiles in response to *in vitro* stimulated wounding. Resulting spectra were correlated to RT-qPCR transcript expression profiles for a comprehensive view of biophysical alterations during re-epithelialization, providing a non-invasive and quantitative inspection of cell polarization and organization. Resulting cluster images were correlated with conventional staining techniques, including histological lipid staining (Oil Red O) and immunofluorescence.

7.2 Methods

All methods, unless otherwise stated below, were previously described on pages 67-71.

Table 7.1 Primer and probe assay designs for RT-qPCR use.

NAME	FORWARD	REVERSE	PROBE	PROBE SEQUENCE	ACCESSION NUMBER
ITGA2	tcaggcacaccaaagaattg	cgtctttcaaccagcaggtaa	38	ctgcttcc	NM_002203.3
ITGA3	gaggacatgtggcttggagt	gtagcggtgggcacagac	13	aggcagag	NM_002204.2
KRT13	tcaccatgcagaacctcaac	aggtgccagtcacggatct	85	gacctgga	NM_153490.2
KRT16	atcgaggacctgaggaacaa	gggccagttcatgctcatac	49	ggccacca	NM_005557.3
IL-8	agacagcagagcacacaagc	atggttccttccggtggt	72	ttcctggc	NM_000584.2
PPAR β/δ	ccccaggagcagaagagagt	ctaagcctgcaggtgcaat	43	ctgcccca	NM_006238.3
EGF	gggtcaatgcaaccaacttc	ctctgtgcccattccacata	16	ggaggcag	NM_001963.3

7.2.1 FT-IR Mapping. A Perkin-Elmer Spotlight 400 (Shelton, CT, USA) incorporating an MCT detector was used to map each stimulated-wound sample in reflection mode. A 6.25 μm lateral resolution was used, providing a resolution level below that of single cells. The mapped region on each sample was 1 mm^2. For each spectrum, 120 scans were

co-added with a 4 cm^{-1} spectral resolution and a background spectrum (960 co-added scans) was pre-scanned before sample mapping.

7.2.2 Spectral Data Analysis. FT-IR spectral maps were processed using UHCA in CytoSpec™. FTIR maps were imported and spectra were converted into absorbance spectra. Data sets were pretreated using a quality test for amide I (1700-1600 cm^{-1}) intensity and vector normalized from 1800-900 cm^{-1} for sample thickness. A 2nd derivative applying 9 points was used for all spectra prior to UHCA. For UHCA, D-Values were used for the calculation of the distance matrix and Ward's algorithm was implemented for hierarchical clustering of the spectral ranges from 1800-900 cm^{-1}& 3250-2800 cm^{-1} and from 3250-2800 cm^{-1}.

7.2.3 Immunofluorescence. Following fixation and spectroscopic analysis, Raman cell samples were fluorescently labeled for caveolin-1 and pan-Cadherin. Samples were rehydrated in PBS for 5 minutes and then blocked for 30 minutes with 1% Bovine Serum Albumin (BSA) in PBS+ Tween (PBST) to prohibit non-specific antibody binding. For visualization of caveolin lipid raft invaginations and the plasma membrane, cells were labeled with Rabbit polyclonal caveolin-1 (abcam, UK) at a concentration of 5 µg/ml and Mouse monoclonal pan-Cadherin (abcam, UK) at a concentration of 20 µg/ml for 1 hour at room temperature. Samples were washed 3 times for 5 minutes each and stained with the corresponding secondary antibodies. Goat anti-Rabbit IgG FITC conjugate (abcam, UK) and Rabbit anti-mouse IgG Texas Red conjugate (abcam, UK) were both used at a concentration of 40 µg/ml and incubated for 1 hour at room temperature. Samples were then washed 3 times for 5 minutes each PBS and the nuclei were counterstained with 14',6-diamidino-2-phenylindole (DAPI) (Sigma Aldrich, Germany) at 1:1000 dilution for 2 minutes. Samples were washed 3 times for 5 minutes each and then mounted (Sigma Aldrich, Germany).

An Olympus IX70 confocal-based microscope (Olympus, Germany) was used with appropriate bandpass filters for 350-460 nm (DAPI), 510-540 nm (FITC) and 595-600 nm (Texas Red). Images were captured using Cell^{A} software (Olympus, Germany).

7.3 Results & Discussion

From H&E staining, a monolayer of cells could be identified. However, conventional histological staining was unable to identify phenotypical differences between cells from its general binding targets (cytoplasm and nuclei) (Figure 7.1A). Once samples were mapped using FT-IR, distinct clusters of cells based on differing phenotypes were identified, in agreement with our previous study albeit on a smaller scale[1]. Regions of cell proliferation could be discerned at 0, 12, 24 and 36 Hours from their heightened features in the 1300-900 cm^{-1} region. Phenotypical changes in edge cells were visualized at all time-points and the population of migrating edge cells was found to increase in density over time (Figure 7.2A). All noticed changes in keratinocyte activities were in agreement with gene expression profiles specific for epidermal wound healing.

As histological staining was unable to discern these varied phenotypes, immunofluorescence was carried out for its more specific nature. Antibodies for the lipid-raft caveolin-1 (CAV1- FITC), the plasma membrane (pan-cadherin- Texas Red) and an intercalating dye for RNA (DAPI) were all used to visualize cell changes. From these images (Figure 7.1B), changes in nuclear granulation and size, cytoplasmic content and the distribution of the specific lipid components could be visualized, providing a degree of phenotypical information. Although targets were more specific, organizational profiles of keratinocytes could not be identified, illustrating the diverse number of components involved in phenotypical differences and surpassing what is practically attainable with conventional labeling techniques. In turn, the setbacks from conventional labeling exemplify both the sensitivity of FT-IR and the advantages of its non-invasive, multivariate nature, enabling all cellular components to be included in UHCA and subsequent false-color visualization.
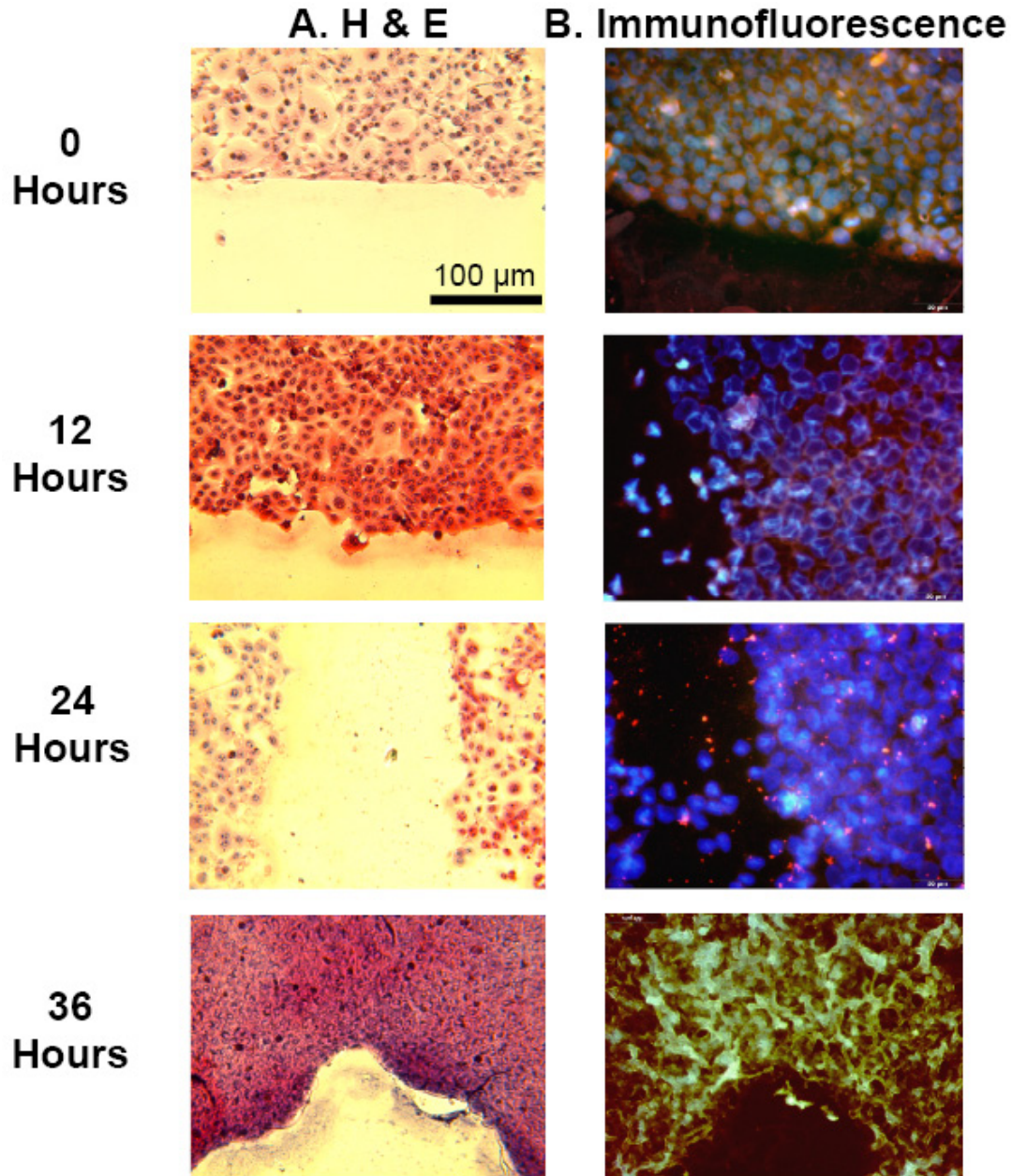
Figure 7.1 (A) Hematoxylin & Eosin (H & E) and (B) immunofluorescence staining on select time-points. Staining was carried out to visualize organizational profiles of keratinocytes monolayers during stimulated re-epithelialization. As noticed, cells can be clearly discerned following both types of staining but large-scale phenotypical differences remain unidentifiable.

7.3.1 Protein/ ECM Distribution

Upon inspection of the UHCA results, clustering for 1800-900 cm^{-1} and 3250-2800 cm^{-1} regions were able to detect changes in ECM presence (Figure 7.2).
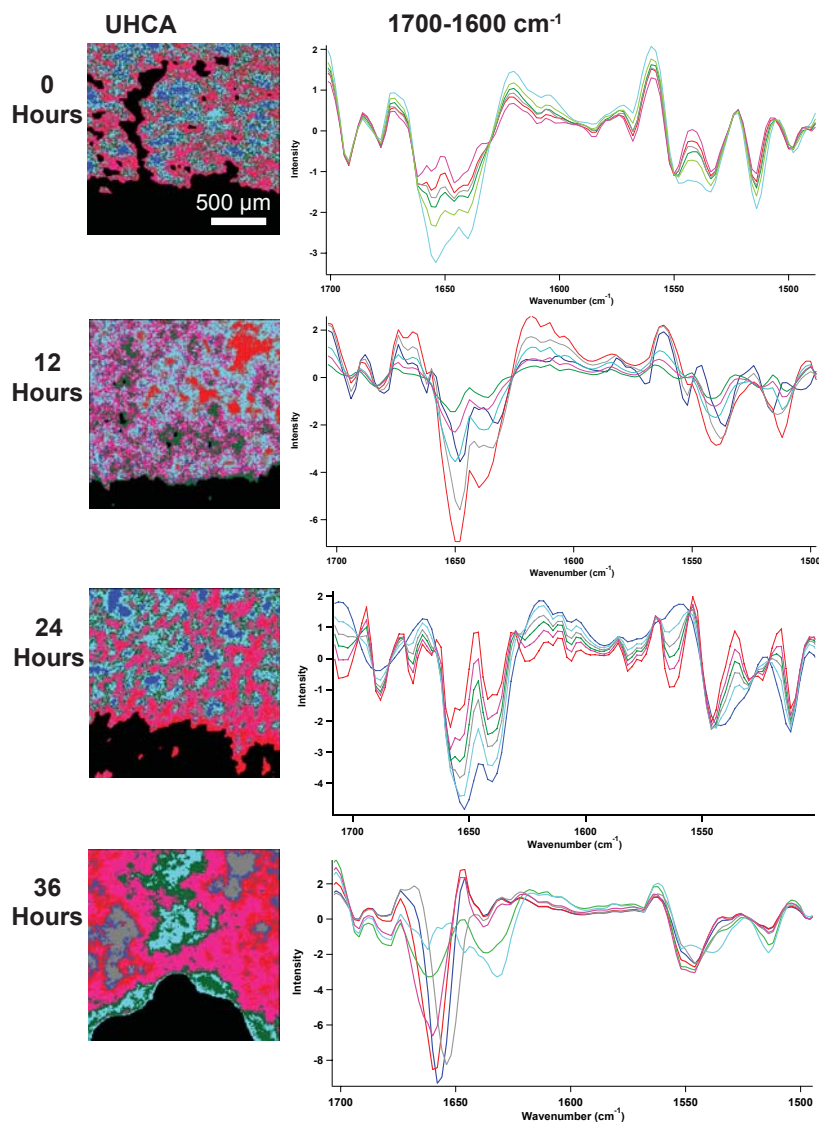
Figure 7.2 Unsupervised hierarchical cluster analysis (UHCA) of keratinocyte monolayers at select time-points during stimulated re-epithelialization for total cell content (1800-900 cm^{-1}; 3250-2800 cm^{-1}). Following UHCA analysis of each FT-IR map, varying clusters based on cell functions can be elucidated. Over time, these clusters distribute differently, with a marked increase in the number of activated, leading keratinocytes and the size of the quiescent, proliferation zones. By 36 hours, the denuded region has been covered, although cells possessing the activated phenotype still remained within the suture region, confirming that cell activity has not ceased following the joining of both migrating regions. Corresponding spectra for 1700-1500 cm^{-1} can detect differences in extracellular matrix (ECM) production. From 0 hours through 24 hours, both in-soluble fibronectin (1654-1640 cm^{-1} doublet) and laminin (1654-1640 cm^{-1} triplet and 1546-1534 cm^{-1} doublet) were detected and are instrumental in enabling cell migration. By 36 hours, laminin presence has subsided and predominately fibronectin remains. However, the cell populations in the suture region (light green; green) still possess laminin; confirming that cell movement is still occurring.

At 0 hours, laminin (1654-1640 cm^{-1} triplet and 1546-1534 cm^{-1} doublet)[2, 3], intracellular keratins (1514 cm^{-1})[2, 4] and in-soluble FN[5] (1654-1640 cm^{-1} doublet) were identified. Laminin was specifically detected among wound edge cells, while FN was localized among the trailing keratinocyte sheet and in the proliferation zones. Under normal conditions, keratinocytes are known to synthesize these ECM proteins to provide a scaffold for organization and assist with directional cell movement via integrin binding in wound healing[6-8]. Meanwhile, keratin presence facilitates cell polarization for subsequent migration and was highest among cells surrounding proliferation zones.

By 12 and 24 hours post-wounding, marked increases were detected in FN and keratin presence among both edge cell and proliferation zone populations. At 12 hours, FN presence was found to surpass that of laminin throughout the sample (Figure 7.2). FN then declined at 24 hours and was countered by laminin presence throughout the migrating cell population, while FN was found within the trailing monolayer (Figure 7.2).

As migration began ceasing at 36 hours from the denuded region bring mostly covered, laminin presence was detected to be localized among the edge cells to a comparable degree with 24 hours. FN presence continued to increase in the trailing cell monolayer, and particularly in the proliferation zones. This overall change in FN localization can be attributed to its importance in providing a provisional matrix for cell migration and subsequent use for the formation of a new basement membrane[9].

These results were further confirmed through parallel RT-qPCR analysis of select transcripts for Keratin's (13 and 16) form their importance in cell polarization, Interleukin-8 (IL-8) for its role in inducing cell migration[10, 11] and select integrins (α2 and α3) for their importance in facilitating cell migration (Figure 7.3).

Candidate Gene Expression Post-Stimulated Wounding
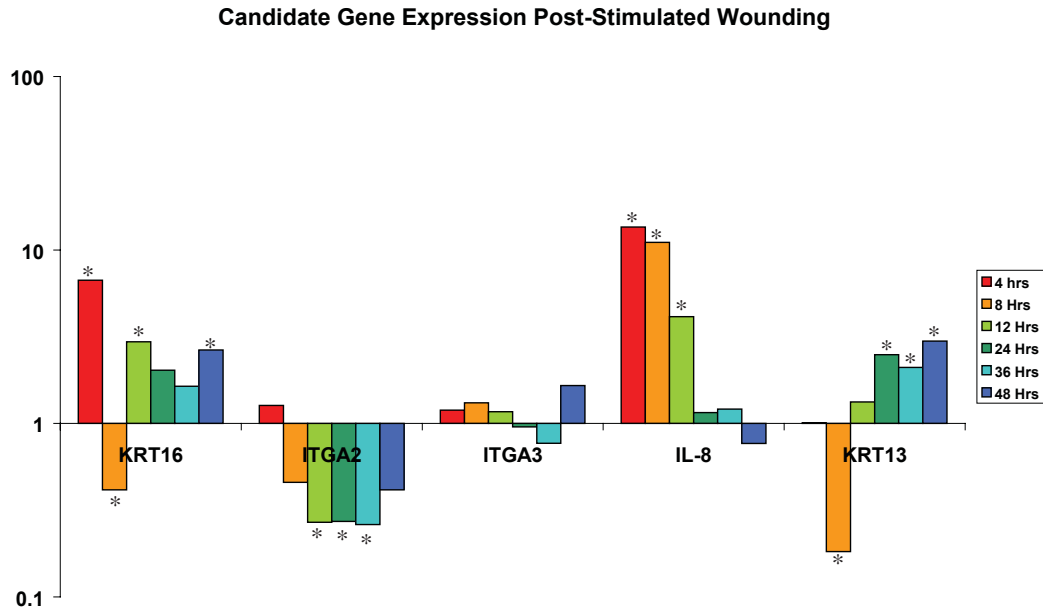
Figure 7.3 Corresponding gene expression profiles for ITGA2, ITGA3, KRT13, KRT16 and IL-8 for their role in cell polarization and migration. All values were assessed for significance using the Mann-Whitney U non-parametric test, where $P \leq 0.1$.

As displayed, Keratin 13 and 16 expression profiles both increased following stimulated wounding and declined as the need for cell polarization and migration subsided, in agreement with the populations of cells displaying elevated FT-IR keratin features at corresponding time-points[12].

Integrin expression also mirrored what was found from FT-IR mapping, with Integrin α2 expression being initially up-regulated for cell adhesion to laminin and its subsequent down-regulation as its role is taken over by Integrin α3 during active cell migration. As migratory activity began to decline, Integrin α3 expression was also found to decline and was compensated for by an up-regulation in Intergin α2 to stabilize cells post migration[3].

In turn, FT-IR mapping was found to successfully track keratinocyte organizational profiles during stimulated wounding based on protein and DNA/RNA content changes, while also accurately monitor ECM distribution and cell polarization. More specifically, the distribution of cells of varying phenotypes can be more precisely identified, as well as the localization of ECM proteins.

7.3.2 Lipid Distribution

UHCA clustering was also carried out on the lipid region of 3250-2800 cm^{-1} for methyl (CH$_3$) and methylene (CH$_2$) lipid presence. Clustering was found to display cell organization profiles considerably different to the protein and DNA/RNA counterparts, with a more heterogeneous distribution.

Lipid UHCA at 0 hours displayed a similar distribution to that of protein and DNA/RNA clustering, with regions displaying elevated CH$_3$ and CH$_2$ profiles overlapping regions of cell proliferation zones (Figure 7.4). At 12 and 24 hours post-wounding, lipid distribution profiles were also similar to the patterns observed at 0 hours, illustrating clusters of high lipid content overlapping with previously detected cell proliferation zones (Figures 7.4).
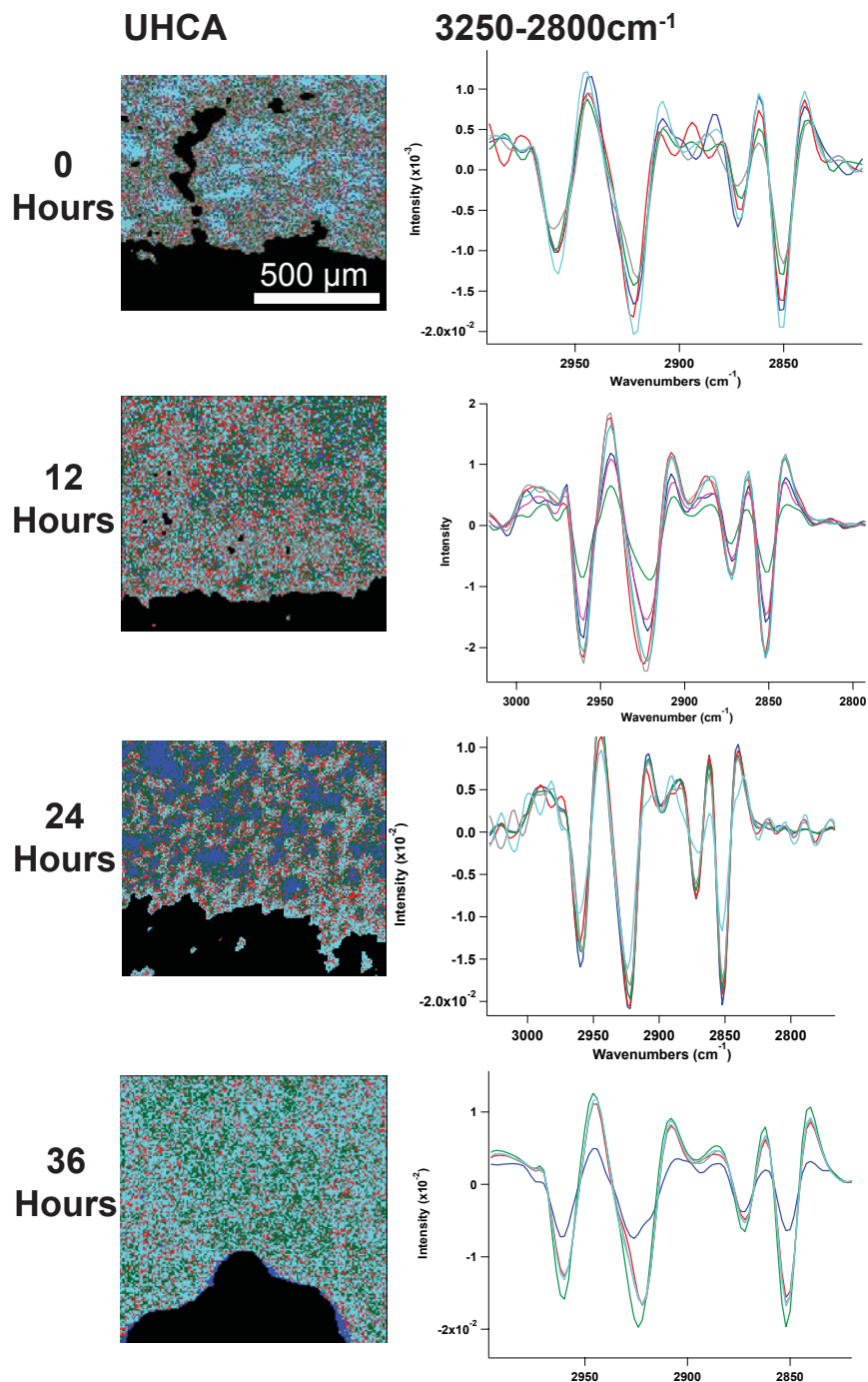
Figure 7.4 UHCA for lipid content from 2800-3250 cm^{-1}. Lipid presence displays a largely heterogeneous distribution when compared with that of the total cell clustering shown in Figure 7.1. Detected regions of elevated total lipid content could be detected (0 hours- light blue; 12 & 24 hours- dark blue) and are in agreement with proliferation regions from total cell content clustering. By 36 hours, distributions of methyl and methylene components are considerably heterogeneously distributed. Overall, CH$_2$ and CH$_3$ stretching intensities are considerably weaker then that of the fingerprint region which could make downstream UHCA more difficult.

However, visualization of CH_3 and CH_2 lipid distribution at 36 hours displayed a different allotment. In this sample, lipid distribution was largely heterogeneous compared with the clustering of previous time-points, aside from a subtle edge cluster possessing the lowest lipid content. Although the lowest lipid content was found on the migrating edge from the lack in proliferative activity, areas of cell proliferation failed to display heightened lipid profiles (Figure 7.4). This absence in distinct lipid clusters could likely result from individual cells responding to the termination of wound healing independently.

All time-points combined, total lipid content at each time-points was not found to vary significantly and was in agreement with previous findings[13], indicating that lipid content was accurately detected using FT-IR mapping.

7.3.3 RT-qPCR Analysis

To further explore lipid involvement, RT-qPCR transcript analyses of relevant genes were explored at corresponding time-points. Specifically, epidermal growth factor (EGF) and peroxisome proliferator-activated receptor β/δ (PPAR β/δ) were investigated for their known involvement in lipid synthesis and metabolism[14-17].

PPAR β/δ expression was found to vary at each time-point, depending on when viable keratinocytes were needed at the wound edge, although fluctuations were not significant[15]. Additionally, PPAR β/δ is known to assist in keratinocyte accumulation of triglycerides, which are important for cell growth[18]. The noticed differential expression of PPAR β/δ can be used to indicate when the stored fatty acids are needed during stimulated re-epithelialization. In this case, triglyceride storage is needed most during the onset and cessation of cell migration (Figure 7.5).
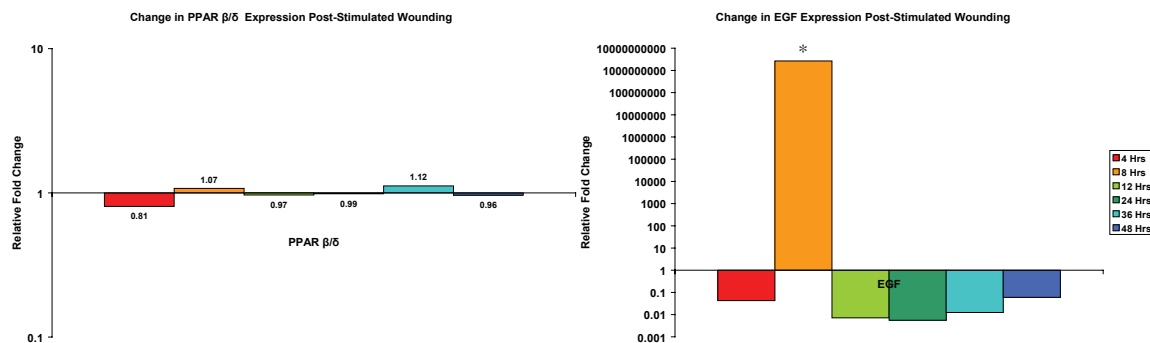
Figure 7.5 Corresponding PPAR β/δ and EGF gene expression. All values were assessed for significance using the Mann-Whitney U non-parametric test, where P≤0.05.

EGF expression was found to significantly increase following stimulated wounding, indicating that triglycerides were synthesized to sustain migration onset, cell differentiation and eventually migration cessation[19]. Through all time-points, EGF expression was found to mirror that of PPAR β/δ expression, displaying how triglycerides are being synthesized and simultaneously stored for cell differentiation and migration (Figure 5).

As the earliest level of lipid membrane polarization has already been found to occur on the single cell level[20], the disposition of membrane lipids among varying keratinocyte phenotypes was of interest. Overall, the identification of lipid components and their general distribution profiles during re-epithelialization by FT-IR mapping was visualized. However, specific lipids and their changes in distribution were not able to be clearly resolved using FT-IR mapping but can be explained when considering a few points. Primarily, a spatial resolution of 6.25 μm was clearly sufficient for elucidating overall cell phenotypes with respect to larger and more localized cellular components, like proteins and DNA/RNA content. This occurs particularly from their aggregation, as DNA and RNA are localized within the nucleus and proteins are known to aggregate during the polarization process. Although these individual components are below the FT-IR spatial resolution, this clustering into larger units permits easier detection.

With respect to lipid distribution, the plasma membrane of epidermal keratinocytes is known to be comprised of phospholipids, cholesterols and glycosphingolipids [20, 21].

However, the distribution of these lipids is largely scattered throughout the plasma membrane with some subtle known differences due to cell edge polarization[20]. Considering the diverse lipid organization, identifying areas of different lipid profiles on the cell surface poses a challenge at this resolution. From the subtle clusters that were discerned in the FT-IR mapping, these are likely to result from areas of substantial changes compared with the largely heterogeneous organization throughout the remaining sample areas. For samples at 0, 12 and 24 hours, areas of proliferation were identified from the elevated levels of plasma membrane degradation and reconstruction following cell division. For the sample at 36 hours, a significant decline in lipid content has been known to be found among migrating edge cells; although as 'contact inhibition' ceases migratory activity[22], reduced levels of proliferation occur and therefore, only very subtle differences in lipid organization could be detected.

7.4 Conclusion

With recent studies having shown that cell activities are correlated with plasma membrane re-organization, this study sought to further explore these changes through FT-IR mapping, chemomometric analysis and RT-qPCR combined.

This study was found to discern specific protein components and their varying localities from resulting spectra following UHCA false-color maps and the changes in their distribution profiles were all confirmed by transcript analyses. With respect to lipid analysis, UHCA false-color maps resulted in some cluster profiles in agreement with total content clustering. However, lipid distribution profiles were largely found to be heterogeneously distributed when compared with protein profiles. This difference favors the hypothesis that protein and lipid distribution profiles are largely independent of one another, but can result in similar distributions depending on cell function, exemplified by proliferation zones displaying high lipid and low protein profiles. Moreover, to better study individual lipid content distribution during these activities, a higher resolution via tip-enhanced Raman scattering (TERS) or coherent anti-stokes Raman spectroscopy (CARS) warrant use.

References

1. M. Mariani, P. Lampen, L. Maccoux, B. Wood and V. Deckert, 2009, **(in preparation)**.
2. A. D. Meade, F. M. Lyng, P. Knief and H. J. Byrne, *Anal Bioanal Chem*, 2007, **387**, 1717-1728.
3. W. G. Carter, E. A. Wayner, T. S. Bouchard and P. Kaur, *J. Cell Biol.*, 1990, **110**, 1387-1404.
4. L. Alibardi and M. Toni, *Prog. Histochem. Cytochem.*, 2008, **43**, 1-69.
5. E. Pauthe, J. Pelta, S. Patel, D. Lairez and F. Goubard, *Biochim Biophys Acta*, 2002, **1597**, 12-21.
6. P. C. Marchisio, S. Bondanza, O. Cremona, R. Cancedda and M. De Luca, *J Cell Biol*, 1991, **112**, 761-773.
7. W. G. Carter, E. A. Wayner, T. S. Bouchard and P. Kaur, *J Cell Biol*, 1990, **110**, 1387-1404.
8. H. Larjava, T. Salo, K. Haapasalmi, R. H. Kramer and J. Heino, *The Journal of Clinical Investigation*, 1993, **92**, 1425-1435.
9. R. A. F. Clark, J. M. Lanigan, P. DellaPelle, E. Manseau, H. F. Dvorak and R. B. Colvin, *J Investig Dermatol*, 1982, **79**, 264.
10. J. N. Barker, M. L. Jones, R. S. Mitra, E. Crockett-Torabe, J. C. Fantone, S. L. Kunkel, J. S. Warren, V. M. Dixit and B. J. Nickoloff, *The American Journal of Pathology*, 1991, **139**, 869-876.
11. J. Steude, R. Kulke and E. Christophers, *J Invest Dermatol*, 2002, **119**, 1254-1260.
12. I. Freedberg, M. Tomic-Canic, M. Komine and M. Blumenberg, *J Invest Derm*, 2001, **116**, 633-640.
13. M. Ponec, A. Weerheim, J. Kempenaar, A. M. Mommaas and D. H. Nugteren, *Journal of Lipid Research*, 1988, **29**, 949-961.
14. G. D. Sharma, P. Ottino, N. G. Bazan and H. E. Bazan, *J Biol Chem*, 2005, **280**, 7917-7924.
15. N. S. Tan, L. Michalik, B. Desvergne and W. Wahli, *American Journal of Clinical Dermatology*, 2003, **4**, 523-530.
16. M. Schmuth, C. M. Haqq, W. J. Cairns, J. C. Holder, S. Dorsam, S. Chang, P. Lau, A. J. Fowler, G. Chuang, A. H. Moser, B. E. Brown, M. Mao-Qiang, Y. Uchida, K. Schoonjans, J. Auwerx, P. Chambon, T. M. Willson, P. M. Elias and K. R. Feingold, *J Invest Dermatol*, 2004, **122**, 971-983.
17. S. Gibbs, A. Pinto, S. Murl, M. Huber, D. Hohl and M. Ponec, 2000, pp. 192-203.
18. A. B. Awad, L. A. Begdache and C. S. Fink, *The Journal of Nutritional Biochemistry*, 2000, **11**, 153-158.
19. L. Chiu-Fang, C. J. C. Jane, H. Shiaw-Min and T. Ya-Hui, 2002, pp. 275-279.
20. B. N. Giepmans and S. C. van Ijzendoorn, *Biochim Biophys Acta*, 2009, **1788**, 820-831.
21. G. van Meer and K. Simons, *Embo J*, 1986, **5**, 1455-1464.
22. M. M. Zegers, M. A. Forget, J. Chernoff, K. E. Mostov, M. B. ter Beest and S. H. Hansen, *Embo J*, 2003, **22**, 4155-4165.

Chapter 8

Lipid Distribution During Stimulated Re-Epithelialization Through Micro-Raman & Tip-Enhanced Raman Scattering (TERS)

8.1 Introduction

Lipid involvement in cell behaviour has become an area of increasing interest since lipids were found to play a role in signal transduction pathways[1]. Previous studies directed at lipids have applied techniques like detergent-resistant membrane fraction analysis[2], labelling through the use of probes[3] or have attempted spectroscopic investigations using FT-IR[4,5]. All of these techniques were capable of analyzing lipids but also possessed similar accompanying setbacks like their resolution capabilities and their ability to maintain native analyte structures.

Vibrational spectroscopic techniques have been recently applied to a myriad of biological topics[5-7] and can successfully detect lipid content. With this known, applying spectroscopic techniques like micro-Raman spectroscopy to study the distribution of particular lipid aggregates can provide label-free analysis through the acquisition of multivariate spectra. Micro-Raman spectroscopy provides an added benefit to its common spectroscopic counterpart, FT-IR, with its spatial resolution. Commercially available FT-IR can achieve a maximum spatial resolution of approximately 6.25 µm and synchrotron FT-IR reaching approximately 4 µm, while micro-Raman can provide a resolution level down to 500 nm, providing a resolution much closer to that of plasma membrane aggregates. Moreover, should a resolution level surpassing 500 nm be necessary, as is for the detection of individual plasma membrane markers, tip-enhanced Raman spectroscopy (TERS) can be applied, enabling a spatial resolution level down to a single nucleo-base[8].

TERS brings together the recognized methodology surrounding surface-enhanced Raman scattering (SERS) and scanning probe technologies, while upholding a high lateral resolution. Moreover, TERS applies the near-field enhancements that are characteristic of SERS through the illumination of nanometre particles[9-13].

Recent studies have begun applying TERS to the surface of cell membranes[14,15]. Using this technique, a small field-enhancing particle is approached toward the cell surface to reflect the Raman signal for detection. Depending on the particle shape and size,

enhancement factors in the Raman scattering can reach several orders of magnitude higher than conventional Raman spectroscopy, while also providing a spatial resolution exceeding 50 nm[16].

In this study, micro-Raman, TERS and real-time reverse transcription quantitative polymerase chain reaction (RT-qPCR) were combined for thorough sample analysis. Initially, samples were imaged using micro-Raman spectroscopy to obtain a spatial overview of plasma membrane fluctuations during migration. From this, noted changes in widespread lipid distribution were further explored by TERS and results were confirmed by RT-qPCR transcriptome analysis. Here for the first time, plasma membrane lipid distributions were successfully tracked and specific target plasma membrane features were explored. Moreover, these label-free, molecule-sensitive techniques were compared with conventional imaging techniques for accuracy and overall sensitivity.

In turn, both micro-Raman and TERS were found to be useful tools for general and specific label-free lipid target analysis, providing unsurpassed sensitivity and specificity.

8.2 Methods

All methods, unless otherwise stated below, were previously described on pages 65-69.

Table 8.1 Candidate gene assay designs. All assays were intron-spanning where possible.

NAME	FORWARD	REVERSE	PROBE #	PROBE SEQUENCE	ASSESSION #
JAM1	aagttgtcctgtgcctactcg	cggtcctcataggaagctgt	7	ctgcttcc	NM_016946.4
CLAUD 1	ccctatgaccccagtcaatg	acctcccagaaggcagaga	66	aggcagag	NM_021101.3
OCCLUDIN	ggactctacgtggatcagtatttg	aataatcatgaaccccagtacaatg	79	ccaggagg	NM_002538.2
CAV1	aagctgcctggtatatccaaaa	cccaaaggcagaatcacaat	15	tcctgctc	NM_001753.3
CAV2	aggtagttgcaaagagacatttca	ggtaatgattatgcgtcccatc	89	cagcatcc	NM_001233.3

8.2.1 Micro-Raman Imaging. HaCaT cells were imaged using a WiTec Raman imaging set-up (Ulm, Germany). A wavelength of 785 nm providing approximately 60 mW of incident power was streamed through a 60x Zeiss objective and was used to excite the sample for 20 seconds. A spatial resolution of 0.8 µm was used to image individual cells

with a 1 µm step-size, providing a spectral image possessing in the range of 5- 10,000 spectra per image. Approximately 5 cells were imaged from each sample and images were composed based on CH- stretching vibrations (3050-2800 cm^{-1}).

8.2.2 Tip-Enhanced Raman Spectroscopy (TERS) Line Scans. The TERS instrumentation has been previously described[17,18]. Briefly, 20 nm of silver (99.99% pure, Balzers Materials, Germany) coated a noncontact-mode silicon cantilever AFM tip (NSG10, NT-MDT) by thermal evaporation (BAL-TEC MDS 020 BAL-TEC GmbH) using an evaporation rate of 0.06 nm/s^{-1}. Tips were stored under argon until use within 2 days. The laser intensity was 1 mW (530.9 nm Krypton Ion) at the sample and the acquisition time was 10 seconds. Following measurements, the active tip was retracted 5 nm and a background spectrum was acquired to ensure no tip contamination producing false signals. TERS spectra were collected in the form of line scans across the region of interest along the plasma membrane and spectral features were assigned.

8.3. Results & Discussion

8.3.1 Micro-Raman Imaging

Previous studies have touched upon the importance of lipids during cell polarization and particularly during cell migration[19,20]. Here, stimulated wounding of keratinocytes in culture activated re-epithelialization. At select time-points (0 hours and 24 hours) during re-epithelialization, samples were fixed and mapped using micro-Raman spectroscopy for CH- stretching.

Following micro-Raman imaging, samples were labelled for lipid content using the histological stain Oil Red O and DAPI for nuclear identification (Figure 8.1). When compared, the traditional staining was unable to clearly display regions of lipid content within the keratinocyte monolayers, while the false-color images based on the micro-Raman analysis could clearly distinguish between regions of high and low lipid content.
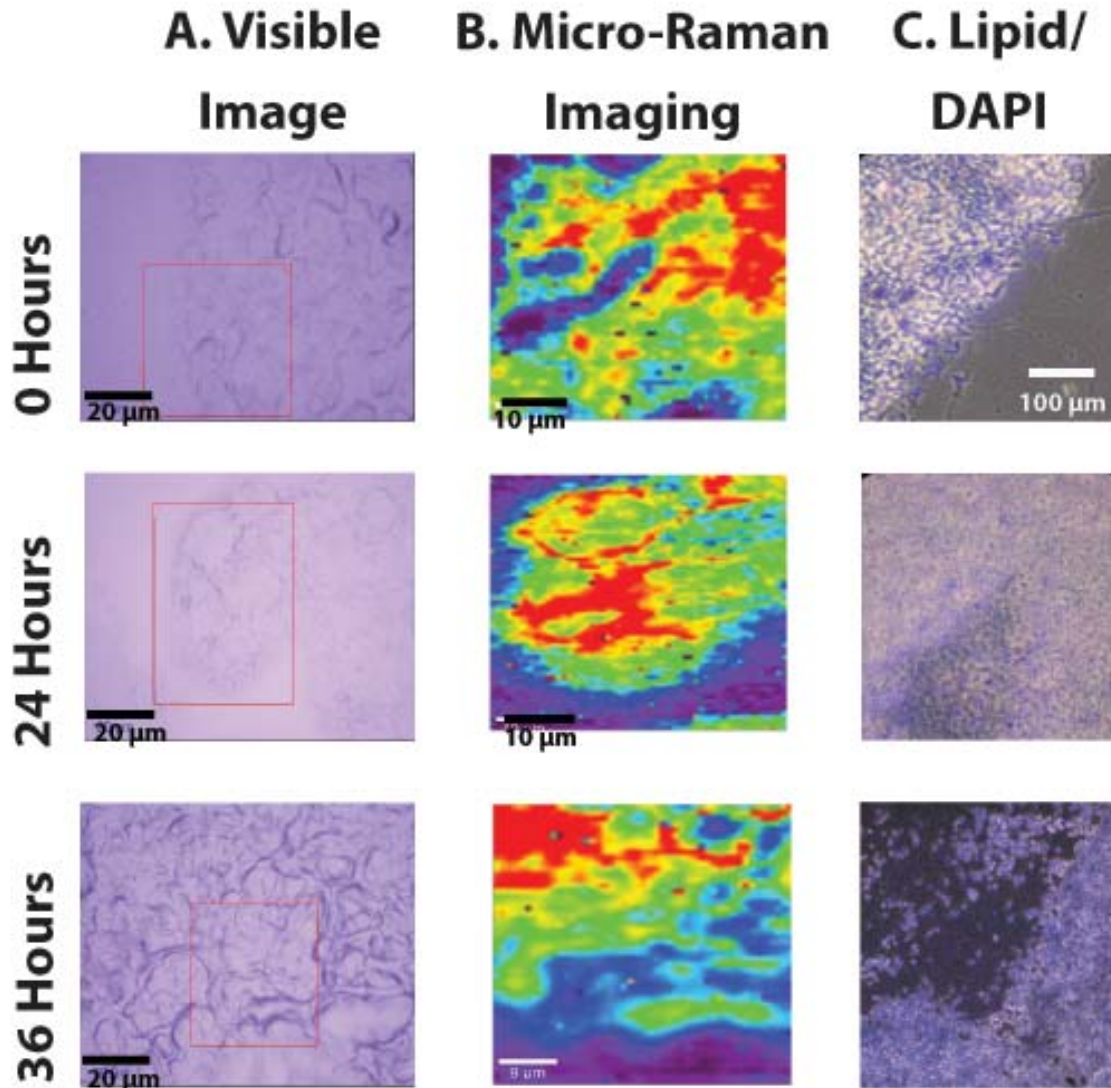
Figure 8.1 Distribution of plasma membrane lipid aggregates during stimulated wound healing. (A) Visible images of keratinocyte monolayers. **(B)** Micro-Raman imaging of keratinocyte monolayers for CH- stretching (2800-3050 cm^{-1}) of the plasma membrane. **(C)** Oil Red O histological staining and DAPI nuclear staining to visualize the distribution of lipid aggregates in the keratinocyte monolayers during stimulated wound healing.

Plasma membrane lipid distribution was found to commence at 0 hours with regions of high lipid content between cells (Figure 8.1A). This is likely to occur at sites of inter-cellular communication from the importance of lipid aggregates, like caveolae, with gap and tight junction mediated communication[21,22]. This lipid distribution among leading, edge cells was also in agreement with previous studies[4,5], where edge cells immediately following stimulated wounding remained un-activated, and thus non-polarized.

By 24 hours post-stimulated wounding, plasma membrane lipid distributions were found to have shifted, displaying elevated levels of lipid content particularly among edge cells (Figure 8.1B). These cells have also begun displaying signs of polarization through their budding from the monolayer edge and from their high lipid arrangements to surround whole cells. Cells in close contact with one another also displayed the most lipid content, indicating these regions could be of continued inter-cellular junction-mediated communication. Moreover, lipid clustering is necessary for specific functions to be carried out, as with migration via integrin clustering[23].

At 36 hours following stimulated wounding, lipid organization possessed similar features to the cells at 0 hours (Figure 8.1C). Areas of high lipid concentrations were found to be concentrated in the inner regions of the monolayer, while edge cells display lower levels of lipid presence. As the cells completed migration and the denuded region became covered, cells began to reconnect via junctions and behave as they did prior to stimulated wound healing (in this case 0 hours).

To confirm the noticed changes in tight junctions during cell migration, related gene expression of occluding (OCCLUDIN), junctional adhesion molecule 1 (JAM1) and claudin 1 (CLAUD1) were explored (Figure 8.2). In agreement with the detected changes in plasma membrane lipid distribution, transcript expression profiles of these 3 tight junction genes were found to be immediately up-regulated post-stimulated wounding to enable inter-cell communication. By 8 hours post-stimulated wounding, the transcript expression of these 3 genes was found to be down-regulated through to 12 hours. From 24 hours through 48 hours, expression was found to slowly increase while cell migration subsides and original cell contact resumes. This transcript profile is also in agreement with the previously noticed changes in micro-Raman lipid distribution profiles.

Tight Junction Candidate Gene Expression
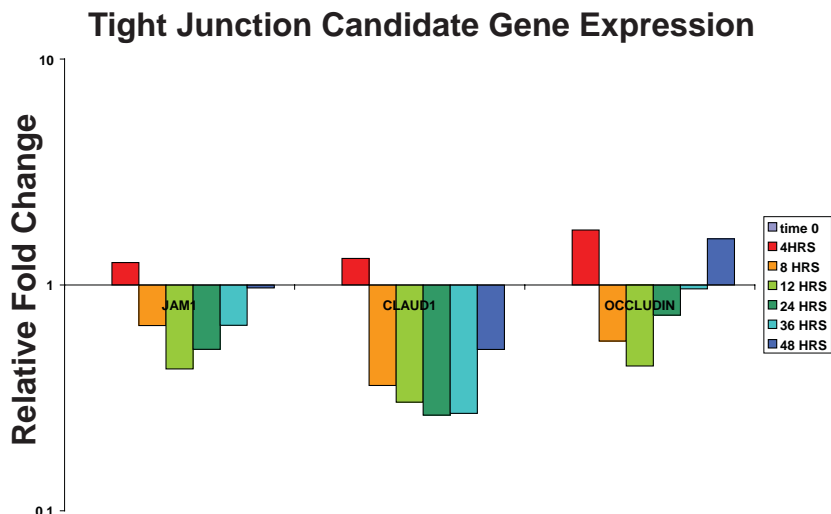
Figure 8.2 Transcript expression profiles of candidate genes related to tight junctions during stimulated wound healing. Occludin (OCCLUD), Claudin-1 (CLAUD1) and junctional adhesion molecule 1 (JAM1) expression were found to be significantly down-regulated following the onset of cell migration. Transcript expression levels for all tight junction candidate genes were found to slowly become up-regulated again as cell migration subsides and wound healing terminates. Significance was tested using the Mann-Whitney U non-parametric test, where $p \leq 0.10$.

Although micro-Raman spectroscopy was successful at tracking changes in general CH-stretching distribution profiles in the plasma membrane, individual lipid components could not be readily discerned. Traditional histological staining was also not capable of providing a spatial resolution low enough to differentiate between lipid components or between general saturated and unsaturated fatty acids. In turn, micro-Raman spectroscopy was shown to provide further insight into plasma membrane fluctuations during stimulated wounding. However, in order to further explore individual lipid components, a technique providing a higher spatial resolution remains necessary.

8.3.2 TERS Results

With the objective to obtain topographical insight into lipid distribution on the plasma membrane, TERS was applied to keratinocyte stimulated wound healing samples for migration onset (Time 0) and during migratory activity (24 hours). Specifically of interest were the distribution of caveolae, from their easily identifiable attributes (caveolar bulbs

are approximately 65 nm in diameter[24]), structural stability[24] and involvement in cell migration.

Caveolae are thought to be involved in cell migration not only because of their role with cell polarization, but also through their oriented distribution to the expanding edge of the cell[25] to aid with directional sensing of the basal and granular layers of the epidermis[26], as displayed in Figure 8.3.
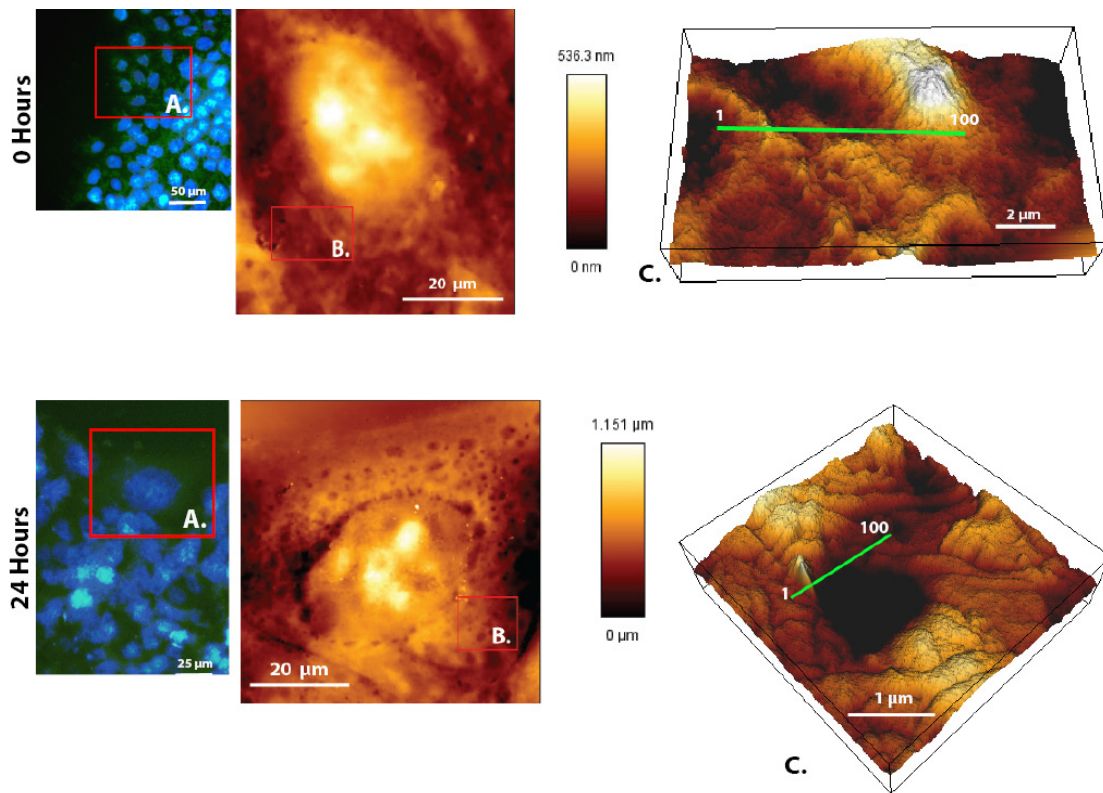
Figure 8.3 Immunofluorescence and atomic force microscopy (AFM) images of keratinocytes prior to (0 Hours) and during stimulated cell migration (24 Hours). Cells were labeled **(A)** with anti-CAV1 (FITC) and DAPI to elucidate the distribution of caveolin-1 as cells polarize for migration. CAV1 distribution is initially found within the cell cytoplasm (0 Hours) but is shown to localize on the plasma membrane by 24 Hours post-stimulated wounding, in agreement with previous findings[27]. AFM imaging **(B)** displays the distribution of these lipid inclusions throughout the cell and how they differ between time-points. Regions zoomed in on for TERS spectra **(C)** and included the striations that form around caveolar invaginations, surpassing the capabilities of conventional techniques like scanning-electron microscopy and micrographs.

Caveolae are also known to localize in the trailing edge of migrating endothelial cells, while cells migrating in 3-D have been known to display caveolae in a soluble, cytoplasmic form in the leading cell edges[25]. These cholesterol and sphingolipid-rich inclusions are found on most cell types; although as specifically abundant in terminally differentiated cells, like mature keratinocytes[28]. Despite all that is known about caveolin and their influence on cell polarization, the precise molecular composition of the coating over these lipid invaginations remains uncharacterized.

Through AFM imaging, the localization of these invaginations and their characteristic striated coatings were clearly visualized (Figure 8.3)[29], something that is not always possible with alternate techniques like micrographs[24]. AFM imaging also found the caveolin invagination to be larger than the frequently cited 100 nm size range. Although literature typically notices caveolin invaginations to range in diameter around 100 nm, studies have also found these invaginations to cycle between 'open' and 'closed' states and can fuse with one-another, enabling a considerable range to this diameter size and explaining the difference found[28,30]. Once the caveolae distribution was visualized, the TERS tip was aligned to the region of interest for line-scanning of the striated regions surrounding the caveolar invagination to better understand the molecular composition of this region.

Caveolae are known to be highly enriched in cholesterol, unlike the rest of the plasma membrane[31,32], while the caveolin-1 protein coating is a cholesterol binding protein that possesses a cholesterol binding amino acid consensus sequence[24,33,34]. Looking at the corresponding spectra for the 24 hour cell sample, noticeable features specific for the presence of only cholesterol and sphingolipids were detected at 1580 cm^{-1} [35], 1445 cm^{-1} [6, 36], 1411 cm^{-1} [21, 35], 1363 cm^{-1} [6], 1302 cm^{-1} [6], and 1164 cm^{-1} [6] (Figure 8.4). These peak intensities varied with the tip position, indicative of fluctuations in the caveolar structural composition. The presence of sphingolipids are particularly important, being a characteristic structural component of caveolae and was not detected in 0 hour TERS spectra. Additionally, an amide II peak was detected (1546-35 cm^{-1})[36] which is

characteristic of protein presence and would likely result from the tip moving over caveolar regions of caveolin-1.

When comparing the spectral features of 24 hours with that of 0 hours, considerable differences were noticed (Figure 8.4). Primarily, the number of spectral features was much greater at 0 hours. Moreover, the spectral features can be seen to vary in intensity as the tip passes over plasma membrane components, displaying the variations in the plasma membrane topography. This is particularly due to the cells at 0 hours not being polarized yet and therefore possessing a diverse distribution of expressed proteins and lipid components. Furthermore, spectral features characteristic of only protein and lipid content were detected and can be used to identify the precise localities on the cell surface where various plasma membrane contents are present.
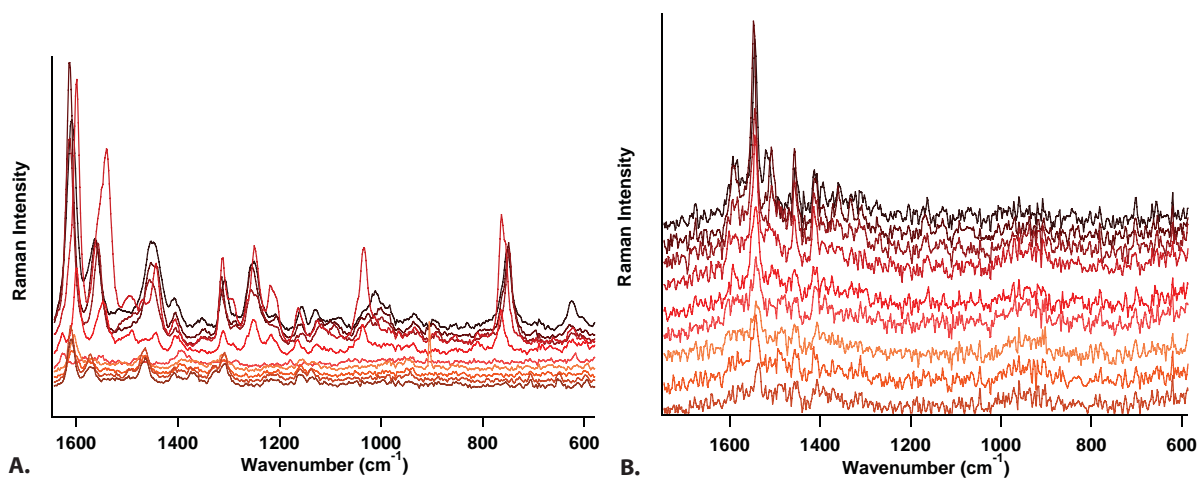
Figure 8.4 Representative TERS spectra of the plasma membrane prior to (0 Hours, A) cell migration and during (24 hours, B) cell migration. At 0 Hours **(A)**, spectral features were found to display the presence of protein and lipid components as the tip moved across the plasma membrane. Spectral features were found to increase or decrease in intensity as the tip moved over each individual component, providing topographical insight. At 24 Hours **(B)**, spectral features were found to be from mainly lipid components. Spectral intensity was found to decline in parallel with the tip passing over deeper regions of the invagination, indicating both the chemical composition of the caveolin coating and where the invagination folds inwards.

Table 8.2 Spectral assignments to detected features during Time 0 (A) and 24 Hour (B) samples.

A.

Wavenumber	Assignment	Ref.
1644	amide I, alpha-helix	[36]
1612, 1598	C=C (tyr, trp)	[6]
1563, 1558	C=C (trp, phe, tyr)	[6]
1539	Amide II	[6,7]
1489	CH def	[35]
1454, 1449	CH$_2$ stretch (lipid)	[36,6,7]
1407	CH$_3$ bending (cholesterol)	[6]
1351	CH$_3$ symm. stretch	[6]
1310	CH$_2$ twist (lipid)	[36]
1290	C-C skeleton structure, amide III	[36,7]
1263, 1248	Amide III, alpha-helix	[6]
1218, 1207	=CH bend, OPO	[6]
1163	C-O stretch, COH bend	[7]
1126	CC asymm stretch, CH?	[36,7]
1094, 1087	C-O stretch, OPO	[6,7,37]
1034	C-H in-plane (phe)	[6,37]
1000	sym ring breath (phe)	[6,37]
954	CH$_2$ (lipid)	[38]
983	CC backbone (prot)	[37]
895	C-C stretch residue	[36]
831	OPO	[37]
763, 750	ring breath (trp), OPO	[6]
748	CH$_2$ (lipid)	[6]

B.

Wavenumber	Assignment	Ref.
1752	C=O (lipid)	[38]
1677, 1657	C=C (cholesterol, sphingomyelin), amide I, beta-sheet	[36]
1603, 1596	C=C (phe, tyr, trp)	[7]
1584	C=C (cholesterol)	[6, 35]
1573, 1560, 1546	amide II	[7]
1521, 1508	C=C stretch (aromatic)	[6]
1485, 1478	CH def, CH_2	[6]
1466, 1453	CH_2 stretch (lipid)	[7]
1437	CH_2 (cholesterol)	[7, 36]
1416, 1407	CH_3 asymm stretch (cholesterol)	[6, 7]
1378, 1372, 1360, 1342	CH, CH_3 (sphingomyelin)	[7]
1332	CH_3 (cholsterol)	[36]
1313, 1302	CH_2 (sphingomyelin)	[36]
1275, 1267	amide III, =CH	[36]
1247.1204	amide III,beta-sheet, -OPO	[7]
1171, 1163	C-O stretch, COH bend	[36]
1129, 1047	CC stretch	[38]
970, 960	$OCCN^+$ (choline group of sphingomyelin) asym stretch	[39, 36]
917, 908	C-C (sphingomyelin) sym stretch	[39]
883	C-C	[36]
782	OPO	[38, 37]
725	C_4N^+ (choline group of sphingomyelin) sym stretch	[39]
702	ring breath (cholesterol)	[36]
620	CC (phe)	[36]

Further confirming the increase in caveolin presence from the 0 hour sample to 24 hours, transcript expression profiling was carried out for the integral membrane proteins caveolin-1 (CAV1) and caveolin-2 (CAV2) for their role in caveolin formation[22], and for CD44 based on its involvement with cholesterol synthesis[40]. Following stimulated wounding, transcript expression of CAV1 and CAV2 were found to be significantly up-regulated for the duration of cell migration, in agreement with previous findings[41] (Figure 8.5).

Caveolin & Cholesterol Synthesis Candidate Gene Expression
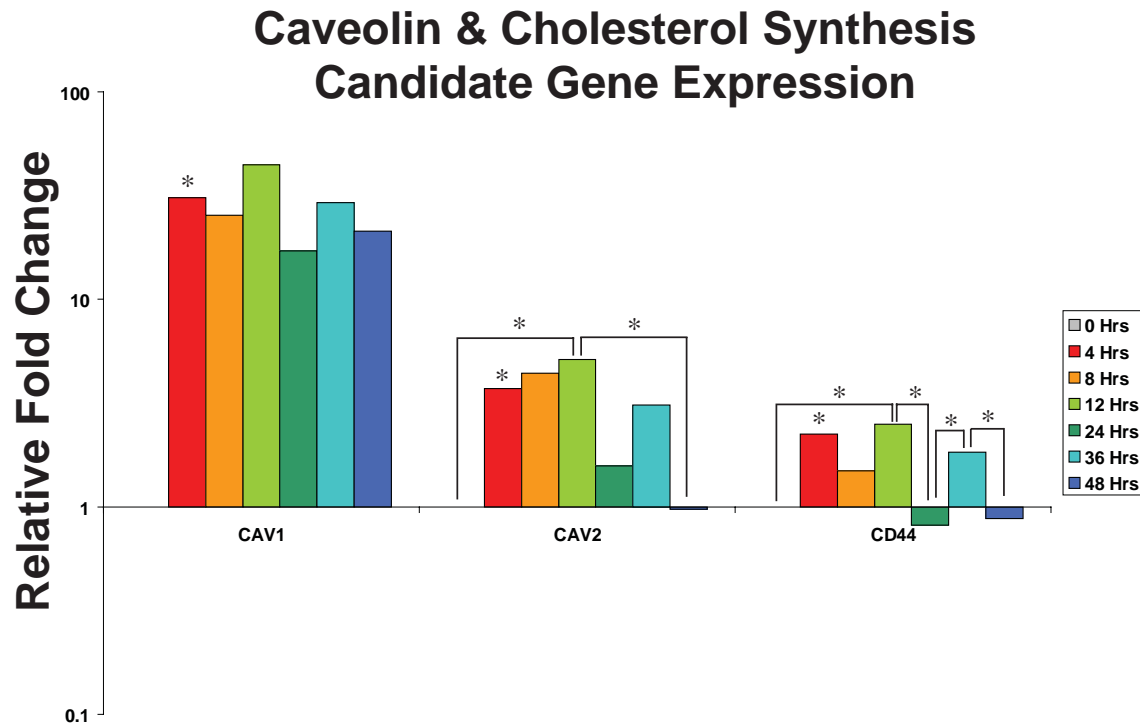
Figure 8.5 Transcript expression profiles of caveolin-1 (CAV1), caveolin-2 (CAV2) and CD44. CAV1 and CAV2 expression were both found to be significantly up-regulated following stimulated wounding, in agreement with immunofluorescence results shown in Figure 9.3. CD44 expression was also found to be significantly up-regulated initially, and is important for the synthesis of cholesterol, a major structural component of caveolae. Significance was tested using the Mann-Whitney U non-parametric test, where $p \leq 0.10$.

CAV1 remains up-regulated through 48 hours post-wounding, while CAV2 was found to also be immediately up-regulated but was less expressed as wound healing and migratory activity began to subside. CD44 was also found to be up-regulated following stimulated wounding and displayed an expression profile similar to that of CAV2, indicating that cholesterol was synthesized in the onset of wounding but subsided as overall migration and cell polarization were no longer necessary.

8.4 Conclusion

Caveolae are thought to play a paradoxical role in cell signalling and have emerged as therapeutic target leads. Through the use of micro-Raman spectroscopy and TERS, the regulation of caveolin spatial and temporal organization throughout the plasma membrane can be further explored during stages of migration to provide a better understanding of their precise role in cell signalling and polarization.

Furthermore, TERS was found to provide the necessary spatial resolution for studying plasma membrane distribution profiles. In turn, this technique showed great potential for future use in imaging applications as an approach specific for targeting plasma membrane components during cell polarization and migration. All together, this study displayed spectroscopic imaging techniques to effectively visualize lipid aggregate distribution profiles, specific plasma membrane components and shed light on the molecular composition of caveolae, whilst also providing quantitative supporting data through the use of RT-qPCR. Consequently, TERS can be applied to monitoring further individual cell membrane components and reference spectra can be collected for use in downstream TERS mapping and imaging studies.

References

1.   K. Simons and D. Toomre, *Nature Reviews*, 2000, **1**, 31-39.
2.   A. Kenworthy, *Trends in Biochemical Sciences*, 2002, **27**, 435-437.
3.   L. Kuerschner, C. S. Ejsing, K. Ekroos, A. Shevchenko, K. I. Anderson and C. Thiele, *Nature Methods*, 2005, **2**, 39-45.
4.   M. Mariani, P. Lampen, L. Maccoux, B. Wood and V. Deckert, *PNAS*, 2009, **(submitted)**.
5.   M. Mariani, B. Wood, M. Diem and V. Deckert, 2009, **(in preparation)**.
6.   C. Krafft, L. Neudert, T. Simat and R. Salzer, *Spectrochimica Acta*, 2005, **61**, 1529-1535.
7.   H. J. van Manen, Y. M. Kraan, D. Roos and C. Otto, *Proceedings of the National Academy of Sciences of the United States of America*, 2005, **102**, 10159-10164.
8.   E. Bailo and V. Deckert, *Chemical Society Reviews*, 2008, **37**, 921-930.
9.   B. Pettinger, B. Ren, G. Picardi, R. Schuster and G. Ertl, *Phys. Rev. Lett.*, 2004, **92**, 96-101.
10.   M. Anderson, *App. Phys. Lett*, 2000, **76**, 3130-3132.
11.   N. Hayazawa, Y. Inouye, Z. Sekkat and S. Kawata, *Opt. Comm*, 2000, **183**, 333-336.
12.   R. Stockle, Y. Suh, V. Deckert and R. Zenobi, *Chem. Phys. Lett.*, 2000, **318**, 131-136.
13.   A. Hartschuh, N. Anderson and L. Novotny, *J. Microsc.*, 2003, **210**, 234-240.
14.   C. Budich, U. Neugebauer, J. Popp and V. Deckert, *J. Microsc.*, 2008, **229**, 533-539.
15.   U. Neugebauer, U. Schmid and e. al., *Chem. Phys. Chem*, 2007, **8**, 124-127.
16.   D. Cialla, T. Deckert-Gaudig, C. Budich, M. Laue, R. Moller, D. Naumann, V. Deckert and J. Popp, *J Raman Spec*, 2008, **40**, 240-243.
17.   R. M. Stockle, Y. D. Suh, V. Deckert and R. Zenobi, *Chemical Physics Letters*, 2000, **318**, 131-136.
18.   A. Rasmussen and V. Deckert, *Journal of Raman Spectroscopy*, 2006, **37**, 311-317.
19.   S. Manes, E. Mira, C. Gomez-Mouton, R. A. Lacalle, P. Keller, J. P. Labrador and A. C. Martinez, *The EMBO journal*, 1999, **18**, 6211-6220.
20.   C. Gomez-Mouton, R. A. Lacalle, E. Mira, S. Jimenez-Baranda, D. F. Barber, A. C. Carrera, A. C. Martinez and S. Manes, *The Journal of cell biology*, 2004, **164**, 759-768.
21.   A. Nusrat, C. A. Parkos, P. Verkade, C. S. Foley, T. W. Liang, W. Innis-Whitehouse, K. K. Eastburn and J. L. Madara, *Journal of Cell Science*, 2000, **113 (Pt 10)**, 1771-1781.
22.   S. Langlois, K. N. Cowan, Q. Shao, B. J. Cowan and D. W. Laird, *Molecular biology of the cell*, 2008, **19**, 912-928.
23.   D. Meder and K. Simons, *Lipid rafts, caveolae, and membrane traffic*, Wiley-VCH, 2006.
24.   R. G. Parton, M. Hanzal-Bayer and J. F. Hancock, *Journal of Cell Science*, 2006, **119**, 787-796.
25.   A. Navarro, B. Anand-Apte and M. O. Parat, *Faseb J*, 2004, **18**, 1801-1811.

26. G. N. Sando, H. Zhu, J. M. Weis, J. T. Richman, P. W. Wertz and K. C. Madison, *The Journal of Investigative Dermatology*, 2003, **120**, 531-541.

27. A. Tagawa, A. Mezzacasa, A. Hayer, A. Longatti, L. Pelkmans and A. Helenius, *The Journal of Cell Biology*, 2005, **170**, 769-779.

28. A. L. Kiss, A. Turi, N. Muller, O. Kantor and E. Botos, *Micron*, 2002, **33**, 75-93.

29. G. Rothberg, J. Heuser, W. Donzell, Y.-S. Ing, G. JR and R. Anderson, *Cell*, 1992, **68**, 673-682.

30. B. Razani, S. E. Woodman and M. P. Lisanti, *Pharmacol Rev*, 2002, **54**, 431-467.

31. K. Simons and E. Ikonen, *Nature*, 1997, **387**, 569-572.

32. D. A. Brown and E. London, *Biochem Biophys Res Commun*, 1997, **240**, 1-7.

33. M. Murata, J. Peranen, R. Schreiner, F. Wieland, T. V. Kurzchalia and K. Simons, *Proceedings of the National Academy of Sciences of the United States of America*, 1995, **92**, 10339-10343.

34. X. A. Li, W. V. Everson and E. J. Smart, *Trends in Cardiovascular Medicine*, 2005, **15**, 92-96.

35. C. Krafft, D. Codrich, G. Pelizzo and V. Sergoa, *J. Raman Spec.*, 2009, **40**, 495-603.

36. I. Dreissig, S. Machill, R. Salzer and C. Krafft, *Spectrochimica acta*, 2009, **71**, 2069-2075.

37. J. W. Chan, D. K. Lieu, T. Huser and R. A. Li, *Anal Chem*, 2009, **81**, 1324-1331.

38. R. Böhme, M. Richter, D. Cialla, P. Rösch, V. Deckert and J. Popp, *J Raman Spec*, 2009, **DOI 10.1002/jrs.2433**.

39. H. Akutsu, *Biochemistry*, 1981, **20**, 7359-7366.

40. L. Y. Bourguignon, M. Ramez, E. Gilad, P. A. Singleton, M. Q. Man, D. A. Crumrine, P. M. Elias and K. R. Feingold, *The Journal of Investigative Dermatology*, 2006, **126**, 1356-1365.

41. W. P. Li, P. Liu, B. K. Pilcher and R. G. Anderson, *Journal of Cell Science*, 2001, **114**, 1397-1408.

Chapter 9

Micro-Raman Detection of Nuclear Membrane Lipid Fluctuations in Senescent Epithelial Breast Cancer Cells

9.1 Introduction

Originally identified in cultured cells, oncogenic cellular senescence is a growth-arrest mechanism that may inhibit tumor development by limiting cell division. This behavior is characterized by cells that have matured into a proliferation-resistant but metabolically-active phenotype. Senescent cell morphology also differs from that of proliferating cells by their noticeable enlargement and granulation[1]. Literature suggests that senescent cells actively secrete proteins which have the ability to produce tumor-inducing and tumor-suppressing profiles[2, 3]. Oncogenic cellular senescence is a defining feature of tumorigenesis that has proven to be of valuable interest for the diagnosis, prognosis and treatment of certain cancers[4]. Further understanding senescence will provide valuable implications for improving treatment targets in the prevention of tumorigenesis and metastasis. Yet, many associated mechanisms between proliferating cells and senescent cells remain to be thoroughly understood.

Many studies have targeted the onset of cellular senescence by observing the roles of tumor suppressors[5-7] and differentiating agents[2]. However, there have been few investigations surrounding nuclear modifications despite the significance of the nucleus' involvement in cellular function.

Signals from the cytoplasm of the cell pass through the nuclear membrane into the nuclear cytoplasm interacting with DNA and instructing specific target gene expression profiles to be expressed. The functional architecture of the nucleus, its transmembrane protein distribution and its associated impact on signal transduction and propagation has become an area of increasing interest. Moreover, as it is known that senescent cells undergo cell cycle arrest, seamless nuclear pore complex disassembly and reassembly do not occur[3]. Recent studies have displayed the advantages of cell imaging[4] for studying the structural/ functional relationship of nuclear architecture with large scale cell function between cells. Specific to the nucleus of senescent cells compared with that of their non-senescent cell counterparts, nuclear envelop modifications remain largely unexplored.

Most widespread imaging methods like immunofluorescence and immunohistochemistry implement sample labeling, provide qualitative results but provide little insight into chemical composition. Circumventing these caveats is the novel addition of micro-Raman spectroscopy to sample imaging. This technique has become increasingly attractive for biological sample analysis and imaging for multiple reasons, including the ability to visualize samples down to a 500 nm resolution without the

use of additional labels or sample perturbations. Sample components are excited through the use of a monochromatic laser and provide spectral plots based on the Raman scattering of target molecules. Resulting spectral images can provide a wealth of chemical information pertinent to cell composition, structural organization and cell functionality, whilst maintaining overall sample integrity[5-9]. From these associated benefits, micro-Raman imaging was carried out on MCF-7/NeuT cells both prior to and following doxycycline (DOX) induced ErbB2 over-expression resulting in oncogenic cellular senescence. This particular cell line provides a reproducible model system to explore the occurrence of oncogenic senescence[10].

As the nuclear envelope and internal architecture are critical for accurate overall nuclear function[11], any changes to this during the onset and maintenance of oncogenic cellular senescence could provide insight applicable to preventative and therapeutic endeavors. Using this oncogenic senescence induced system, we explored nuclear fluctuations detected through micro-Raman spectroscopy that could provide details pertinent to the onset of cellular senescence, diagnosis, prognosis and the potential for therapeutic targets.

9.2 Methods

9.2.1 Cell Culture & Raman Sample Preparation. MCF7/NeuT cells[10] were seeded onto quartz discs in a 24-well culture dish at a density of 1×10^5 cells per well. Cells were cultured in tetracycline free DMEM containing 1% P/S and 10% FCS at 37 °C in 5% CO_2 humidified air. MCF7/NeuT cells were allowed to settle and adhere to the quartz disc for 48hrs before DOX (1 ng/mL) was added to the medium. Cells were exposed to DOX for 7 days, producing a population of senescent cells. Media was then aspirated off and cells were fixed in PBS containing 2% Formaldehyde. Following chemical fixation, samples were rinsed with distilled water, wrapped in aluminum foil and frozen at -80˚C to inhibit auto-fluorescence.

9.2.2 Micro-Raman Imaging. MCF-7/NeuT cells were imaged using a Raman imaging set-up (WiTec, Ulm, Germany). A wavelength of 514.5 nm providing approximately 8 mW at sample was delivered through a 100x Nikon objective, providing a penetration depth capable of reaching the nucleus membrane[12, 13]. Spatial resolution of approximately 0.5 μm (numerical aperture 0.9) was achieved and individual cells were imaged with a 0.5 μm step-size, providing a data set with 8- 10,000

spectra. A total of 4 cells were imaged from the control (non-senescent) and senescent MCF-7 cell samples and images were composed based on CH- stretching vibrations (2800-3050 cm^{-1}).

9.2.3 Data Analysis. All spectral images were imported into CytoSpec™ for unsupervised hierarchical cluster analysis. Spectral images were subjected to a quality test to omit image regions not containing sample. Images were then vector normalized to compensate for uneven sample thickness and clustered using D-Values and Ward's algorithm. Image clustering was carried out to isolate the nucleus from the Raman image of each cell and average nuclei spectra were compared.

9.2.4 RT-qPCR. Total RNA was extracted from three samples each of senescent and control MCF7/NeuT cells in culture using the innuPREP RNA Mini isolation kit and following manufacturer's instructions (Analytik Jena GmBH, Germany). Total RNA was reverse- transcribed into complimentary DNA (cDNA) using the High Capacity cDNA reverse transcription kit (Applied Biosystems, Germany). Following reverse-transcription, control and senescent samples were tested for mRNA expression of the rat homolog, erythroblastic leukemia viral oncogene homolog 2 (NeuT), and cyclin-dependent kinase inhibitor 1A (CDKN1A/p21) to confirm cellular senescence as well as the glycoprotein Nucleoporin 210 (NUP210) for nuclear membrane fluctuations. Forward and reverse primers were designed for each gene sequence and synthesized by Metabion GmBH (Germany). Gene Sequences were obtained from the online database of the National Center for Biotechnology Information (USA). Probes were synthesized by Roche Diagnostics (UK), implementing the locked nucleic acid technology including the reporter dye fluorescein (FAM (6-carboxy fluorescene)) at the 5'-end and a dark quencher dye at the 3'-end (Table 9.1).

Table 9.1 Primer and probe assay designs for RT-qPCR use.

NAME	FORWARD	REVERSE	PROBE	PROBE SEQUENCE	ACCESSION NUMBER
ErbB2 (NeuT)	actgggaccagaactcatcg	tggggggtcccttcaaagt	22	ctccacca	NM_017003
P21; CDKN1A	tcactgtcttgtacccttgtgc	ggcgtttggagtggtagaaa	32	gggagcag	NM_000389
NUP210	tctggccactgttctgacc	tcgatgtggaggatgctgt	78	tcctcagc	NM_024923

Each RT-qPCR assay was performed in triplicate using the 96-well configuration in an ABI 7500 (Applied Biosystems, Germany). Each assay included three no-template controls. The reaction volume for each well was 20 μl and contained 10 μl 2x TaqMan® Universal PCR Master Mix (Applied Biosystems, Germany), 5 μl of RNase-free H$_2$O (Invitrogen, Germany), 0.4 μl of 20 μM forward

primer, 0.4 μl of 20 μM reverse primer, 0.2 μl of 10 μM fluorescently-labeled probe (Roche Diagnostics, UK) and 4 μl of sample cDNA was added to each well. All no-template control wells supplemented cDNA volume with 4 μl of RNase-free H_2O. The amplification conditions for all assays included 1 cycle at 50 °C for 2 minutes, 1 cycle at 95°C for 10 minutes to initiate the AmpliTaq Gold® DNA polymerase followed by 40 cycles of 95 °C for 15 seconds and 60 °C for 1 minute. RT-qPCR data was analyzed by using ABI® 7500 standard software to determine Ct and relatively quantified to time 0 gene expression profiles. Reference genes TBP (TATA binding protein) and UBC (Ubiqutin C) were selected for their stability in the MCF-7 cell line, identified as previously described[14], and were applied to all assays as an endogenous control.

9.2.5 Statistical Analysis. RT-qPCR data was assessed for statistical significance using $2^{-\Delta\Delta Ct}$ values for each candidate gene. Transformed values for each gene were imported into SPSS v.16 (SPSS UK Ltd) and assessed for significance using a Mann-Whitney U nonparametric test. P-values below 0.05 (95% confidence interval) are considered to be significant.

9.3 Results & Discussion

To ensure trustworthy cell phenotypes, we induced the expression of oncogenic ErbB2 by DOX incubation, leading to senescence. The proto-oncogene ErbB2 is over-expressed in approximately 30% of breast carcinomas and is a predictor of poor prognosis[10]. As expected, following 7 days of DOX culture, ErbB2 expression was significantly up-regulated (Figure 9.1A) compared with that of the control (P=0.05). Similar to a previous study, DOX induced over-expression of ErbB2 led to a typical senescent morphology, characterized by large cells with a granular cytoplasm and the over-expression of the senescence marker P21 (Figure 9.1B)[10].
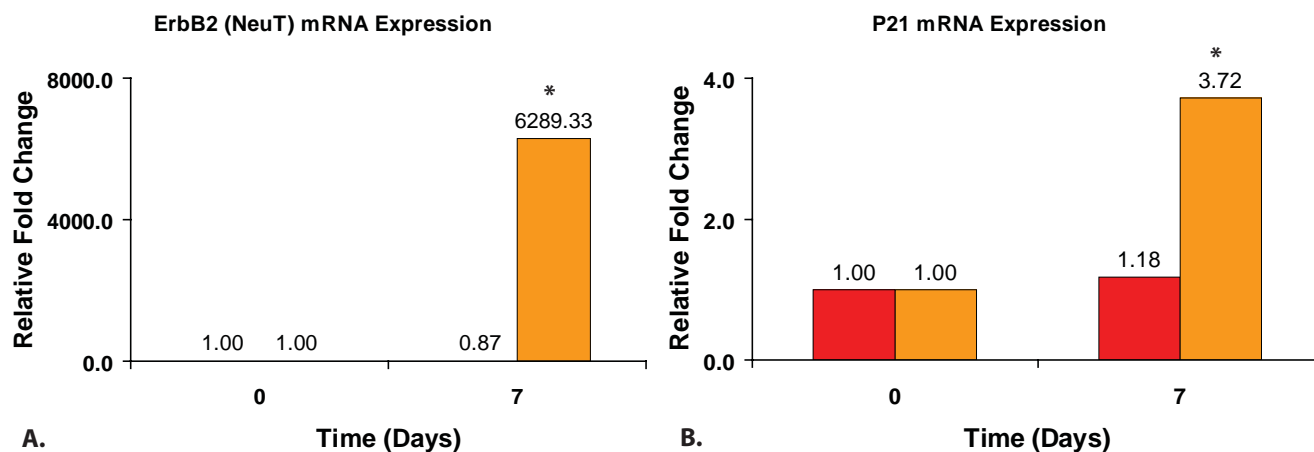
Figure 9.1 ErbB2 (A) and P21 (B) mRNA expression in MCF7/NeuT (Grey) and MCF7/EGFP Control (White) cells. Expression of ErbB2 and P21 was found to be significantly up-regulated in the MCF7/NeuT cells compared to the MCF7/EGFP cells at 7 days DOX incubation. P21 is used as a senescence-associated biomarker to confirm senescence at the transcription level. Gene expression profiles were normalized to the average gene expression of two preselected reference genes based on their overall expression stability. Statistical significance was assessed using the Mann-Whitney U non-parametric statistical test, where $p \leq 0.05$.

Following phenotype confirmation, cells were imaged using micro-Raman spectroscopy. Visible images (Figure 9.2A), chemical images based on CH- stretching (Figure 9.2B) and subsequent unsupervised hierarchical cluster analysis (UHCA) (Figure 9.2C) were obtained to identify sub-cellular localities. Upon direct inspection of micro-Raman imaging, morphological features of senescent cells were found to differ to that of the control cells.

A. Visible Image   B. Chemical Image   C. HCA Image

Control MCF-7 NeuT Cell

Senescent MCF-7 NeuT Cell
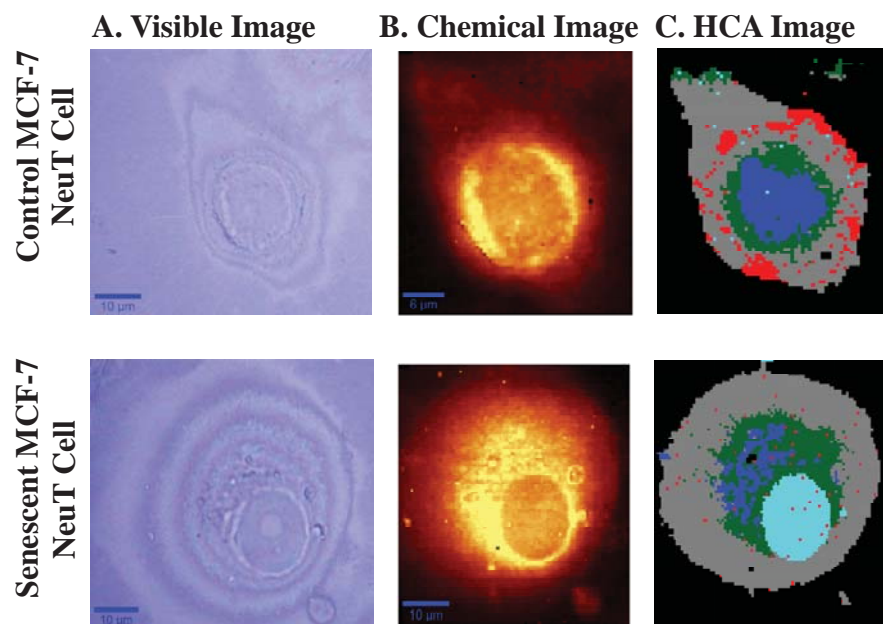
Figure 9.2 Raman imaging of single control (non-senescent) and senescent MCF-7/NeuT cells. Cells were cultured directly onto quartz substrates and fixed with formaldehyde (**A**). Individual cells from each population were imaged at a constant wavelength of 514.5 nm, providing approximately 20 mW of incident power. A lateral resolution of 0.5 µm was achieved, providing sufficient sensitivity to image sub-cellular localities. Routine instrument calibration was performed prior to sample analysis using the silicon peak. Raman images are displayed specific to CH- peak intensity (**B**) and were imported into CytoSpec™ software for unsupervised hierarchical cluster analysis (**C**). Average nuclear spectra were used for subsequent comparison of nuclear composition. Black regions fell outside of the quality test range, excluding them from subsequent cluster analysis.

Average nuclear spectra were selected for comparison following UHCA. Spectral comparisons between non-senescent MCF-7/NeuT cells (control) were found to be similar and possessed negligible fluctuations, as was the case amongst the DOX-induced senescent cell population (Figure 9.3). When comparing the average Raman spectra of control and senescent MCF-7/NeuT, the spectra initially seemed very similar in the fingerprint region (675-1800 cm^{-1}). However, upon closer inspection, subtle but reproducible spectral changes were identified and confirmed through the formation of a difference spectrum (Figure 9.3 & Figure 9.4).
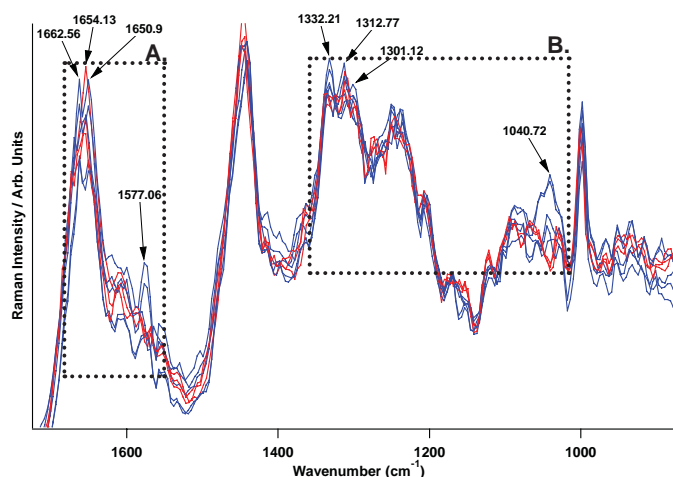
Figure 9.3 Average nuclear spectra from each imaged cell per sample (n=4). Control cell spectra are displayed in blue, whilst senescent cell spectra are displayed in red. By comparing the spectra from each sample group, subtle but reproducible differences pertinent to nuclear envelope composition were identified. Peaks specific for *–cis* and *–trans* unsaturated fatty acid isomers (1662 & 1650 cm^{-1}) were detected in the control sample (**A**). However, only the *–trans* isomer peak was detected in the senescent cell population. Additional differences were identified at 1332 cm^{-1} and 1312 cm^{-1} (**B**). These features are assigned to the presence of glycoprotein and senescent cells display a clear lack of both features.
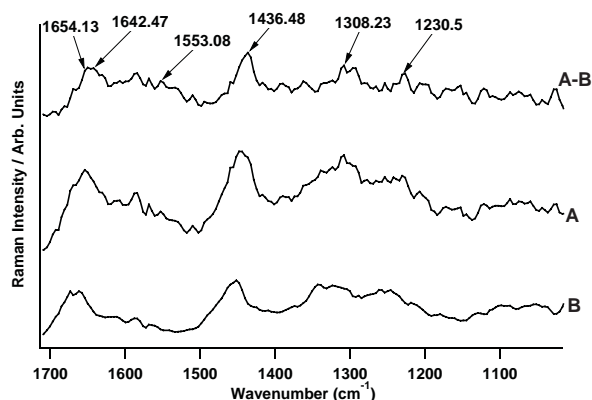
Figure 9.4 Difference spectrum from average control (non-senescent) and senescent MCF-7/NeuT cell spectra. Average spectra from the nuclei of 4 cells for each sample were combined. Using the average spectrum for the nucleus of the control and senescent cell samples, by subtracting the control spectrum (**B**) from the senescent spectrum (**A**), a difference spectrum (**A-B**) was obtained. This difference spectrum illustrates the specific features that differ between samples and at what intensity. By looking at the difference spectrum, DNA and RNA contents are found to remain consistent. However, the protein and lipid components are found to vary, specifically for Amide I (1642 cm^{-1}), Amide II (1553 cm^{-1}), CH$_2$ deformations (1436 cm^{-1}), lipid CH$_2$ twisting (1308 cm^{-1}) and anti-symmetric phosphate stretching (1230 cm^{-1}).

Differences in peaks from 1650-1662 cm^{-1} were determined between the spectra of control and senescent cells (Figure 9.3A). These spectral features are specific for unsaturated membrane lipids of –cis and –trans isomers[15]. Modifications in the presence of these features can be attributed to changes in the nuclear envelope composition. The nuclear envelope is composed of the inner and outer nuclear membranes and nuclear pores are formed by glycoproteins to monitor macromolecular transfer. The functional architecture of the nucleus has become an area of increasing interest. Cells possessing stable nuclear envelope architecture are known to possess both –cis and –trans unsaturated fatty acid isomers[16-18]. Typically, -trans isomers are known to be the most stable from their linear shape by hydrogen bond positioning at opposite ends of the double bond, which also enables the development of hydrogen intermolecular forces to reinforce the lipid conformation.[19] In the average nuclear spectrum of the control sample, peaks were found at 1654 & 1662 cm^{-1}, indicating that both –cis and –trans -isomers of unsaturated lipids were present (Figure 9.3A). When compared with the average spectrum of the senescent sample, this doublet became a single peak at 1654 cm^{-1}, showing that mainly –cis -isomers were present. From the minimal presence of -trans isomers in senescent cells, nuclear envelope organization becomes destabilized. The –cis or bent conformation induced by hydrogen atoms is positioned on the same side of the double bond leading to increased nuclear fluidity[19].

Additional spectral variances between control and senescent MCF-7/NeuT cells were detected in the 1332-1312 cm^{-1} range (Figure 9.3B). Control cells were found to possess peaks at 1332 & 1312 cm^{-1}. However, these features were missing in the senescent population. The peaks at 1332 cm^{-1} and 1312 cm^{-1} can be assigned to the presence of glycoproteins[20]. Glycoproteins are distributed throughout the nuclear membrane and permit the flow through of macromolecules from the cytoplasm into the nucleus[21-24].

The difference spectrum between the averages of all senescent cell and control cell nuclear spectra further confirms our findings of a decline in glycoprotein presence. While no differences specific to DNA and RNA content are detected, differences assigned to protein and lipid content are noticed. In addition to the already mentioned spectral variances, major spectral features at 1646 cm^{-1}, 1553 cm^{-1}, 1436 cm^{-1} and 1308 cm^{-1} were noticed (Figure 9.4). Peaks at 1646 cm^{-1} and 1553 cm^{-1} are attributed to amide's I and II[25] vibrations for protein presence, whereas peaks at 1436 cm^{-1} and   1308 cm^{-1} are due to CH_2 deformations, CH_2 twists and the protein amide III band[25].

The noticed spectral variations conclude a lack in nuclear glycoprotein amongst senescent cells. This detected decline in nuclear pore complex presence was further confirmed through RT-qPCR analysis of the only known pre-mitotic transmembrane, nuclear pore complex glycoprotein Nucleoporin 210 (NUP210)[26]. NUP210 has been identified as an integral lipid-anchored membrane protein and is known to be involved in both structural organization of the nuclear pore complex and directly related to gene regulation and mRNA transport into the cell cytoplasm[27, 28]. From RT-qPCR screening, NUP210 expression was found to be significantly down-regulated in senescent cells, indicating a decline in the nuclear membrane protein (Figure 9.5). It is important to note that a considerable down-regulation of NUP210 would affect overall cell viability. This down regulation in overall NUP210 could contribute to an inability to efficiently disassemble and reassemble the nuclear pore complexes in senescent cells, hindering their cell cycle completion[26]. Furthermore, fewer present nuclear transmembrane proteins could lead to a decline in general nuclear membrane macromolecule selectivity and stability, potentially enabling the transport of proteins exceeding the ≤ 25 kDa standard size[3, 11, 29].

ErbB2 (NeuT) mRNA Expression
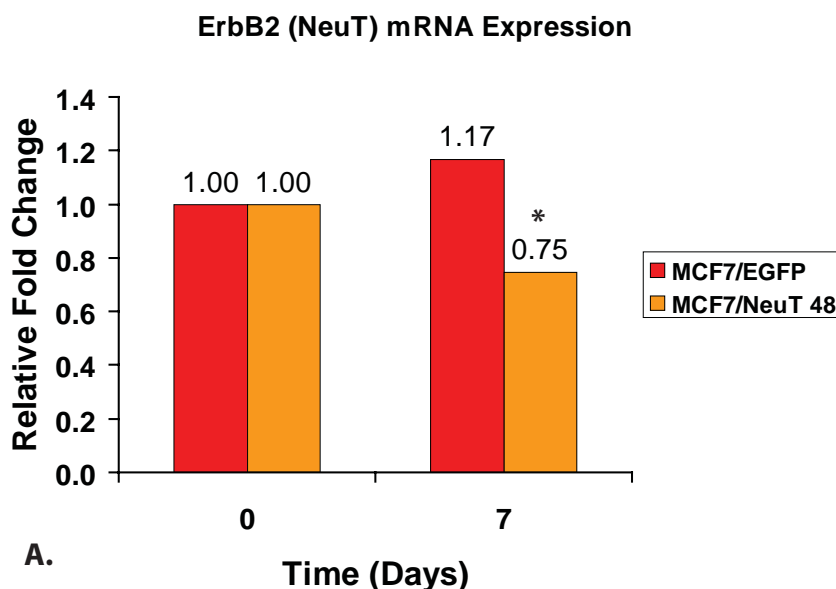
Figure 9.5 NUP210 mRNA expression in MCF7/NeuT (Grey) and MCF7/EGFP Control (White) cells. Expression of NUP210 was found to be significantly down-regulated (0.42-fold decrease) in MCF7/NeuT cells compared to the expression of MCF7/EGFP cells at 7 days DOX incubation. This confirms spectral variances in support of the inability of senescent cells to breakdown the nuclear envelop during the cell cycle and potentially creating a more penetrable nuclear membrane. Gene expression profiles were normalized to the average gene expression of two preselected reference genes based on their overall expression stability. Statistical significance was assessed using the Mann-Whitney U non-parametric statistical test, where $p \leq 0.05$.

9.4 Conclusion

Through the sensitivity of micro-Raman imaging and the combination of chemometric analysis techniques, sub- cellular localities like the nucleus can be accurately imaged and studied. By comparing the average nuclear spectra from each population, differences in lipid and glycoprotein components were detected. These differences were further confirmed through the use of RT-qPCR.

Micro-Raman imaging of senescent and control MCF-7/NeuT cells was found to identify structural modifications in the nuclear envelope. These structural changes were specific for unsaturated lipids in the nuclear membrane. Specifically, senescent cells were found to possess mainly unstable *–cis* isomers, whilst control cells possessed the more stable combination of *–trans* and *–cis* unsaturated membrane lipids. Through RT-qPCR analysis, specific nuclear pore complexes were further studied to quantify their differential expression, where the nuclear glycoprotein NUP210 was found to be significantly down-regulated in senescent cells. Nuclear glycoproteins regulate the flow-through of macromolecules into the nucleus. When down-regulated, fewer nuclear pore complexes are present, contributing to poor nuclear pore complex reassembly, disassembly and inhibition of the cell cycle. Moreover, a decline in *–trans* unsaturated isomers in the membranes result in a more disorganized membrane lipid structure and increasing overall nuclear envelope fluidity.

In turn, this study has displayed the sensitivity of label-free, micro-Raman spectroscopic imaging and RT-qPCR, as well as their combined strength. This study has also identified distinct fluctuations in the nuclear envelope between senescent and control cells, warranting further investigation for prospective therapeutic and preventative treatment targets. Moreover, from the identification of spectral variances between the two sampling populations, *in vivo* studies could be pursued for the differentiation between senescent and their non-senescent counterparts within tumors, increasing diagnosis speed. Senescence is a defining feature of tumorigenesis that could prove valuable in the diagnosis, prognosis and treatment of cancer through the use of micro-Raman imaging and RT-qPCR.

References

1. J. Campisi, *Trends in Cell Biology*, 2001, **11**, S27-31.
2. J. C. Acosta and J. Gil, *Cancer Res*, 2009, **69**, 2167-2170.
3. M. A. D'Angelo, M. Raices, S. H. Panowski and M. W. Hetzer, *Cell*, 2009, **136**, 284-295.
4. T. C. Voss and G. L. Hager, *Biochimica et Biophysica Acta*, 2008, **1783**, 2044-2051.
5. C. Matthäus, T. Chernenko, A. Kale, V. Torchilin and M. Diem, *Molecular Pharmaceutics*, 2008, **5**, 287-293.
6. C. Krafft, B. Dietzek and J. Popp, *Analyst*, 2009, **134**, 1046-1057.
7. F. Draux, P. Jeannesson, A. Beljebbar, A. Tfayli, N. Fourre, M. Manfait, J. Sule-Suso and G. D. Sockalingum, *Analyst*, 2009, **134**, 542-548.
8. H. J. van Manen, A. Lenferink and C. Otto, *Anal. Chem.*, 2008, **80**, 9576-9582.
9. C. W. Freudiger, W. Min, B. G. Saar, S. Lu, G. R. Holtom, C. W. He, J. C. Tsai, J. X. Kang and X. S. Xie, *Science*, 2008, **322**, 1857-1861.
10. T. M. Trost, E. U. Lausch, S. A. Fees, S. Schmitt, T. Enklaar, D. Reutzel, L. R. Brixel, P. Schmidtke, M. Maringer, I. B. Schiffer, C. K. Heimerdinger, J. G. Hengstler, G. Fritz, E. O. Bockamp, D. Prawitt, B. U. Zabel and C. Spangenberg, *Cancer Res*, 2005, **65**, 840-849.
11. A. C. Rowat, J. Lammerding and J. H. Ipsen, *Biophys J*, 2006, **91**, 4649-4664.
12. R. Hine, *Membrane*, 3rd. Edition edn., Checkmark, New York, 1999.
13. R. Reichelt, A. Holzenburg, E. L. Buhle, Jr., M. Jarnik, A. Engel and U. Aebi, *J Cell Biol*, 1990, **110**, 883-894.
14. J. Vandesompele, K. De Preter, F. Pattyn, B. Poppe, N. Van Roy, A. De Paepe and F. Speleman, *Genome Biol*, 2002, **3**, RESEARCH0034.
15. C. Onogi, C. Motoyama and H. Hamaguchi, *J Raman Spec*, 2008, **39**, 555-556.
16. C. Chatgilialolglu and C. Ferrerri, *Fatty Acids & Phospholipids*, Wiley-VCH, 2006.
17. R. Ledeen and G. Wu, *Journal of Lipid Research*, 2004, **45**, 1-8.
18. A. Alessenko and E. Burlakova, *Bioelectrochemistry*, 2002, **58**, 13-21.
19. W. Rawicz, K. Olbrich, T. McIntosh, D. Needham and E. Evans, *Biophys. J.*, 2000, **79**, 328-339.
20. Y. Tomimatsu, J. R. Scherer, Y. Yeh and R. E. Feeney, *J Biol Chem*, 1976, **251**, 2290-2298.
21. B. Burke and C. L. Stewart, *Annual Review of Genomics & Human Genetics*, 2006, **7**, 369-405.
22. M. L. Tomassoni, D. Amori and M. V. Magni, *Biochem Biophys Res Commun*, 1999, **258**, 476-481.
23. M. Suntharalingam and S. R. Wente, *Developmental Cell*, 2003, **4**, 775-789.
24. Y. Gruenbaum, A. Margalit, R. D. Goldman, D. K. Shumaker and K. L. Wilson, *Nature Reviews*, 2005, **6**, 21-31.
25. H. Edwards, *Biological applications of Raman spectroscopy. Infrared and Raman spectroscopy of biological materials (practical spectroscopy)*, 2000.
26. V. Galy, W. Antonin, A. Jaedicke, M. Sachse, R. Santarella, U. Haselmann and I. Mattaj, *Journal of Cell Science*, 2008, **121**, 317-328.
27. E. Prokhortchouk and P. A. Defossez, *Biochim Biophys Acta*, 2008, **1783**, 2167-2173.
28. U. F. Greber, A. Senior and L. Gerace, *Embo J*, 1990, **9**, 1495-1502.
29. C. P. Lusk, G. Blobel and M. C. King, *Nature Reviews*, 2007, **8**, 414-420.

Chapter 10

Conclusion & Outlook

The need to better understand individual cell mechanisms and their relation to larger scale systems like whole tissues has become critical, resulting from the demand for increasingly specific therapies, personalized diagnostics and preventative medicine. The focus of this study aimed to investigate cell-cell and cell-extracellular-matrix interactions in wound healing from its potential to supply significant, novel insights on fundamental cell behaviors like cell polarization, cell communication and cell organizational preferences. From the development of advanced analytical methods and applications of spectroscopic techniques for single component or full sample imaging, these topics can be further delved into[1].

As the demands for pharmaceutical and diagnostic targets becomes increasingly specific, the ability to obtain data pertinent to molecular composition and maintain the spatial-temporal analyte distribution in context of the whole sample through imaging (tissue or cell monolayer) while preserving the sample for downstream analysis has become vital. The joining of FT-IR and Raman spectroscopies with microscopy has enabled the breadth of their applications to expand considerably in the direction of the bio-medical sciences, filling the current caveat in bio-analysis and bio-medical diagnostics.

This combination has lead to the quantitative, non-invasive analysis of specific localities or the imaging of whole samples, providing a resolution below the micrometer level while maintaining spatio-temporal organization. From its high resolution and chemical-rich spectra, accurately filtering the many intrinsic spectral components of FT-IR and micro-Raman spectra has lead to the development of multiple algorithms to de-convolute heterogeneous samples and provide quantitative insight. Although absolute quantification of raw spectral data remains complicated to achieve, relative quantification can be readily achieved, surpassing that of most other conventional imaging techniques.

Likewise, as medicine and related industries leaning more and more towards quantitation, all techniques implemented for diagnostic use must be capable of providing some degree of quantification. Vibrational spectroscopies possess an intrinsic degree of quantitation along with multivariate data, compared with the traditional univariate data obtained from conventional imaging techniques. This is of particular interest for the highly complex and heterogeneous samples often found in biological studies.

For single spectrum analyses, applying methods like band deconvolution can assist in relative sample evaluation[2]. Absolute quantification with respect to sample heterogeneity versus molecular quantity can be achieved with imaged samples by applying methods like HCA and PCA. Through the use of hyper-spectral data clustering methods and the sensitivity of micro-Raman analysis, sample heterogeneity can be clearly visualized and measured with a theoretical single molecule limit of detection.

Although FT-IR can span tens of microns and micro-Raman can reach sub-micron resolution, progressively more sensitive spectroscopic techniques will enable better spectral quantification by assessing individual cellular components. Techniques like tip-enhanced Raman spectroscopy (TERS) are already pushing the boundaries of resolution and sensitivity limits, while upholding the associated benefits of its vibrational spectroscopic counterparts like non-invasive, multivariate sample analysis. TERS in particular can provide a lateral resolution down to 10 nm, comparable to the size of the tip used and smaller then the majority of sub-cellular components[3].

While vibrational spectroscopies provide detailed chemical insight into sample composition, their applications among biological studies and biomedical diagnostics remain relatively new. In lieu of this, technique combination with an industry standard like RT-qPCR can provide profitable means of obtaining more thorough, quantitative sample analysis on the transcript level while confirming phenotypic spectroscopic detections.

From this study, the benefits of combining vibrational spectroscopic imaging with chemometric data analyses and RT-qPCR have clearly displayed their strengths as combined techniques for *in vitro* cell studies. Commencing with assessing the effects of fixation on spectroscopic sample analysis to more complex endeavors like exploring *in-vitro* fundamental cell-cell mechanisms enforced during epidermal re-epithelialization, vibrational spectroscopy and RT-qPCR have displayed great potential for applications into more diverse *in-vitro* model systems and for further use in areas of biomedical diagnostics including cancer metastasis, tissue engineering and drug penetration.

In order to continue advancing these techniques, technical advancements will be necessary to decrease the time needed for sample imaging, while also improving the current level of automated sample imaging. Automated sample imaging at a faster rate will greatly aid technique adaptations to

biomedical diagnostics as it will take into consideration vital aspects like technique standardization and high-throughput sample analyses. Additionally, from the growing size of complex data sets that will result from technique advancements, more readily available and specific chemometric applications will also be needed for adequate, quick and specific data deconvolution.

As FT-IR and micro-Raman spectroscopies gain acclaim in bio-medicine and significant spectral databases are developed, quantification capabilities are likely to develop synergistically. In turn, as the potential for quantification expands, FT-IR and micro-Raman spectroscopies will continue to deliver in bio-medical applications. Moreover, in view of the associated benefits of vibrational spectroscopies with quantitative gene profiling, the future of heterogeneous tissue research looks promising and capable of integrating various disciplines of science, from translational medicine to systems biology, for the facilitation of broad-spectrum, reproducible and quantitative data.

References

1.   S. MacNeil, *Nature*, 2007, **445**, 874-880.
2.   G. Thomas Jr and D. Agard, *Biophys J*, 1984, **46**, 763-768.
3.   E. Bailo and V. Deckert, *Chem Soc Rev*, 2008, **37**, 921-930.

Appendix A

1. **Bio-Rad Automated Gel Electrophoresis Results**

2. **Microarray Results**

3. **Reference Gene Results**

1. Bio-Rad Automated Gel Electrophoresis Results

Electrophoresis Chip 1
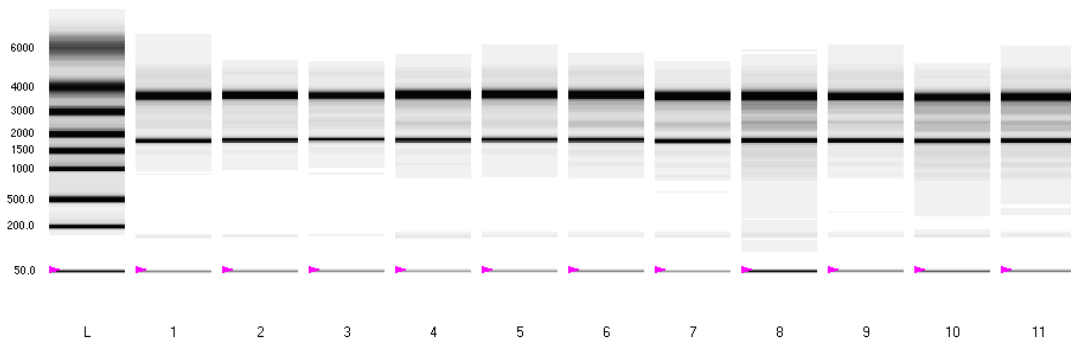
Electrophoresis Chip 2
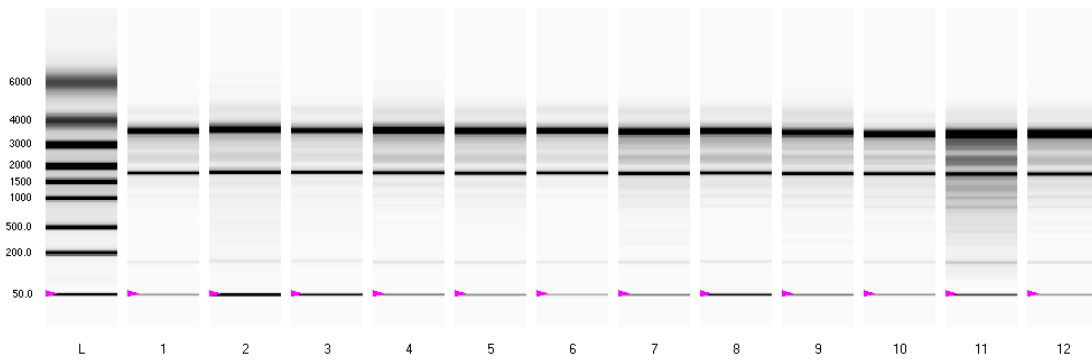
Electrophoresis Chip 3
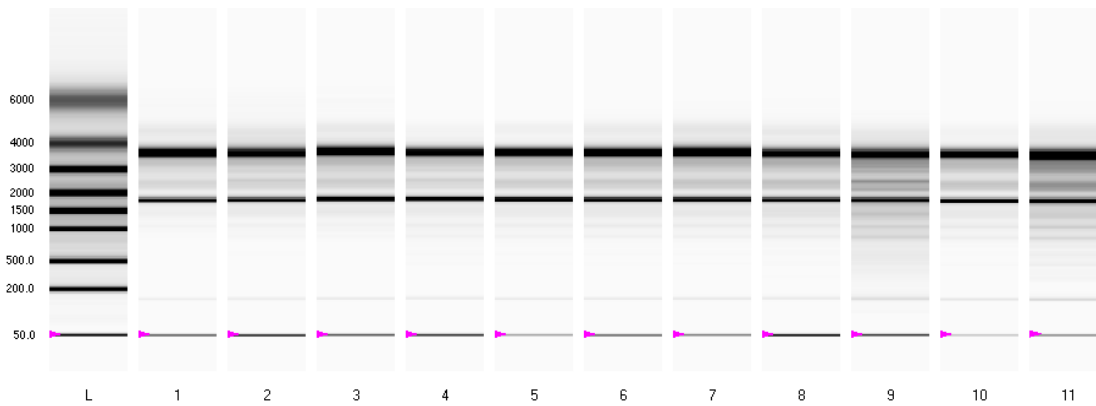
Electrophoresis Chip 4
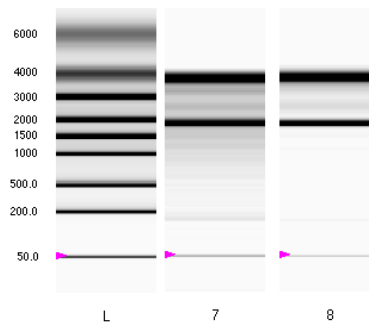
Gel # & Well #	Sample ID	ng/ul	Bio-Rad Conc's	260/280	260/230
2,1	0hrs hacat	133.05	273.49	1.98	0.51
1,1	0hrs hacat b	133.82	149.35	2.06	1.37
3,1	0 hrs c	68.75	125.06	2.11	1.21
1,2	30sec hacat	85.22	117.25	2.06	1.17
2,2	30sec hacat b	23.8	62.59	2.08	0.62
3,2	30 sec c	44.24	95.16	2.08	0.49
1,3	30 min hacat	81.23	112.93	2.09	0.32
2,3	30 min hacat b	40.32	97.01	2.12	0.21
3,3	30 min c	65.14	122.58	2.07	1.49
2,4	1hr hacat	94.86	256.98	2.06	2
1,4	1hr hacat b	150.48	186.31	2.03	2.01
3,4	1 hr c	49.65	84.57	2.1	0.33
2,5	2hr hacat	115.33	256.55	2	1.55
1,5	2hr hacat b	111.3	145.27	1.97	1.86
3,5	2 hrs c	84.17	198.56	2.1	0.78
2,6	4hrs hacat	123.07	309.38	1.54	1.14
1,6	4hrs hacat b	101.7	132.99	2.03	1.68
3,6	4 hrs c	47.82	123.38	2.07	0.83
2,7	8hrs hacat	104.7	255.06	2.03	1.48
1,7	8hrs hacat b	123.5	164.91	2.07	1.93
3,7	8 hrs c	76.42	171.25	2.05	1.73
2,8	12hrs hacat	48.17	119.98	2.13	0.71
1,8	12hrs hacat b	53.83	65.37	2.11	0.8
3,8	12 hrs c	45.83	81.21	2.03	0.34
2,9	24 hrs hacat	76.43	225.93	2.09	0.59
1,9	24 hrs hacat b	82.69	111.94	2.08	0.8
3,9	24 hrs c	25.59	144.09	2.07	1.54
2,10	36 hrs hacat	114.83	236.09	2	0.27
1,10	36 hrs hacat b	71.74	100.16	2.07	0.49
3,10	36 hrs c	159.31	335.99	2.09	1.44
2,11	48 hrs hacat	138.74	267.28	2.1	0.63
1,11	48 hrs hacat b	105.56	122.92	2.11	0.51
3,11	48 hrs c	180.59	150.13	2.09	1.44
4,7	96 hrs hacat	127.5	253.25	2.08	1.47
2,12	96 hrs hacat b	129.2	339.41	2.08	1.2
4,8	96 hrs c	158.46	248.74	2.06	2.09

2. Microarray Results

Sample ID	ng/ul	260/280	260/230	Total Yield
HaCaT	334.01	2.02	2.39	13.3604
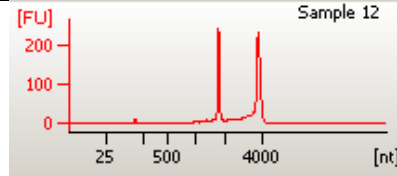
Overall Gene Expression of Basal Keratinocytes

HaCaT Cell Surface Marker Gene Expression

Gene Expression Dataset

Project	06-05-2008 Melissa OHS-055	
Catalog #	Oligo GEArray Human Cell Surface Markers Microarray, OHS-055	
Density	Average	
Clover	Clover Off	
Total Arrays	6	
Total Groups	3	
Array Name	HaCaT	
Assigned Group	Group 3	

		HaCaT	
		spot intensity	local background
Position	Symbol		
1	RPS27A	20704.80	3653.33
2	ACE	302.07	339.75
3	ACTA2	148.77	144.46
4	ADAM8	192.86	148.60
5	ADIPOQ	125.20	134.13
6	ALCAM	130.43	125.13
7	C5AR1	118.37	125.59
8	CD14	137.73	128.03
9	CD160	169.60	214.00
10	CD163	167.00	240.61
11	CD19	137.23	138.09
12	CD1A	217.85	158.06
13	CD1C	148.63	141.80
14	CD1D	133.13	131.48
15	CD2	120.83	133.05
16	CD209	169.40	134.95
17	CD22	137.53	149.01
18	CD24	269.82	162.51
19	CD244	133.40	135.87
20	CD28	137.33	136.17
21	CD33	139.17	131.95
22	CD34	129.17	135.21
23	CD37	244.61	159.12
24	CD38	121.20	132.97
25	CD3D	163.93	164.94
26	CD3G	163.90	156.85
27	CD247	144.70	150.74
28	CD4	263.97	169.40
29	CD40	151.63	169.37
30	CD40LG	136.67	144.03
31	CD5	125.10	145.82
32	CD6	144.70	140.53
33	CD63	1734.27	416.56

		HaCaT	
Position	Symbol	spot intensity	local background
34	CD68	268.00	183.08
35	CD69	148.67	151.31
36	CD7	141.50	150.33
37	CD72	1137.88	345.07
38	CD74	148.53	151.41
39	CD79A	633.21	248.36
40	CD79B	138.97	137.28
41	CD80	154.67	156.89
42	CD83	313.39	183.10
43	CD86	153.93	152.24
44	CD8A	158.67	150.92
45	CD8B	149.53	153.13
46	CD96	161.93	149.26
47	CDH5	161.97	153.28
48	CHIT1	150.40	144.91
49	CHST10	170.13	163.71
50	CMA1	173.10	159.77
51	COL1A1	142.17	153.81
52	COL1A2	144.43	142.81
53	COL3A1	142.93	146.87
54	CR2	149.83	148.99
55	CSF1R	152.20	150.19
56	CTLA4	145.27	145.13
57	DPP4	172.13	179.08
58	ENG	181.66	158.66
59	FABP4	169.67	166.95
60	FAS	140.10	151.73
61	FCER1A	146.70	144.99
62	FCER2	150.53	152.34
63	FCGR1A	152.40	151.52
64	FCGR3B	141.70	151.47
65	FSCN1	980.86	330.01
66	HLA-A	244.33	208.73

Position	Symbol	HaCaT spot intensity	HaCaT local background
67	HLA-DRA	153.60	145.29
68	ICAM2	140.57	136.99
69	IL12RB1	137.80	137.34
70	IL1R2	317.81	179.58
71	IL2RA	166.97	172.74
72	ITGA1	206.60	466.83
73	ITGA2	1989.85	548.44
74	ITGA3	2531.16	610.85
75	KRT72	163.97	218.28
76	KLRB1	115.23	130.51
77	KLRC1	131.67	127.53
78	KLRD1	131.63	190.93
79	KRT10	923.48	342.42
80	KRT13	25166.58	4780.33
81	KRT17	7223.13	1292.13
82	KRT18	2488.42	523.15
83	KRT19	6011.60	1078.15
84	KRT4	470.69	256.68
85	KRT5	174.57	166.95
86	KRT8	3147.33	746.24
87	LAG3	130.53	156.79
88	MCAM	147.20	164.25
89	MS4A1	175.40	165.03
90	MUC1	166.10	177.23
91	MYH10	148.90	175.09
92	MYH11	157.63	177.95
93	MYH9	1252.54	322.37
94	MYOCD	156.27	162.55
95	NCAM1	144.80	142.83
96	NOS3	146.80	142.95
97	NT5E	176.80	172.63
98	PECAM1	164.90	183.61
99	PH-4	158.63	153.69

Position	Symbol	HaCaT spot intensity	HaCaT local background
100	PROCR	276.31	180.75
101	RETN	254.10	191.27
102	S100A8	149.93	153.14
103	SELE	158.43	152.05
104	SELP	155.43	148.21
105	ST6GAL1	383.91	212.96
106	TACSTD1	1960.58	457.52
107	TEK	175.40	171.55
108	THBD	612.92	233.31
109	TNFRSF4	432.49	233.13
110	TNFRSF8	189.47	185.31
111	CD70	198.43	185.33
112	TPSAB1	164.47	169.09
113	VCAM1	207.57	356.89
114	VWF	580.48	362.74
115	PUC18	350.57	1065.03
116	Blank	333.43	1059.91
117	Blank	361.80	1224.86
118	AS1R2	379.50	1257.93
119	AS1R1	281.07	599.89
120	AS1	563.27	2180.91
121	**GAPDH**	8791.17	1329.87
122	**B2M**	3475.81	816.49
123	**HSP90AB1**	31197.76	6277.23
124	**HSP90AB1**	31742.94	5605.57
125	**ACTB**	33167.29	5732.81
126	**ACTB**	28975.25	5374.95
127	BAS2C	15097.97	3122.18
128	BAS2C	61327.40	15378.62

Green: denotes reference genes applied for sample normalization

3. Reference Gene Results

HaCaT Reference Gene Analysis using geNorm® (http://medgen.ugent.be/~jvdesomp/genorm/)

Table 1. geNorm® sample normalization results for HaCaT cells.

|	B2M	HMBS	YWHAZ	UBC	TBP	SDHA	PPIA	HPRT	ATCB	RPL32	RPL13A	GAPDH	Normalisation Factor
HaCaT1	5.07E-01	9.72E-01	8.68E-01	2.40E-01	1.00E+00	5.33E-01	1.00E+00	5.38E-01	9.51E-01	1.00E+00	6.88E-01	6.69E-01	0.9029
HaCaT2	1.00E+00	1.00E+00	1.00E+00	1.00E+00	7.07E-01	6.21E-01	9.09E-01	8.93E-01	1.00E+00	7.78E-01	8.07E-01	8.70E-01	1.0264
HaCaT3	6.73E-01	9.84E-01	9.52E-01	8.08E-01	4.02E-01	1.00E+00	9.59E-01	1.00E+00	9.63E-01	3.67E-07	1.00E+00	1.00E+00	1.0790
M < 1.5	1.602	1.467	1.454	2.073	1.912	1.639	1.513	1.572	1.465	12.338	1.494	1.485	
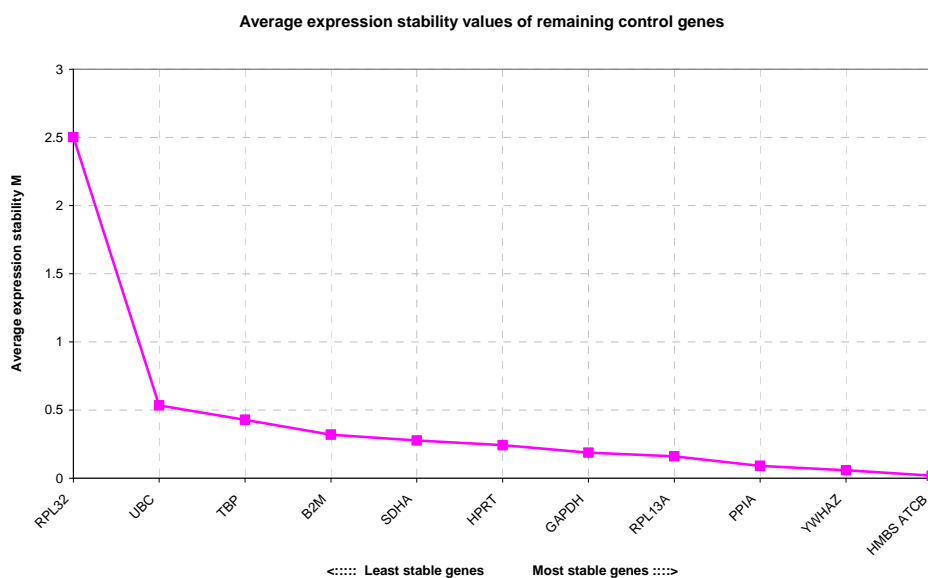
Figure 1. geNorm® results from HaCaT inter-sample normalization. This series of calculations is carried out to identify the most and least stable genes within a sample based on their M-value. Here, HMBS and ATCB display the most stability
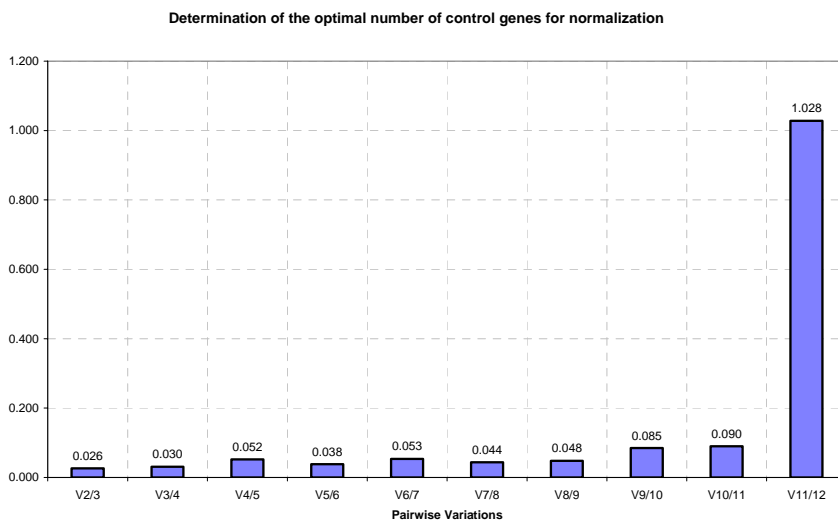

Figure 2. geNorm® results from HaCaT inter-sample normalization. This series of calculations is carried out to indicate the pairwise variation 'V' between two sequential normalization factors including an multiple genes. Here, HMBS and YWHAZ display the most stability.

Conclusion: use **YWHAZ** & **HMBS** as reference genes

These genes were selected based on their overall stability (Graph 1) and their M-Value ratio (Graph 2) and are highlighted in the geNorm® normalization results (Table 1).

Curriculum Vitae

Melissa M. Mariani AMSB
MSc Immunology & Immunogenetics

EDUCATION

Jan. 2007- Present
PhD at ISAS – Institute for Analytical Sciences, Dortmund
Theme: Vibrational Spectroscopy for Fundamental Cell Behavior Analyses in a Wound Healing Model
Supervisor: PD Dr. Volker Deckert

Sept. 2005- Dec.2006
MSc Studies & Thesis- University of Manchester, Manchester, UK
Theme: Immunological Responses to Intestinal Infections: The *Trichuris muris* Mouse Model
Obtained: MSc Immunology & Immunogenetics
Supervisor: Dr. Kathryn Else

Sept. 2002- May 2005
BSc Studies & Thesis- Oxford Brookes University, Oxford, UK
Laboratory-Based Thesis Theme: The Production of Monoclonal Antibodies to Anti-Müllerian Hormone
Supervisor: Prof. Dr. Nigel P. Groome
Research-Based Thesis Theme: The Medicalization of Behavior
Supervisor: Prof. Dr. Dick Craven
Obtained: BSc(Hons) Biology, concentration on Molecular Biology & Immunology

AFFILIATIONS & AWARDS

AFFILIATIONS
- Associate Member of the Institute of Biology, UK (AMSB)
- Affiliate Member of the Royal Society of Chemistry
- Associate Member of the GDCh (German Chemical Society)

AWARDS
- Poster Prize winner, ANAKON 2009
- Boehringer Ingelheim travel grant recipient to collaborate with Prof. Dr. Max Diem at Northeastern University, Boston, MA (Nov. 2008)
- Received a Bursary to attend SPEC 2008, Sao Paolo, Brazil (Oct. 2008)
- Received a Bursary to attend ICORS 2008, London, England (Aug. 2008)

PUBLICATIONS
- **Mariani, MM**; Lampen, P; Popp, J; Wood, BR; Deckert, V. (2009) Impact of fixation on in vitro cell culture lines monitored with Raman spectroscopy. *Analyst.* **134**, 1154 – 1161.
- **Mariani, MM**; Day, PJR; Deckert, V (2009) Applications of Modern Micro-Raman Spectroscopy For Cell Analyses. Integrative Biology, DOI:10.1039/B920572A
- **MM Mariani** & V Deckert. 'Principles, Benefits & Applications of Modern Raman Spectroscopy ', (2009) Bunsenmagazin (In Press)
- **Mariani, MM**; Chen, L; Day, PJR (2007) The Miniaturization of PCR for Quantitative Clinical Diagnostics. PCR Revolution (Ed. S. A. Bustin) Cambridge University Press (In Press)

- **Mariani, MM**; Lampen, P; Maccoux, L; Wood, BR; Deckert, V. (2009) FT-IR Mapping of Keratinocyte Organizational Profiles During *in vitro* Wound Healing. Anal. Chem. *(submitted)*
- **Mariani, MM**; Maccoux, LJ; Matthäus, C; Diem, M; Hengstler, J; Deckert, V. (2009). Nuclear Membrane Changes in Senescent Breast Cancer Carcinoma Cells. Anal Chem. *(submitted)*
- Vogler, N; Bocklitz, T; **Mariani, MM;** Deckert, V; Rösch, P; Akimov, D; Dietzek, B; Popp, J (2009) Physically motivated CARS image analysis. JOSAA *(submitted)*
- **Mariani, MM**; Richter, M; Lampen, P; Pulvermacher, E; Deckert, V. (2008) The Analysis of Cell-Cell Interactions in Wound Healing Using Vibrational Spectroscopic Techniques & Quantitative Gene Expression Analysis. *Proceedings of the XXIst ICORS* (Ed. R. Withnall and B. Z. Chowdhry) IMPublications Chichester, pp.1085.
- **Mariani, MM;** Deckert-Gaudig, T; Deckert, V (2009) A label-free *in vitro* approach to visualize lipid distribution of the cell membrane during stimulated re-epithelialization. Biophysical Journal *(in preparation)*
- **Mariani, MM;** Karimiani, E; Day, PJR (2009) Sample handling for defining disease threshold in circulating blood and haemotological malignancies. *(in preparation)*
- **Mariani, MM;** Wood, BR; Diem, M; Deckert, V (2009) High Resolution Imaging & Gene Expression Profiling of ECM Localization & Lipid Profiles in Epidermal Keratinocytes During *in vitro* Wound Healing**.** *(in preparation)*
- Maccoux, LJ; **Mariani, MM;** Schormann, W., Matthäus, C., Diem, M., Deckert, V., Hengstler, J.G. (2009) Detection of cytochrome-*c* levels in senescent epithelial breast carcinoma cells using confocal micro-Raman Spectroscopy. *(in preparation)*

PRESENTATIONS & FIRST-AUTHOR POSTERS
Oral Presentations

- Oral presentation entitled 'Applications of Vibrational Spectroscopy in Cell Interaction Analyses' at Mount Sinai School of Medicine, New York City, Oct. 2009
- Oral presentation entitled 'Cell Organization in Wound Healing using FT-IR & Quantitative Gene Expression Analysis' at the Technical University of Dortmund, Dortmund, Germany, Feb. 2009
- Oral presentation entitled 'Cell-Cell Interactions in Wound Healing' at Northeastern University, Boston, MA, November 2008
- Oral presentation entitled 'Cell-Cell Interactions in Wound Healing' at SPEC, October 2008

First-Author Posters

- Poster presentations, entitled 'Impact of *in-vitro* cell culture sample preparation techniques on Raman spectra'; 'Raman imaging & multivariate analysis of senescent breast carcinoma cells'; 'Keratinocyte Organization in Epidermal Wound Healing using FT-IR & Quantitative Gene Expression Analysis' at ANAKON, March 2009
- Poster presentation entitled 'Impact of *in-vitro* cell culture sample preparation techniques on Raman spectra' at SPEC, October 2008
- Poster presentation entitled 'Cell - Cell Interactions in Wound Healing Using Vibrational Spectroscopy & Quantitative Gene Expression Analysis' at the International Conference of Raman Spectroscopy (ICORS), August 2008
- Poster presentation entitled 'Characterization of epidermal and dermal cell lines using Raman, IR and quantitative gene expression analysis' at the Microscale Bioseparations (MSB) Symposium, March 2008
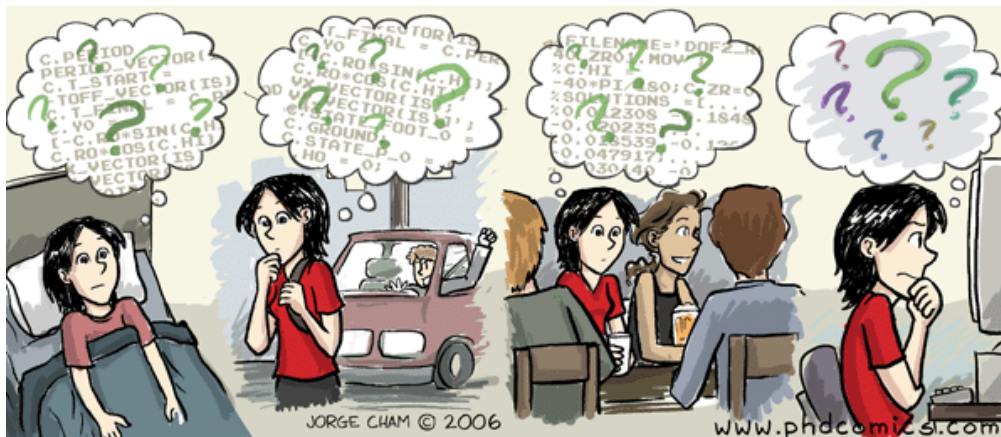
Research is what I'm doing when I don't know what I'm doing.
~Wernher Von Braun (German-American rocket physicist & astronautics engineer)

Research is a funny thing. I was once instructed that it was similar to running a marathon-filled with moments of excessive motivation often offset swiftly by feelings of exhaustion and defeat; thoughts of exhilaration for the end combined with persistent whispers of whether continuing was *really* necessary, all combined with persistent thoughts of the days work and the 'big picture'.

As the research haze lifts and I near the end of my Ph.D studies, I can begin to look back and see that this journey was in fact as important was critical for the outcome. From the numerous bumps and turns encountered during the hours in the lab, excessive data analysis and fruitful discussions about the sometimes important, but often not-so-pressing issues, the ability to refine and expand on my abilities as a scientist and as an individual have grown tremendously.

Experience and wisdom are not gained without the guidance and support of others and therefore, there are multiple people whom I must extend my sincerest gratitude. Foremost, I would like to thank my supervisor, Dr. Volker Deckert, for his continual encouragement, enthusiasm and support from my very beginning at ISAS. His passion and excitement for vibrational spectroscopy and research in general was infectious and helped make each day more stimulating then the previous. I would also like to thank the

members of my research group (past and present), my 'Manchester crew' and all of my friends at ISAS for their support, both at work and outside.

Ofcourse, I must also thank my patient, patient roommate Lindsey. Our numerous conversations and conversation-snippets surrounding research and life, at all hours of the day, have also been central to continuing on the research marathon.

Tremendous gratitude is also extended to my family and friends, both near and far. Their encouragement from the beginning of college straight through to this Ph.D has really provided me with the foundation to continually make the hard, exciting, often scary but always rewarding decisions to keep pushing myself and attain my dreams. I would lastly like to extend my appreciation to all my grandparents, for without their tremendous journeys, I would have never been able to encounter many of these opportunities.